Wolfson Centre for Magnetics
School of Engineering
Cardiff University

A Steady State Model for Prediction of Amplitude and Phase Errors in Measuring Current Transformers

Tomasz Kutrowski

A thesis submitted for the degree of

Doctor of Philosophy

Wales, May 2014

Acknowledgements

The work has been carried out at the Wolfson Centre for Magnetics, Cardiff School of Engineering, Cardiff University, to which I am grateful for providing me with an opportunity to pursue research at and the resources needed to complete this project.

I would like to express my gratitude to Prof. A. J. Moses for his invaluable guidance and discussion throughout this investigation.

I would like to extend my appreciation to my second supervisor Dr P. I. Anderson for support and encouragement.

Special thanks to Howard Butler Ltd., Walsall, England and T. Welch personally for provision of specimens used in this investigation.

I would like to thank EPSRC for funding my studentship for three years to work on this project.

Thanks to the kindness of engineering research office staff.

My sincere gratitude to the Electrical and Mechanical Workshop teams at School of Engineering for their work and assistance.

I am thankful to all the staff and students at the Wolfson Centre, Dr Y. Melikhov in particular, for their help, discussions and friendly atmosphere throughout my studies.

Finally, I would like to appreciate un–ending encouragement from my family.

Abstract

Foreseen expansion and increasing complexity of power distribution networks will increase demand for accurate metering of electric energy flow. The current transformer (CT) is widely used in measurement systems and has direct effect on the overall accuracy of electric power measurement. Therefore, its design and performance are of great importance.

A steady state model of a CT is proposed to relate its performance to basic magnetic properties of its core. It enables a CT amplitude and phase errors to be predicted from the magnetic permeability and power loss of its core. Therefore it can be easily implemented at the design stage of these devices. The accuracy of the model has been verified against experimental data and the predicted CT errors were found to be in a good agreement with measured values. A negligible leakage reactance design CT is considered in this work, but an additional parameter would have to be considered for gapped cores or non–uniformly distributed windings.

CT errors are determined by magnetic properties of its core in a wide flux density range. Measurement of magnetic properties at very low flux densities can be extremely challenging due to low signal-to-noise ratio. An accurate, low flux density measurement system has been developed for the investigation of CTs. It features digital triggering, cycles and moving averaging techniques, innovative digital compensation, customised digital feedback algorithm and is capable of measuring magnetic properties of materials at flux densities as low as few μT. This setup can be used for testing variety of ferromagnetic materials for other low flux density applications such as magnetic shielding.

Table of Content

List of table captions

List of figure captions

Acronyms

ADC	Analogue to Digital Converter
ATC	Analogue Trigger Circuitry
CGO	Conventional Grain Oriented
CT	Current Transformer
DAC	Digital to Analogue Converter
DAQ	Data Acquisition Card
DOE	Department of Energy
DSA	Digital Signal Analyser, Dynamic Signal Acquisition
EMI	Electromagnetic interference
FF	Form Factor
FFT	Fast Fourier Transform
FM	Ferromagnetic
GO	Grain Oriented
HGO	High permeability Grain Oriented
ICT	Instrument Current Transformer
IT	Instrument Transformer
IVT	Instrument Voltage Transformer
JA	Jiles–Atherton
LSB	Least Significant Bit
MCT	Measuring Current Transformer
NI	National Instruments
NO	Non Oriented Steel
PC	Personal Computer
PCI	Peripheral Component Interconnect Local Bus
PXI	PCI eXtensions for Instrumentation
RMS	Root Mean Square
SCXI	Signal Conditioning eXtensions for Instrumentation
SST	Single Strip Tester
subVI	Subprogram in LabVIEW
TCR	Temperature Coefficient of Resistance
TDMS	Technical Data Management and Streaming
THD	Total Harmonic Distortion
VI	Virtual Instrumentation Program Written in LabVIEW
VT	Voltage Transformer

Chapter 1

Introduction

1.1. Scope, motivation and contribution

There is a great deal of political pressure to reduce the carbon dioxide emissions by increasing the production of renewable electric energy [1.1] following the Kyoto Protocol, the international treaty, forcing industrialised countries to reduce emissions of greenhouse gases. All this in effort to decelerate the global warming. Whatever the reason for switching to renewable sources of energy, this will lead to a decentralised generation of electricity and combined with foreseen growth of demand for electricity will require a more complex structure of the electricity distribution grid [1.3]. For proper management of such a network, and reconciliation of the parties involved in generation, transmission and distribution of electricity, accurate measurement of energy flow is crucial [1.1], [1.4].

One of the devices widely used in electric power measurement systems is the current transformer (CT) [1.5]. It scales down the current and isolates measuring instruments from high voltages. Therefore its accuracy of current transformation has a direct influence on the accuracy of power measurement [1.7].

There are numerous complex models, by Guerra and Mota [1.8], Annakkage et al. [1.9], Rezaei–Zare et al. [1.10], and others, that require detailed magnetic information on a CT core and sophisticated modelling techniques. These models are commonly employed in transient state studies of protective current transformers. At the same time designers of current transformers lack a steady state model relating CT errors to commonly available data on magnetic properties of its core that could be easily utilized at the design stage of these devices.

The performance of current transformers is well specified in international standards [1.11] and [1.12] to assure accurate measurement of electric power flow. CT errors have to be below specific limits over a full working range of currents and thus the core magnetic properties over a corresponding range of flux densities are important [1.13]. Determination of current transformer core magnetic properties at very low flux densities is extremely challenging due to low signal-to-noise ratio of induced in magnetic flux sensing coil voltage [1.14]. Unacceptable variation in magnetic permeability within batches has also been reported [1.15] adding to the complexity of a current transformer design. Consequently an accurate, low flux density measurement system was critical for investigation of current transformers.

1.2. Organisation of the thesis

Work undertaken in this investigation can be divided into analytical and experimental parts. The former investigates a relationship between a current transformer errors and magnetic properties of its core. This resulted in the development of a current transformer model which subsequently is evaluated based on tested accuracy of a current transformer and measured magnetic characteristics of its core. The experimental part comprises the development and assessment of a low flux density measurement system, and a set up for testing current transformer errors.

Chapter 2 presents the overall background of this research work. Basics of transformers and, more specifically, details of current transformers are discussed. Attention is given to the characteristics of materials used for core production. Subsequently, other current sensing devices are described.

In chapter 3, the development and construction of the system for measurement of the magnetic properties of materials is described in details. It includes a brief explanation of the principles of this magnetic measurement and discussion on the selection of the system hardware, control algorithm including triggering and feedback and the realisation of this algorithm in Labview software.

Modelling of a Current Transformer by means of an equivalent circuit diagram is elaborated on in Chapter 4. The relationship between magnetic properties and the exciting impedance is derived and discussed. An algorithm of current transformer errors calculation is proposed and programmed. A case study is simulated and analysed.

Evaluation of the current transformer model is presented in chapter 5. This includes information on what data was required for this evaluation. The results of the comparison of CT errors derived by means of the model and those measured experimentally are presented and discussed. The assumptions made in developing the model are assessed critically. Finally, idealized materials are incorporated into the model to test their suitability for current transformer applications.

The overall conclusions and suggested directions for future work are presented in Chapter 6.

1.3. References

[1.1] Meeting the Energy Challenge, A White Paper on Energy, Department of Trade and Industry, 2007

[1.2] http://www.kyotoprotocol.com

[1.3] postnote, UK Electricity Infrastructure, Parliamentary Office of Science and Technology, Number 280, 2007

[1.4] B. L. Capehart (editor), Encyclopedia of Energy Engineering and Technology, Vol. 2–3, CRC Press, 2007

[1.5] N. Locci, C. Muscas, A Digital Compensation Method for Improving Current Transformer Accuracy, IEEE Transactions On Power Delivery, Vol. 15, No. 4, pp. 1104–1109, 2000

[1.6] S. Ziegler, R. C. Woodward, H. H. C. Iu, L. J. Borle, Current Sensing Techniques: A Review, IEEE Sensors Journal, Vol. 9, No. 4, pp. 354–376, 2009

[1.7] K. Draxler, R. Styblikova, Influence of Instrument Transformers on Quality of Electrical Power and Energy Measurement, IEEE International Symposium on Industrial Electronics, pp. 1317–1321, 2007

[1.8] F. C. F. Guerra, W. S. Mota, Current Transformer Model, IEEE Transactions on Power Delivery, Vol. 22, No. 1, pp. 187–194, 2007

[1.9] U. D. Annakkage, P. G. McLaren, E. Dirks, R. P. Jayasinghe, A. D. Parker, A Current Transformer Model Based on the Jiles–Atherton Theory of Ferromagnetic Hysteresis, IEEE Transactions on Power Delivery, Vol. 15, No. 1, pp. 57–61, 2000

[1.10] A. Rezaei–Zare, R. Iravani, M. Sanaye–Pasand, H. Mohseni, S. Farhangi, An Accurate Current Transformer Model Based on Preisach Theory For The Analysis of Electromagnetic Transients, IEEE Transactions on Power Delivery, Vol. 23, No. 1, pp. 233–242, 2008

[1.11] Instrument Transformers – Part1: Current transformers, International Standard, IEC 60044–1:1996

[1.12] Requirements for Instrument Transformers, IEEE Standard, C57.13–2008

[1.13] B. D. Jenkins, Introduction to Instrument Transformers, George Newnes, 1967

[1.14] A. J. Moses, Challenges in High and Low Field AC Magnetic Measurements for Material Modelling and Electrical Machine Performance Prediction, IET Seminar, pp. 15–20, 2006

[1.15] Z. Godec, High Permeability Grain Oriented Electrical Steels and Instrument Current Transformers, Journal of Magnetism and Magnetic Materials, Vol. 20, No. 3, pp. 243–244, 1980

Chapter 2

Background information

Transformers are electrical machines which transfer electrical energy from one electric circuit to another by means of magnetic circuit. There are many types of transformers depending on their application, including:

- distribution transformers
- power transformers
- instrument transformers
- communication transformers
- audio transformers

There are two types of instrument transformers (IT) depending on their function, voltage (IVT) and current instrument transformers (ICT). Both types are utilised in transmission and distribution networks but depending on their application and hence design requirements, they are commonly divided into two groups:

- protective – used with power–system protective equipment and relays and are required to operate under faulty line conditions, overload currents/voltages, but sacrifice the accuracy.
- measuring – feed indicating and summation–metering equipment, thus accuracy within typical line currents is of prime importance. In the case of an overload current/voltage however, the opposite is desirable in order to protect measuring apparatus.

In this work measuring current transformers are investigated.

2.1. Basics of current transformers

The current transformer (CT) is a low power transformer that operates under practically short circuited conditions enabling a large current to be measured safely and with significantly smaller range apparatus. It is composed of a ferromagnetic core on which insulated primary and secondary coils are wound. The primary winding is usually formed by a conductor going through the centre of the CT core (window) which constitutes one single turn, as shown in figure 2.1a.

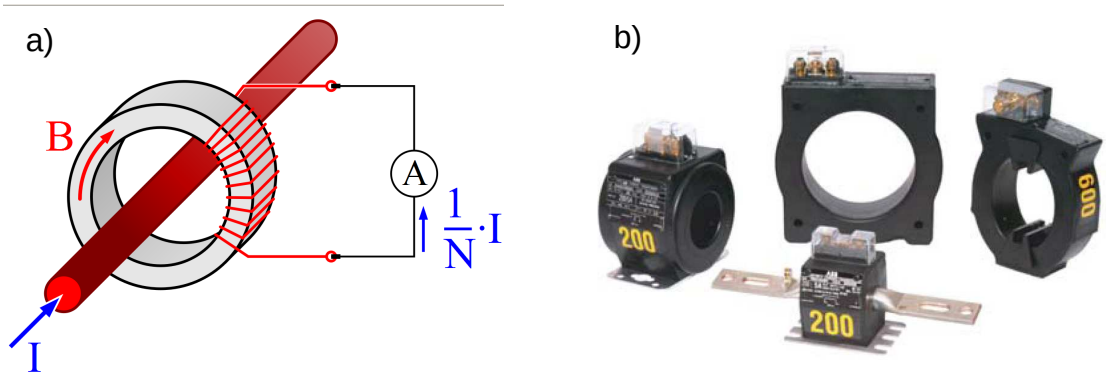

Figure 2.1 a) Sketch of a current transformer (CT). Courtesy of wikipedia.org
b) Examples of commercially available CTs (window and bar type) Courtesy of ABB Ltd

The operation of a CT is based on three principles. According to Ampere's Law, an alternating current carrying conductor produces a magnetic field around its circumference. As the CT core is few orders of magnitude more magnetically permeable than air, the field is concentrated inside it as depicted in figure 2.1a. This internal, alternating magnetic field generates an electromotive force (voltage) in the secondary coil wound on the core (Faraday's Law). The induced voltage gives rise to a current whose magnetic field, according to Lenz's Law, opposes the original magnetic flux. The value of the secondary current is proportional to the primary current and can be expressed as in equation (2.1):

$$I_S = I_P \frac{N_P}{N_S} \tag{2.1}$$

I_S – RMS value of secondary current

I_P – RMS value of primary current

N_P, N_S – number of turns in primary and secondary windings, respectively

CTs are defined by the ratio of the rated primary to secondary currents (e.g. 500:5). The most common secondary rating is 5 A while 1 A and 2 A are also used. Nevertheless, the widespread introduction of electronic watt-hour meters advocates lower ratings [2.1].

The most important characteristic of a measuring CT is its current transformation accuracy which is defined in terms of two errors [2.2]:

- The amplitude error is a difference of RMS values of both currents in per cent of the primary current:

$$F\% = \frac{I_S \cdot \frac{N_S}{N_P} - I_P}{I_P} \cdot 100\% \tag{2.2}$$

- The phase error is a difference in phase between secondary and primary current:

$$PD = \varphi_S - \varphi_P \tag{2.3}$$

The performance of a CT, characterised by the above errors, is mainly determined by the magnetic characteristics of its core material [2.3]. For this reason relevant magnetic phenomena are discussed in the following section.

CTs are designed to work under low impedance in order to maximise their accuracy. However, this working condition must be ensured whenever a CT is energised for safety reasons. In the event the CT output is open–circuited while energised, its core will saturate periodically possibly overheating the core. The high rate of change of magnetic flux will result in excessive, distorted secondary voltage (Figure 2.2), hazardous to personnel and possibly leading to an electric arc between secondary terminals, damage to the secondary winding insulation [2.6].

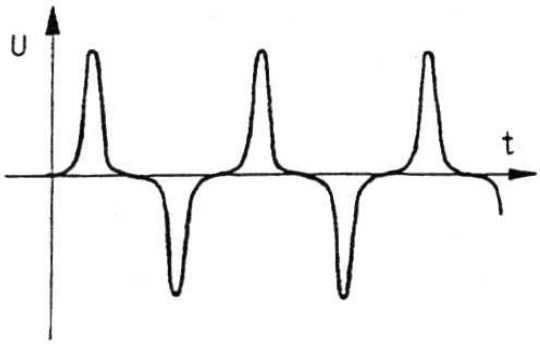

Figure 2.2 Voltage (U) induced in the secondary winding of a CT operated in a no–load condition.

2.2. Basics of magnetism

Magnetism is a phenomenon by which materials exert an attractive or repulsive force on other materials. The source of the force are constantly moving, electrically charged particles of an atom. In figure 2.3 a nucleus and an electron are shown spinning about their axes, and the orbit on which the electron is circling the nucleus. All three movements create their own magnetic fields which are called magnetic dipole moments. The two magnetic moments of an electron are three orders of magnitude stronger than that of a spinning proton (charged component of the nucleus). Hence the combined magnetic moment of an electron plays the main role in magnetism.

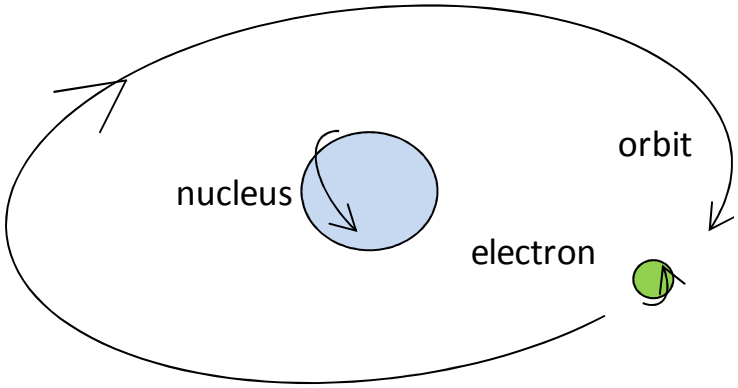

Figure 2.3 The orbit of a spinning electron about the nucleus of an atom.

On the microscopic scale, the elementary magnetic moments constitute the magnetic moment of an atom. Similarly, atom magnetic moments in a material structure combine into the macroscopic magnetic behaviour of a material.

2.2.1 Magnetic classification of materials

Materials can be divided into groups depending on their response to a magnetic field and their internal orientation of magnetic moments. The main groups are:

- diamagnets – random orientation in the absence of an external field (Figure 2.4a), align in the opposite direction to an external field (Figure 2.4b);
- paramagnets – random orientation in the absence of an external field (Figure 2.4a), align in the direction of an applied field (Figure 2.4b), but do not retain any magnetisation;
- ferromagnets – aligned over a limited volume (Figure 2.4b) respond to feeble magnetic fields and have the ability to retain magnetisation;
- anti–ferromagnets – adjacent magnetic moments tend to align anti–parallel to each other without an applied field (Figure 2.4c);
- ferrimagnets – exhibit uneven anti–ferromagnetism (Figure 2.4d).

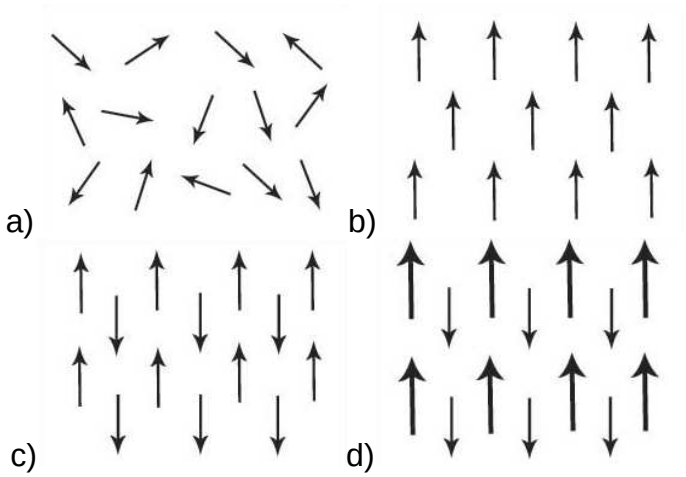

Figure 2.4 Schematic diagram showing orientation of magnetic moments:
a) random (diamagnets, paramagnets without external field),
b) parallel alignment,
c) anti–parallel (one of many possible antiferromagnetic arrangements),
d) unequal anti–parallel (ferrimagnets).

2.2.2 Magnetic structure of ferromagnets

Ferromagnets are made up of magnetic moments aligned parallel in regions referred to as magnetic domains shown in figure 2.5. The spontaneous domain magnetisation is caused by exchange interaction between unpaired electron spins referred to as the exchange energy. The partition of bulk material into domains is a result of minimisation of other energies, not limited to:

- Magnetocrystalline (anisotropy) energy is associated with the crystallographic structure.
- Magnetoelastic (magnetostrictive) energy is connected to the strain in the crystallographic structure.
- Magnetostatic (demagnetising) arises from the material having finite dimensions.

In bulk ferromagnetic material, what seems to be a random magnetic orientation of domains as in figure 2.5 is actually a combination of magnetic moments that results in the lowest total energy.

Figure 2.5 Example of randomly oriented magnetic domains in bulk ferromagnetic material

An example of the minimisation of magnetostatic and exchange energy is shown in figure 2.6. The exchange interaction between magnetic moments aligns them parallel to minimise the corresponding energy. This however, creates a single domain throughout a material that acts like a permanent magnet and creates a strong external field as shown in figure 2.6a (high magnetostatic energy). The north and south pole of the single domain magnet create internal demagnetising field opposite to of the material magnetisation. The material not able to withstand this strong demagnetising field divides into domains (figure 2.6 b, c) until rise in exchange energy due to misaligned

magnetic moments exceeds the accompanying reduction in the magnetostatic energy.

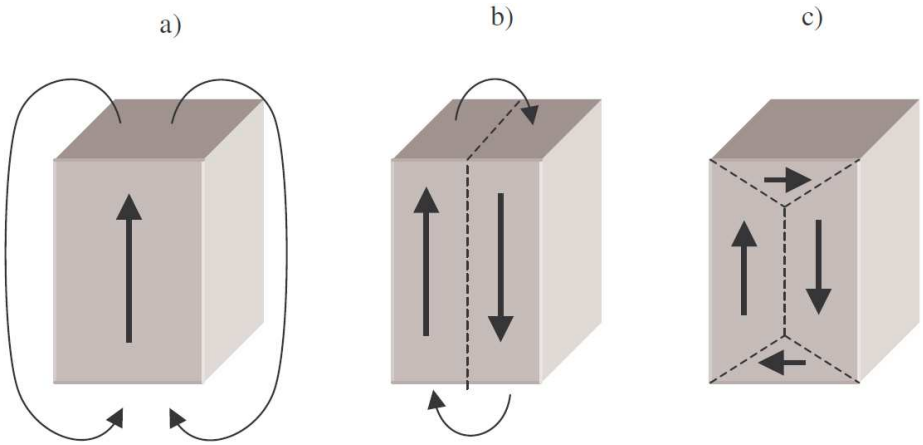

Figure 2.6 Diagrams illustrating the formation of domains due to minimisation of magnetostatic and exchange energy in ferromagnets:
a) single–domain state of high magnetostatic and low exchange energy,
b) two–domain state with reduced magnetostatic energy and increased exchange energy,
c) further minimisation of total energy through formation of closure domains [2.7]

The exchange force between the adjacent magnetic moments prevents sudden change in direction. As a result, areas between domains exist, called domain walls, where magnetic moments gradually change their individual directions. In figure 2.7 two possible structures of the magnetic moment rotation in a domain wall are shown, Neél and Bloch type of wall. Generally, material with the latter type is used for manufacturing CTs. However, in recent years there has been an increased interest in production of CT cores from very thin tapes (amorphous and nanocrystalline), in which the Neél type of wall prevails. The difference between the two types of walls is the plane of rotation which usually is perpendicular to the domain. In the Neél wall the magnetic moments rotate in the plane of the domain.

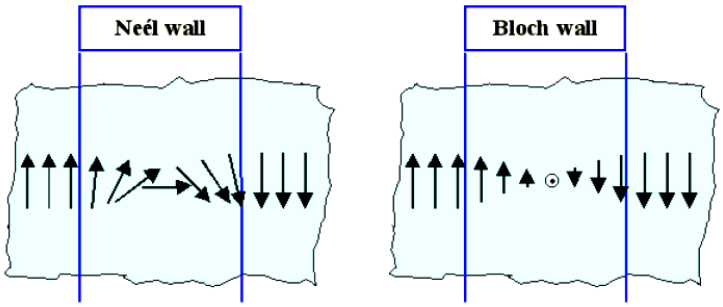

Figure 2.7 Illustration of the magnetic moments arrangement in the Neél and Bloch type domain wall

2.2.3 Ferromagnetic behaviour in magnetic field

When an external field is applied to a ferromagnetic material the domains oriented in a favourable direction (closest to the direction of field) increase their volume at the expense of others. The overall magnetisation of a material in an arbitrary direction, that is the sum of elementary magnetic moments components in that direction, can be quantified per unit of volume:

$$\vec{M} = \frac{\vec{m}}{V} \quad \left[\frac{A}{m}\right] \tag{2.4}$$

$\vec{m}$ – net magnetic moment vector

V – volume of the material

Through magnetic measurement, magnetic flux density (magnetic induction) is commonly determined. It quantifies the magnetic response of a material in the direction of the applied magnetic field. The relationship between magnetisation and magnetic induction is described by the following formula:

$$\vec{B} = \mu_0(\vec{H} + \vec{M}) \quad [T] \tag{2.5}$$

μ_0 – magnetic permeability of free space, $4\pi 10^{-7}$ [H/m]

$\vec{H}$ – vector of the magnetic field

The vector quantities of flux density and magnetic field given above are hereafter regarded as parallel and expressed as scalar quantities.

The relationship between the magnetising field (H) and the magnetic flux density (B), which it produces, is used to characterise ferromagnetic materials.

For that purpose, a sample of material is magnetised such that the characteristics shown in Figure 2.8 can be plotted, referred to as BH loops.

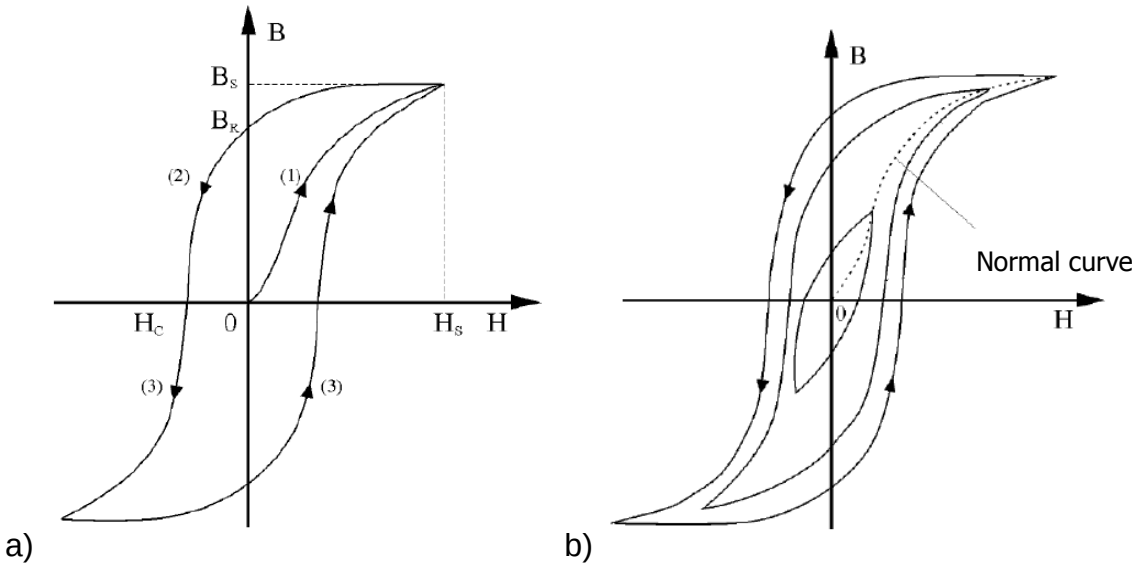

Figure 2.8 Examples of BH loops commonly used to describe magnetic characteristics of materials:
a) DC or quasi–static (near DC) BH loop (also called hysteresis) with initial magnetisation curve
b) BH loops at different inductions with normal curve

Depending on the exact conditions of the BH loop measurement various corresponding parameters can be derived from BH characteristics, as described below [2.8]:

- Remanence is the magnetic induction retained in a ferromagnetic material after the removal of an applied magnetic field.
- Retentivity (B_R in Figure 2.8a) is equal to the remanence after saturating magnetic field is removed.
- Residual induction is the value of induction at a zero field during symmetrical cyclic magnetisation.
- Coercive force is the value of the magnetic field at zero induction during symmetrical cyclic magnetisation.
- Saturation induction (B_S in Figure 2.8a) is the value of induction when all the magnetic moments in a material are parallel to the direction of applied field.
- Coercivity (H_C in Figure 2.8a) is the magnetic field required to reduce the magnetic induction from saturation to zero.

- Saturation magnetic field (H_S in Figure 2.8a) is the value of the magnetic field necessary to saturate a material.
- Power loss can be calculated by dividing the area of the loop (the amount of work done over one cycle of magnetisation) by the time duration of that cycle.
- Absolute permeability quantifies how strongly a material is responding to a magnetic field. It is equal to the gradient of a line drawn from the origin to a point on the normal magnetisation (also called commutation) curve (dotted line in Figure 2.8b). Due to the fact that the permeability is dependent on the magnetic history and applied field, various types have been defined (initial, complex, incremental, differential).
- Relative permeability of material is a measure of how many times the absolute permeability is stronger than that of free space.
- Maximum permeability is the maximum value of permeability a material exhibits and corresponds to the "knee" area of the magnetisation curve (Figure 2.9).
- Differential permeability is the slope of the magnetisation curve at any point.
- Incremental permeability is the permeability measured under superimposed direct and alternating magnetisations.

The properties of materials, and thus BH loops, vary with frequency. Since the devices investigated in this work operate at a frequency of 50 Hz, the magnetic properties considered hereafter relate only to this frequency, unless specified otherwise.

2.3. Core material selection

Since CT performance is determined mainly by the magnetic properties of its core, it is very important to select a suitable core material during production. The desirable properties are low power loss and high magnetic permeability,

both over the CT's operating flux density range. CTs are designed to operate in the region between the ankle and the knee [2.3] (the areas marked 1 and 2 on the red curve in Figure 2.9) of the core's normal magnetisation curve (1 mT – 0.4 T magnetic flux density for cores made of electrical steel). The magnetisation below the ankle region is proportionate to the magnetic field hence a constant value of permeability at very low inductions [2.4]. In grain oriented electrical steel this has been found to occur below few hundredths of microtesla [2.5]. The magnetisation below the ankle region is also thought to be reversible, as at such low fields there is not enough energy to unpin the domain walls; hence the movement is limited to wall bowing. In the ankle region, the magnetisation becomes irreversible as an increasing proportion of domain walls jump between pinning sites. The permeability increases continuously until its maximum value which occurs in within the knee region. At this stage most of the domains are aligned along the grains easy directions towards the applied field and the magnetic dipoles are being forced away from their easy directions. From there to saturation, rotation predominates.

The above division of the magnetization curve into regions is arbitrary and at various stages wall motion mayo be occurring in one portion of a specimen and rotation in another.

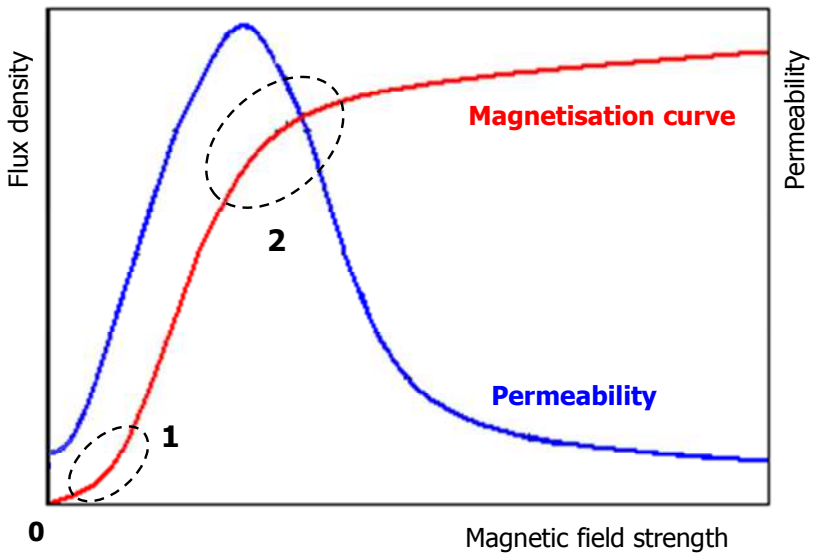

Figure 2.9 An example of magnetisation curve and permeability characteristic of electrical steels, 1 – ankle region, 2 – knee region [2.9]

Another factor to consider in the CT design is the temperature dependence of the core power loss and permeability. A CT often operates outdoors and thus is exposed to considerable temperature fluctuations. The CT core may also heat up from the magnetic losses and high currents flowing in windings. Although the variation of power loss and permeability in temperatures ranging from -20 to 50 °C, in a wide range of flux densities, has not been investigated as yet, the accuracy of CTs is potentially compromised by significant changes in operation temperature. An example of temperature dependence of a magnetic property, in this case the initial permeability, is shown in figure 2.10. The highly permeable 80% NiFe alloy exhibits variation up to 25% between temperatures of -5 and 50 °C and up to 30% between -30 and 0 °C.

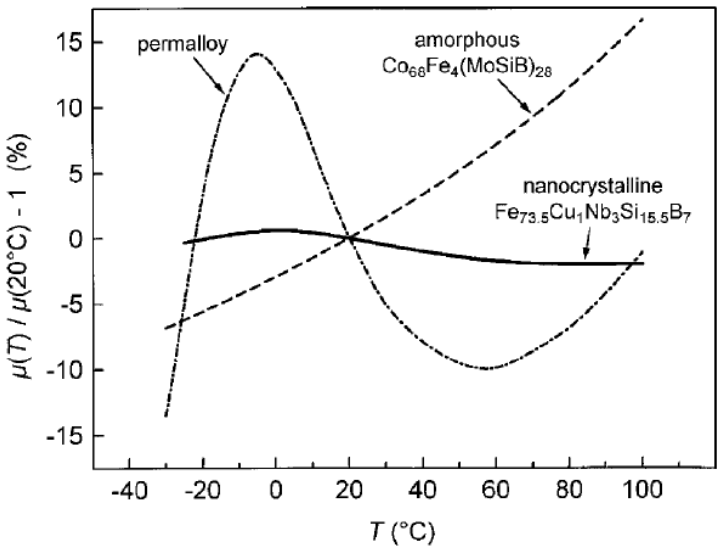

Figure 2.10 Percentage change of the initial permeability normalized to its room temperature value at various temperatures for highly permeable soft magnetic materials [2.10]

Similarly, causing stress in a core material may have detrimental effect on the magnetic properties considered. Stress might be unintentionally introduced during resin–impregnation or encapsulation. This is performed to insulate cores and add rigidity for handling purposes.

Several types of soft magnetic materials are used for manufacturing CT cores including CoFe, NiFe, amorphous, nanocrystlline alloys and SiFe steel [2.15]. A few of these materials and their basic magnetic properties are shown in Table 2.1. CoFe alloys, although have high saturation magnetisation, exhibit lower

permeability than other materials. The expensive NiFe alloys with the highest Ni content are characterised by the highest permeability of all magnetic materials. Their disadvantages are the low saturation magnetisation and cost. Modern, amorphous and nanocrystalline, alloys can be tailored to deliver as high permeabilities as those of NiFe alloys but without the advantage of higher saturation magnetisation. They can perform better in terms of permeability and power loss than electrical steels at acceptable flux densities but for a higher price. Additionally, the nanocrystalline alloys are very brittle and put restrictions on manufacturing. The more expensive alloys are used in small size, low rating CTs (homes, apartments), where the material cost is insignificant compared to the overall product price. A core made up of two alloys is also possible, as a means to improve the CT accuracy while limiting the cost of the core [2.16][2.17].

Table 2.1 Relevant magnetic properties of typical magnetic materials used in instrument transformers (ITs)

Material	Initial permeability μ_4 (*)	Maximum relative permeability	Power loss [W/kg] (**)	Saturation magnetisation [T]
CoFe alloy (17–50% Co) (VACOFLUX 17, VACOFLUX 48)	600 – 1 200	4 – 20 (10^3)	$P_{0,5}$ = 0.25 – 0.55	2.22 – 2.35
NiFe alloy (80 % Ni, VACOPERM 100)	100 (10^3)	250 (10^3)	$P_{0,5}$ = 0.015	0.74
NiFe alloy (54–68 % Ni, PERMAX M)	50 (10^3)	110 (10^3)	$P_{1,0}$ = 0.1	1.5
NiFe alloy (45–50 % Ni, PERMENORM 5000 H2)	12 (10^3)	90 (10^3)	$P_{1,0}$ = 0.25	1.55
NiFe alloy (35–40 % Ni, e.g. PERMENORM 3601 K5, MEGAPERM 40 L)	4 – 9 (10^3)	50 – 75 (10^3)	$P_{1,0}$ = 0.2 – 0.3	1.3 – 1.48
SiFe (3% Si, isotropic, TRAFOPERM N3)	700	13 (10^3)	$P_{1,0}$ = 1.0	2.03
Amorphous, e.g. $Co_{68}Fe_4(MoSiB)_{28}$	1 400 – 3 000	–	$P_{1,2}$ = 0.11 –0.12	0.55 – 1.55
Nanocrystalline, e.g. $Fe_{73.5}Cu_1Nb_3Si_{13.5}B_9$	100 – 100 000	10 – 400 (10^3)	–	1.2
CGO electrical steel	5 (10^3) (***)	40 – 45 (10^3)	$P_{1,0}$ = 0.3	2.03
HGO electrical steel	600 (***)	45 – 55 (10^3)	$P_{1,0}$ = 0.3	2.03

Notes: 50 Hz data; (*) μ_4 = relative permeability at 0.4 A/m; (**) $p_{0,5}$ = specific core losses at 0.5 T etc.; (***) results of measurements; [2.11][2.12][2.13][2.14]

Grain oriented silicon steel is still the most common CT core material [2.18][2.19]. However, it is graded according to its performance at 50/60 Hz at high flux density (1.5 and 1.7 T), and no information on magnetic characteristics variability over a wide range of flux density is normally provided by steel manufacturers [2.21]. Consequently, the selection based on available data might not necessarily result in the best CT performance. Furthermore, magnetic characteristics at low induction may deviate from core to core resulting in inconsistent performance [2.3].

2.4. Principles of a magnetic measurement

Magnetic properties of a material are generally measured by exposing a sample to a desired magnetic field while monitoring the response. Magnetic field in the system developed in this work is applied through a magnetising coil encompassing a sample. An example of an air magnetic field generated by a solenoid is shown in Figure 2.11. Magnetic field lines depicted by the bright, dense lines inside the helix coil illustrate the area of the uniform field. The magnetic flux density drops where lines become darker and sparse.

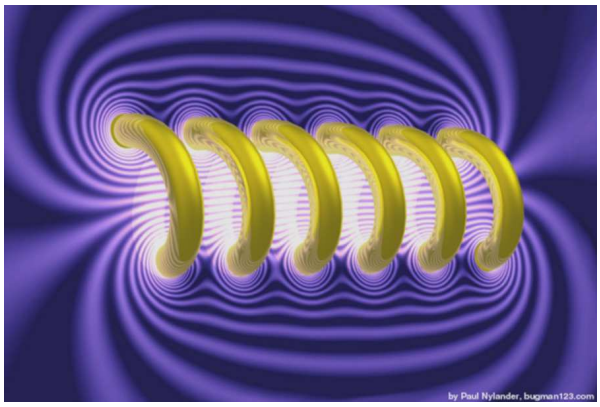

Figure 2.11 A magnetic field produced by a solenoid. Courtesy of P. Nylander [2.19]: yellow – current carrying conductor; bright lines on dark background – magnetic field lines

The value of magnetic field created by a current carrying conductor is described by the Ampère's circuital law [2.22]:

$$\oint_C H \cdot dl = I \tag{2.6}$$

$\oint_C$ – line integral around closed curve C

I – current enclosed by the curve C

The measurement of the material response to a magnetic field is realised by means of a search coil wrapped around a sample, as shown in Figure 2.12, and is based on Faraday's law of induction. The voltage induced in a coil is proportional to the number of turns and the magnetic flux rate of change [2.23]:

$$V(t) = -N \frac{d\Phi(t)}{dt} \tag{2.7}$$

V(t) – voltage induced in a coil

N – number of coil turns

$d\Phi(t)/dt$ – rate of change of magnetic flux density

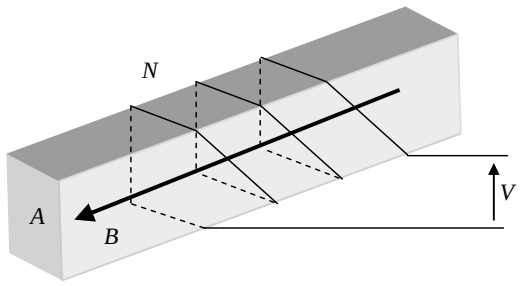

Figure 2.12 Voltage V induced in a search coil of N turns by magnetic flux density B in a sample of cross-sectional area A [2.24]

BH Curves can be obtained from measurements of current flowing through a magnetising coil and voltage induced in a search coil. An example of a BH loop with its characteristic points is shown in Figure 2.13. For the developed CT model two parameters were utilised, namely the area enclosed by the loop (power loss) and the ratio of maximum values of flux density and magnetic field (permeability).

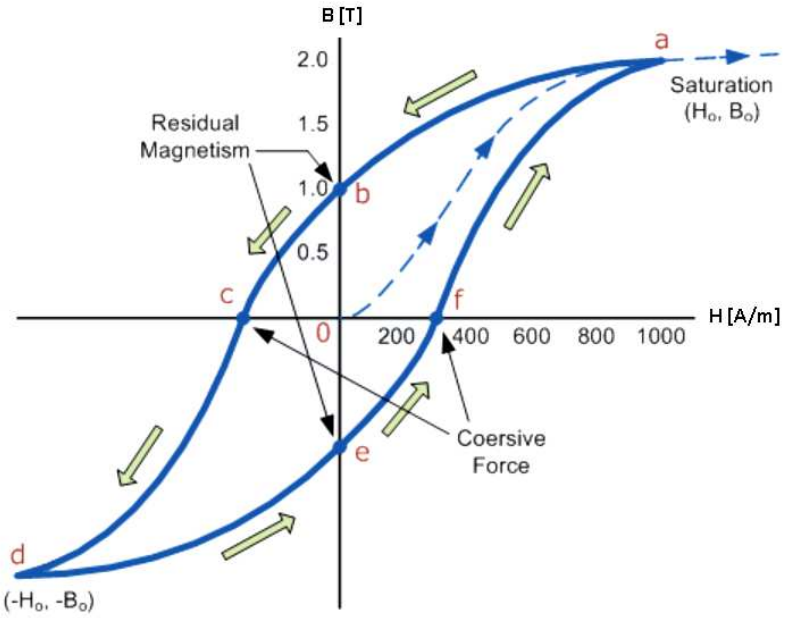

Figure 2.13 An example of a BH loop with its characteristic points. Adapted from www.electronics–tutorials.ws

There are several types of standardised samples that are used in magnetic measurements including toroid, ring, sheet, strip. Toroidal sample is commonly used when toroid is part of the final product, as it is generally the case with ITs. Otherwise strips of 30mm x 300mm dimensions are commonly used.

2.5. Equivalent circuit of a CT

The equivalent circuits of transformers are well established. These were described in 1948 by Cherry in [2.25], when he showed that the principle of duality exists between magnetic circuit of a transformer and the corresponding equivalent electric circuit. Furthermore, he gave a complete guide to creating circuits that can substitute the behaviour of transformers with reasonable accuracy for the purpose of analysis of circuits consisting of transformers [2.25].

Figure 2.14 shows a basic equivalent electric circuit diagram of a single phase transformer comprising electrical components that represent its physical behaviour at a steady state in the low frequency regime. A short description of the elements is given below [2.26]:

$\mathbf{R_P, R_S}$ – DC resistance of primary and secondary windings respectively

$\mathbf{X_P, X_S}$ – inductive reactances representing leakage flux of the corresponding windings

$\mathbf{R_C}$ – electric representation of the core magnetic loss

$\mathbf{X_C}$ – inductive reactance represents the physical need for a flux to be maintained in a core in order to induce voltage in a secondary winding

$\mathbf{Z_L}$ – impedance of load connected to the transformer

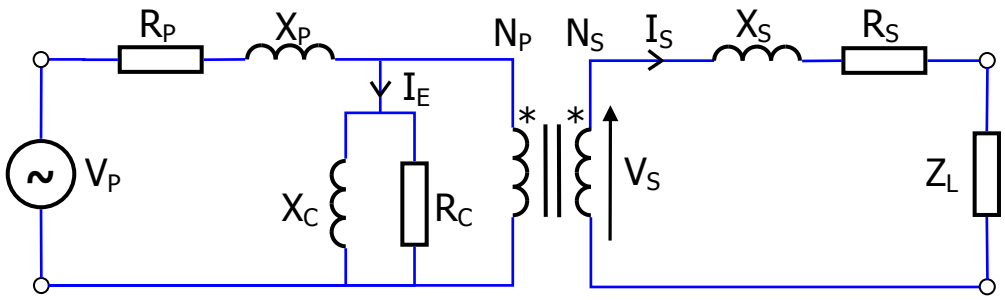

Figure 2.14 The equivalent electric circuit diagram of a single phase transformer in the low frequency regime [2.26]

The equivalent circuit diagram can be adopted to describe a particular type of transformer under desired conditions and hence it forms the basis of any CT model. Consequently, the same approach was used in developed CT model.

For the ease of analysis, the link between voltages and currents in the equivalent circuit is generally illustrated on a phasor diagram. The equivalent circuit of a CT with corresponding vector diagram is shown and discussed in section 4.1.

2.6. Review of CT models

Several CT models have been identified and evaluated, the majority for transient studies applicable to protective CTs. Two of these models are based on the well known Jiles–Atherton [2.27] and Preisach [2.28] hysteresis models. The first was utilised in CT modelling by Annakkage et al. and described in [2.29]. The authors modified the Jiles–Atherton model of hysteresis to simulate BH

loops of a CT core during transient operation. Subsequently, they calculated CT output signals by means of electromagnetic transient simulation programs (EMTDC, EMTP) and compared with measured CT characteristics. The CT model was specifically developed for analysis of the CT performance during short interruptions of power. It requires special software for the prediction of CT transient signals.

The second CT model, based on the Preisach hysteresis model, was also intended for analysis of CTs in transient conditions, more specifically, during fault currents and after the event [2.30]. In their publication, authors compared the accuracy of their model against Program Reactor Type–96 based CT model and the IEEE Power System Relaying Committee CT model. For the implementation of the CT model PSCAD/EMTDC software was used.

Both CT models described are based on the modelling of hysteresis which requires measurement of various parameters. In the case of the Preisach model, the accuracy of hysteresis prediction can be good, however a substantial amount of data must be taken and calculations are based on double integration which is time consuming. In the case of the classical Jiles–Atherton model, only two curves (initial magnetisation curve and major hysteresis loop) must be measured to identify the parameters of the model, however the hysteresis prediction will be limited within some flux density range, hence might not be applicable to assessment of measuring CTs. Furthermore, the Jiles–Atherton model still requires one integral calculation.

In the case of both models, the hysteresis prediction is time consuming and together with simulating CT output signals in special software, is a complex process. None of the models include any information on their usability for accuracy evaluation in the steady state conditions. As it is the case with other models, e.g. by Kojovic [2.31], Lorito [2.32], Guerra and Mota [2.33], the above models appear to be unsuitable for the steady state conditions error prediction of CTs.

Draxler and Styblikova proposed a model for calculating CT errors in the steady state conditions in order to analyse the effect of instrument transformer

(IT) errors on power measurement [2.34]. Therein the authors analyse errors of the VT and CT as two factors that can adversely affect the accuracy of a Wattmeter. The suggested CT model is based on the equivalent circuit diagram of a transformer, similar to the one shown in Figure 2.14, and the corresponding phasor diagram. The influence of the leakage inductance in the secondary winding is neglected. Based on the argument that the exciting current is much smaller than the primary, the authors simplified the phasor diagram such as the CT primary and secondary currents are parallel. Subsequently the final CT errors are given as:

$$\varepsilon_I = \frac{Bl\sin(\delta+\beta)}{\mu_0\mu_Z N_I I_I}\cdot 100\% \tag{2.8}$$

$$\delta_I = \frac{Bl\cos(\delta+\beta)}{\mu_0\mu_Z N_I I_I} \tag{2.9}$$

ε_I – CT amplitude error

B – flux density in the CT core

l – the length of the mean magnetic path of the toroidal core

δ – loss angle of the core

β – angle between the voltage induced in secondary and its current

μ_0, μ_Z – magnetic permeability of free space and apparent permeability respectively

N_I – number of primary windings

I_I – primary current

δ_I – phase angle of an uncorrected ICT

The above model relates CT errors to the core dimensions (magnetic path length), number of primary turns, and the steady state condition parameters (primary current, core permeability, flux density in the core, loss angle). It is not stated how the loss angle is being derived from the measurements, neither is the potential effect of the assumed parallelism of CT currents. Furthermore, the calculation of errors using equations (2.8)(2.9) requires the CT primary current value (I_1) at the corresponding magnetic induction (B) of the core. Since this is not available, the calculation of errors according to given formulae is not feasible.

Since the proposed model is not utilised in the CT errors prediction and only experimental data is presented, it is presumed that the authors' intention was

merely to show analytically the direct dependence of both CT errors on the primary current. This hypothesis is confirmed by the measurements presented in their publication. However the model does not allow the CT errors to be calculated and hence does not provide a solution for designing CTs.

2.7. CTs in energy distribution

Changes in the organization of electricity distribution are expected in the near future. There is a lot of political pressure to reduce the carbon dioxide emissions by increasing the production of renewable electric energy. That will lead to the decentralized generation of electricity and therefore will require a more complex structure of the grid [2.35].

For proper management of electric grid and reconciliation of the parties involved in generation, transmission and distribution of electricity, accurate measurement of energy flow is crucial [2.36].

Electric power is measured as a product of instantaneous voltage and current averaged over a required number of cycles. The CT is most often employed to scale down the current and isolate the measuring device from high voltage [2.37][2.38]. Therefore its accuracy of transformation has direct influence on power measurement correctness [2.34].

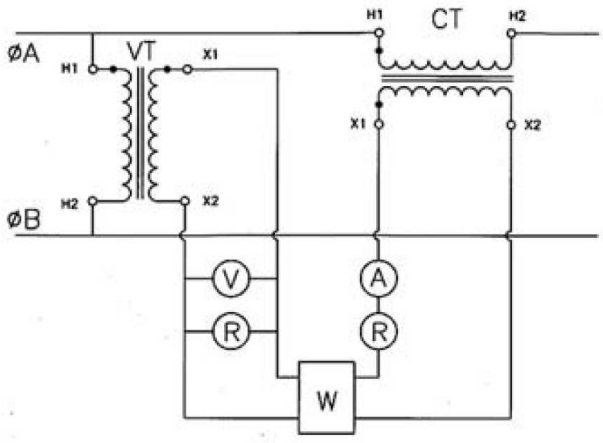

Figure 2.15 Typical wiring of the current and potential instrument transformers with Watt–hour meter [2.19]

To assess the effect of CT errors on the measured value of power, the following equation should be considered:

$$P = \frac{1}{T}\int_0^T i(t)\cdot v(t)\,dt = IV\cos\varphi \qquad (2.10)$$

P – active power

T – time duration of one cycle

i(t), I – instantaneous and RMS value of the current respectively

v(t), V – instantaneous and RMS value of the voltage respectively

φ – angle between the current and the voltage

cosφ – power factor

The error in current amplitude transformation of a CT defined by equation (4.21) contributes in the same amount of error to power measurement. The effect of phase error on the other hand is not so straightforward and it depends on the power factor of the network load:

$$P_{\%errorPD} = tg\varphi \cdot PD \cdot 100\% \qquad (2.11)$$

$P_{\%errorPD}$ – percentage error of the power measurement due to phase displacement of a CT

PD – phase displacement error of a CT

2.8. Alternative technologies of current sensing

CTs are prevalent in power–metering applications. Being passive devices, they do not require any external power supply. Their relatively simple construction and manufacturing provided cost effective solution to measurement of current. The CT, through its limited operating range, ensures the safety of the instrumentation during faulty currents. It also guarantees a high galvanic insulation between the input and output terminals.

There is growing concern over the accuracy of CTs in the presence of harmonics in the measured currents. The increasing accuracy demands and wider operating range are the additional factors against CTs.

As the technology advances and the expectations of measuring equipment performance rise, new designs of current sensors are becoming an attractive alternative to CTs. Ziegler et al. [2.38] compared numerous ways of measuring current based on various phenomena. Details of the most relevant of these techniques for current metering are summarised in the next sections.

2.8.1 Fiber–optic current sensors

Fiber–optic current transducers are based on magneto–optic effect discovered by Faraday in 1845 in which magnetic flux flowing in the same direction as light, through a suitable medium, affects its polarisation rotation (Figure 2.16).

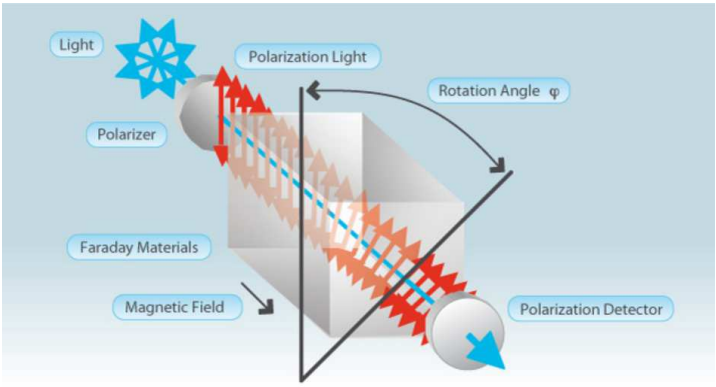

Figure 2.16 Illustration of current measurement by means of Faraday effect based sensor. Courtesy of Alstom

Due to the high complexity and cost involved, the Fiber–optic sensors are generally utilised for measuring of several hundredths thousand amperes. They provide significant reduction in bulk and cost of the electrical insulation compared with CTs.

2.8.2 Hall Effect current sensors

Various transducers utilise the Hall Effect in which the voltage appears across the edges of a thin sheet conductor carrying a current, whilst being exposed to a magnetic flux (Figure 2.17) [2.38].

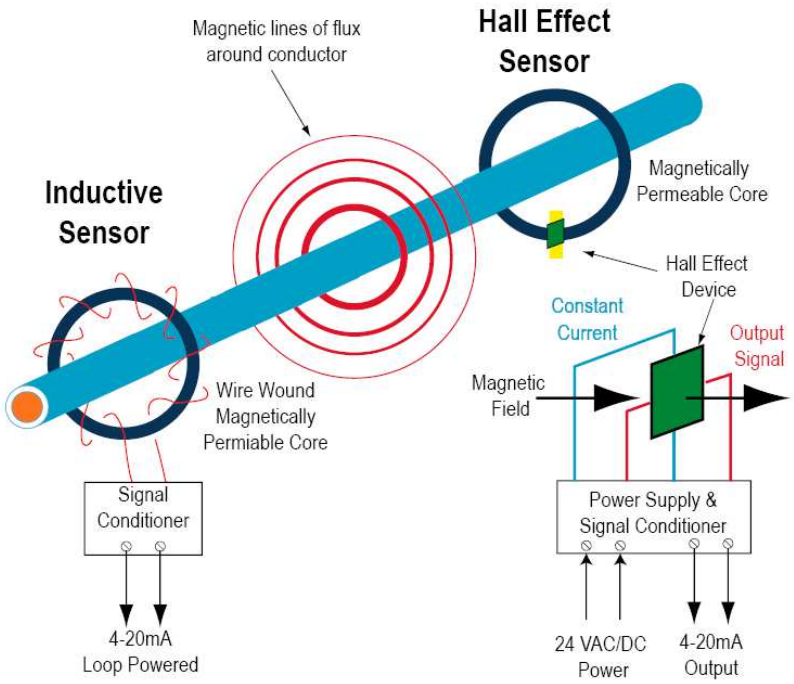

Figure 2.17 Illustration of current measurement by means of inductive sensor and Hall Effect sensor. Adapted from NK Technologies

Since the sensor requires both, a magnetic core and a Hall sensor, they are costly compare to that of CTs. The application is very much limited to current measurement of tens of thousands of amperes in magnitude, where the combination of magnetic saturation and size of CTs prohibits their use.

2.8.3 Air–core current sensors

The Rogowski–Chattock coil is a device similar to current transformer but with a non–magnetic core (Figure 2.18) where the induced secondary voltage is the output parameter, rather than the current [2.39].

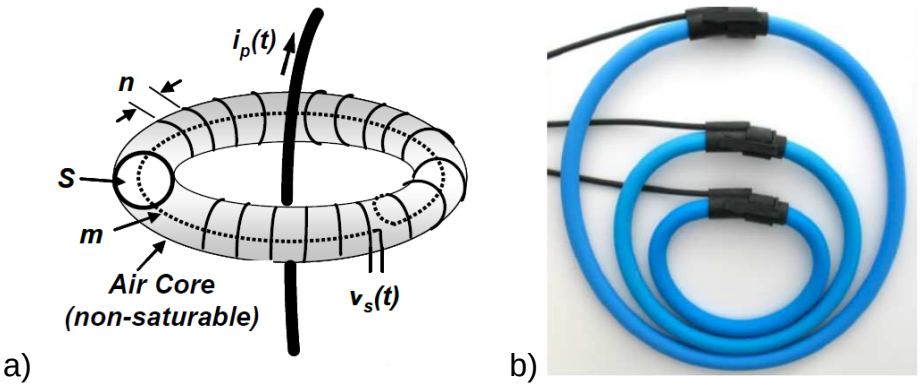

Figure 2.18 a) Sketch of a Rogowski–Chattock coil [2.40]
b) Example of a commercially available product. Courtesy of Submeter Solutions

The Rogowski–Chattock coil requires the output voltage to be integrated and thus its use with the electromechanical Watthour meters was not feasible due to the extra instrumentation requirement. Due to the lack of a magnetic concentrator, i.e. ferromagnetic core, the air coil is sensitive to external magnetic fields. The advantage of the non–magnetic core is the linear response, lack of saturation, and frequency independent operation. However to provide accurate measurements, the Rogowski coil sensor requires sophisticated, high precision manufacturing.

2.9. References

[2.1] Introduction to Current Transformers, Application Note, Elkor Technologies Inc., 2006

[2.2] Instrument Transformers – Part1: Current Transformers, International Standard, IEC 60044–1:1996

[2.3] B. D. Jenkins, Introduction to Instrument Transformers, George Newnes, 1967

[2.4] L. Rayleigh, On the behaviour of iron and steel under the operation of feeble magnetic forces, Philosophical Magazine, Vol. 23, pp. 225-245, 1887

[2.5] S. Zurek, F. Al–Naemi, A. J. Moses, Anomalous B–H Behaviour of Grain–oriented Electrical Steels at Very Low Flux Density, Journal of Magnetism and Magnetic Materials, Vol. 320, pp. 2521–2525, 2008

[2.6] A. Chwaleba, M. Poniński, Metrologia Elektryczna, WNT, Warszawa 1998

[2.7] S. Zurek, Two–dimensional magnetisation problems in electrical steels, PhD Thesis, Cardiff University, 2005

[2.8] Magnetic Circuits and Transformers, The MIT Press, 1965

[2.9] B. D. Cullity, Introduction to Magnetic Materials, John Wiley & Sons, 2009

[2.10] G. Herzer, Amorphous and Nanocrystalline Soft Magnets, Kluwer, 1997

[2.11] Soft Magnetic Cobalt–Iron–Alloys, PHT–0041, Vacuumschmelze GmbH & Co. KG., 2001

[2.12] Soft Magnetic Materials and Semi–finished Products, PHT–001, Vacuumschmelze GmbH & Co. KG., 2002

[2.13] G. Herzer, Nanocrystalline Soft Magnetic Alloys, Handbook of Magnetic Materials, Vol. 10, Elsevier, 1997

[2.14] M. A. Laughton, D. F. Warne, Electrical Engineer's Reference Book, Newnes, 2003

[2.15] T. Batista, B. A. Luciano, R. C. S. Freire, S. Y. C. Catunda, Current Transformer with Nanocrystalline Alloy Core for Measurement, Instrumentation and Measurement Technology Conference (I2MTC), pp. 1–4, 2011

[2.16] T. Edel, A-C current transformer functional with D-C current component present, United States Patent, 2005

[2.17] J. H. Harlow, Electric Power Transformer Engineering, CRC Press, 2003

[2.18] B. A. Luciano, J. M. C. Albuquerque, W. B. Castro, C. R. M. Afonso, Nanocrystalline Material in Toroidal Cores for Current Transformer: Analytical Study and Computational Simulations, Materials Research, Vol. 8, No. 4, pp. 395–400, 2005

[2.19] http://members.wolfram.com/jeffb/visualization/solenoid.shtml

[2.20] J. H. Harlow (editor), Electric Power Transformer Engineering, CRC Press LLC, 2004

[2.21] R. Pytlech, R. Rygał, W. Pluta, M. Soiński, Quick Measurement Procedure for Quality Flux Density Checking at 0.3 A/M in Toroidal Cores, Journal of Electrical Engineering, Vol. 55, No. 10/S, pp. 95–96, 2004

[2.22] G. Bertotti, Histeresis in Magnetism, Academic New York, 1998

[2.23] D. C. Jiles, Introduction to Magnetism and Magnetic Materials, Chapman and Hall New York, 1991

[2.24] S. Zurek, T. Kutrowski, A. J. Moses, P. I. Anderson, Measurements at Very Low Flux Density and Power Frequencies, Journal of Electrical Engineering, Vol. 59, No. 7/S, pp. 7–10, 2008

[2.25] E. C. Cherry, The Duality Between Interlinked Electric and Magnetic Circuits and the Formation of Transformer Equivalent Circuits, Proceedings of the Physical Society, Sec. B, Vol. 62, No. 2, pp. 101–111, 1949

[2.26] W. M. Flanagan, Handbook of Transformer Design & Applications, Second Edition, 1993

[2.27] D. C. Jiles, D. L. Atherton, Theory of Ferromagnetic Hysteresis, Journal of Magnetism and Magnetic Materials, Vol. 61, No. 1–2, pp. 48–60, 1986

[2.28] I. Mayergoyz, Mathematical Models of Hysteresis, Physical Review Letters, Vol. 56, No. 15, pp. 1518–1521, 1986

[2.29] U. D. Annakkage, P. G. McLaren, E. Dirks, R. P. Jayasinghe, A. D. Parker, A Current Transformer Model Based on the Jiles–Atherton Theory of Ferromagnetic Hysteresis, IEEE Transactions on Power Delivery, Vol. 15, No. 1, pp. 57–61, 2000

[2.30] A. Rezaei–Zare, R. Iravani, M. Sanaye–Pasand, H. Mohseni, S. Farhangi, An Accurate Current Transformer Model Based on Preisach Theory for the Analysis of Electromagnetic Transients, IEEE Transactions on Power Delivery, Vol. 23, No. 1, pp. 233–242, 2008

[2.31] L. A. Kojovic, Comparison of Different Current Transformer Modelling Techniques for Protection System Studies, Power Engineering Society Summer Meeting, Vol. 3, pp. 1084–1089, 2002

[2.32] F. Lorito, Identification of a Grey–box Model of Nonlinear Current Transformers, Control Engineering Practice, Vol. 6, No. 11, pp. 1331-1339, 1998

[2.33] F. C. F. Guerra, W. S. Mota, Current Transformer Model, IEEE Transactions on Power Delivery, Vol. 22, No. 1, pp. 187–194, 2007

[2.34] K. Draxler, R. Styblikova, Influence of Instrument Transformers on Quality of Electrical Power and Energy Measurement, IEEE International Symposium on Industrial Electronics, pp. 1317–1321, 2007

[2.35] postnote, UK Electricity Infrastructure, Parliamentary Office of Science and Technology, No. 280, February 2007

[2.36] B. L. Capehart (editor), Encyclopedia of Energy Engineering and Technology, Vol. 2–3, CRC Press, 2007

[2.37] K. Iwansson, G. Sinapius, W. Hoornaert, Measuring Current, Voltage and Power, Handbook of Sensors and Actuators, Vol. 7, Elsevier, 1999

[2.38] S. Ziegler, R. C. Woodward, H. H. C. Iu, L. J. Borle, Current Sensing Techniques: A Review, IEEE Sensors Journal, Vol. 9, No. 4, pp. 354–376, 2009

[2.39] S. Tumanski, Induction Coil Sensors – a Review, Measurement Science and Technology, Vol. 18, No. 3, pp. R31-R46, 2007

[2.40] Practical Aspects of Rogowski Coil Applications to Relaying, IEEE PSRC Special Report, 2010

Chapter 3

The magnetisation measurement system

Magnetic characteristics of a material are usually determined by magnetising a sample and measuring its response in the form of flux density. The aim is to record BH loops, from which magnetic properties can be derived. The procedure is standardised to allow comparable results of a specific type test under controlled conditions. For the purposes of this investigation, the power loss and permeability were to be accurately measured over a range of flux densities (0.5 mT to 1 T, or a wider range) under 50 Hz excitation. The measurement of low flux density magnetic properties is considered difficult [3.1] due to the feeble signals and low signal-to-noise ratio [3.2]. The amplitude of the waveforms to be measured and the implications on instrumentation requirements is discussed in section 3.2.

The design of the developed measurement system is based on one previously used for investigation of electrical steels behaviour in low flux densities [3.2]. The aim was to improve the test duration, accuracy and versatility by reducing the electromagnetic noise, improving of signal-to-noise ratio, a higher resolution equipment and a sample holder including coils (magnetising and sensing). Digital compensation was designed and incorporated into the control application to reduce the search coil resistance, reduce the electromagnetic noise, and thus enhance the system performance. Additional features included digital triggering and modified digital feedback algorithm.

The developed measurement system facilitates testing of Single Epstein Strips and connects to an Epstein frame or toroidal samples.

3.1. Existing system for low flux density measurements

In the work on anomalous behaviour of electrical steels by Zurek et al. the authors point out the potential shortcomings of low flux density measurements of electrical steels up to date, open magnetic circuit and apparatus used [3.2]. The authors made an attempt to measure magnetic properties of Epstein strips in a single strip tester, a standardised method used at high flux densities [3.3]. The paper includes results of measurements in a wide range of flux densities, down to 10 μT, which satisfies well the requirements of the work being presented in this thesis. However, the system analysis presented below identified the following limitations:

- the reliability is limited to measurements above 1.5 mT;
- the duration of a measurement is unacceptable to be employed in testing of high number of samples;
- the setup lacks arrangement for sample swapping.

The potential challenges in building a new system are:

- minimisation of noise,
- programming knowledge required to modify the complex software employing advanced functions.

In their article Zurek et al. described a system consisting of several components (Figure 3.1) serving the following purposes:

- PC with Labview software for measurement control and analysis
- Data Acquisition Card (DAQ) for measurement and generation of signals
- power amplifier to provide the necessary magnetising field
- isolating transformer as a DC filter
- Single Strip Tester (a sample with the primary and secondary coil wound on it and C yokes as a means of closing the magnetic circuit).

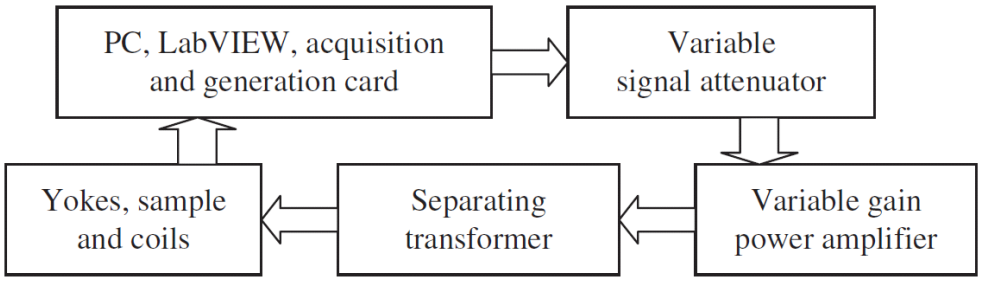

Figure 3.1 Block diagram of a digital SST system used by Zurek et al. [3.2]

The magnetising and sensing winding were placed directly on the sample preventing any air gap and hence no air compensation was required. The disadvantage of such solution is that the windings could not be utilised for measurements of any other samples.

In order to assess the suitability of the electronic instrumentation to perform the measurement, I calculated, based on the data included in the article, the amplitude of the lowest voltage signal induced in the search coil that needed to be measured [3.4]:

$$V_{pk} = 2\pi f B_{pk} NA \approx 20\ \mu V \tag{3.1}$$

f – frequency of the signal (20 Hz)

B_{pk} – the lowest expected peak value of flux density (10 μT)

N – number of turns in a search coil (2000)

A – cross–sectional area of the ‚sample (≈ 30 x 0.27 mm)

According to the specification of the DAQ used, PCI6115 the sensitivity (the minimum voltage change in the signal that can be detected) is 98 μV [3.5]. As the amplitude of the measured signal is about 5 times smaller than the smallest voltage the device can sense and discriminate, it is impossible to complete the measurement without further aid. In this case this appears to be the averaging that is specified in the article to be up to 1000 readings. It has previously been found that averaging a signal with sufficient amount of white noise performs comparably to intentional dithering and averaging, resulting in effective increase of measurement instrument resolution [3.6]. In this case, the resolution is expected to have increased from 12 bit to 16 bit, and hence allowing discrimination of signal levels of 6.1 μV:

$$S = \frac{range}{2^{reslution} - 1} \approx 6.1\,\mu V \tag{3.2}$$

S – sensitivity of an instrument

range – measurement range of between the max and min measurable value

resolution – resolution of the analogue to digital converter (ADC)

It is shown in Figure 3.2 that the DAQ with the employment of dithering and averaging as used in [3.2] must have produced a significant quantisation error in the measurements at the lowest flux density. Even 21 bit resolution DAQ would generate a visible quantisation error and up to 1% amplitude error related to the DAQ sensitivity. Hence 22 bit or higher resolution DAQ is favoured of which sensitivity would be more than 200 bigger than the signal amplitude. Similarly, it can be shown that the equipment used in [3.2] with the stated averaging of 1000 cycles offers sufficient sensitivity above 1.2 mV corresponding to about 600 μT.

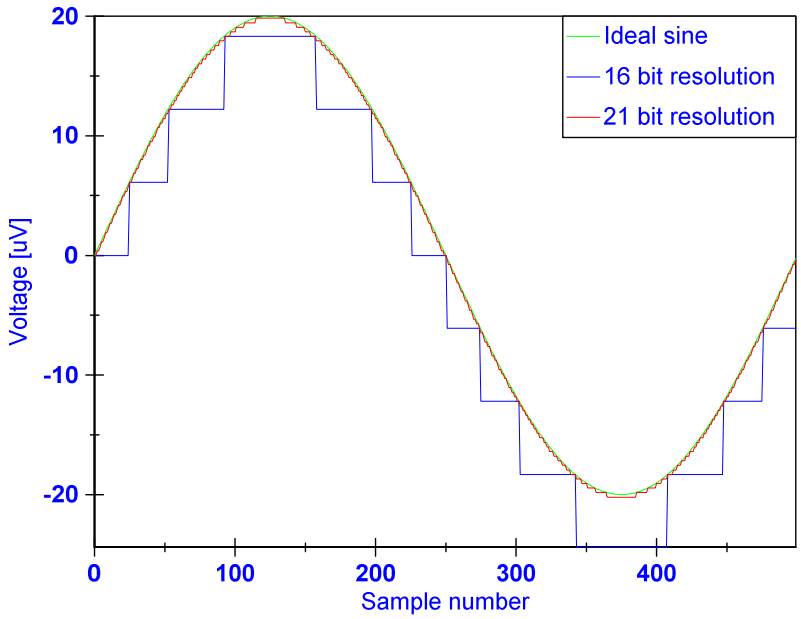

Figure 3.2 Simulation of quantisation of a 20 μV amplitude sinusoidal signal by DAQ PCI6115

Periodic averaging used in [3.2] is an effective tool for improving the signal-to-noise ratio. However, it relies heavily on the assumption that all the noise is random (Gaussian noise). Other, non-random components of the noise, e.g. power frequency interference, will not be eliminated by averaging and will cause a distortion to the measured signal [3.7]. When a considerable amount of

Gaussian noise is present in a signal being measured, which appears to be the case in [3.2] based on the amount of averaging cycles used, the non-random components may not to be visible.

In the simulation of quantisation of the PCI6115 shown in Figure 3.2, a sinusoidal signal was chosen as a representative type of the expected waveform. However, it is important to note that due to finite accuracy of the acquisition in time domain, an extensive averaging will 'smooth out' any potential high order harmonics present in the signal [3.8].

The duration of a measurement is another parameter of the system affected by the high number of cycles averaging. In the worst case, averaging of 1000 cycles of 20 Hz frequency signal, a single waveform reading required 50 s. As the system software algorithm performs calculations and magnetising field signal adjustments on an iteration per iteration basis, a measurement at a single desired peak flux density may take tens or hundredths of repetitions, corresponding to a time delay of 10 minutes to few hours. Performing one magnetic test on a single sample in a range of flux densities can easily take a day of running the system.

Considering the above implications of high-count averaging, it can be concluded that although the technique reduces white noise and can increase the sensitivity of the acquisition equipment, it may result in inaccurate measurements, at the same time requiring unacceptable testing time. At reduced averaging cycles number (100-150) the sensitivity of the equipment being assessed would reduce to about 12 μV, allowing measurement of signals of 2.5 mV peak value.

3.2. Equipment selection for new system

In order to select a suitable equipment, an estimate of the lowest signals to be measured was vital. The SST measurement was expected to be challenging because in the Epstein test the cross–sectional area of a sample is at least three times, and in the case of toroids significantly, higher than in the SST test. The

amplitude of the sinusoidal voltage expected to induce in the secondary winding of the SST when a sample is magnetised to the peak flux density of 0.5 mT can be found from the equation (3.1) assuming the following parameters: 50 Hz frequency, 0.5 mT peak flux density, 1000 turns search coil and 30 mm wide, 0.27 mm thick sample; this is 1 mV. Acquisition of such a waveform with a sufficient precision requires an instrumentation with the sensitivity of 6 μV or better.

Independent of the instrumentation precision, it is of paramount importance to reduce the noise in the signals to be measured as concluded in section 3.1.

3.2.1 Data Acquisition Card

It has been shown by Zurek et al. [3.6] that dithering and averaging can be used to improve the sensitivity of digital acquisition devices. Nonetheless it leads to unacceptable testing time length and affects the accuracy. Higher resolution equipment was expected to increase the credibility of results and shorten the testing time from a few hours to a few minutes, making ongoing testing feasible.

Digital data acquisition equipment which would possess the following characteristics had to be acquired:

- simultaneous sampling for preserving the interchannel phase relationship [3.10]
- ultimate resolution for accurate low level measurements
- at least one output and two input channels
- non–PC housed for noise minimisation

Products offered by National Instruments were investigated and two models were selected, i.e. DAQ 6120 and DSA (Dynamic Signal Analyser) 4461, each available as a PCI extension card and a purpose built chassis module. The latter form was recommended by the manufacturer. This way, an acquisition device works in a predictable environment, hence the measurements are more accurate. This solution does not imply using an expensive PXI Embedded Controller (complete PC system contained in the PXI chassis) as there are

Remote Controllers available, making PXI modules accessible for a PC as if they were PCI modules directly installed in the computer. The 5–Slot PXI-1033 Chassis with an Integrated MXI–Express Controller (shown in Figure 3.3) and an PCI Express Card installed in a desktop PC were utilised for the investigation [3.11].

Figure 3.3 DSA card installed in the PXI-1033 chassis with wiring to the other components of the measurement system

According to the Data Acquisition Product Families Comparison, the DAQ 6120 is characterised by the best dynamic accuracy and simultaneous sampling features. The DAQ has four 16 bit analogue inputs and two outputs. With 8 ranges, the smallest being 0.2 V and the highest 42 V, the card allows for the widest range of measurements of all DAQs.

The second card of interest, DSA 4461, belongs to a group of products called Sound and Vibration Measurement Hardware which can acquire signals with 24–bit resolution compare to 16 bit of the 6120 card. The module consists of two inputs and two output channels, all simultaneously sampled. Specification of the card shows in the lowest range –316..316 mV sensitivity of 37.7 nV (compare to 6 μV of the 6120 or 100 nV of commonly employed in laboratory setting Keithley multimeters).

Explicitly for low–level measurements, NI provides an apparatus under the term "Signal conditioning". Using signal conditioning to amplify the signal level (to match the analogue–to–digital converter range) increases the measurement sensitivity. In addition, external signal conditioners located closer to the signal source improve the measurement signal–to–noise ratio by boosting the signal level before it is affected by environmental noise. The only amplifier identified as offering simultaneous sampling was the NI SCXI–1140, 8–channel differential amplifier module with switch–selectable gain (1, 10, 100, 200, or 500). The SCXI system consists of a shielded chassis that houses required modules and can also operate as a front–end signal conditioning system for PCI, PXI, or PCMCIA data acquisition devices. There is also the possibility to accommodate SCXI and PXI devices in a PXI/SCXI Combination Chassis [3.12][3.13].

The Dynamic Signal Analyzer PXI 4461 was chosen as the sensitivity of the 6120 card is at the limits required. Through its embedded amplifiers it is capable of measuring signals as low as ≈ 38 nV. In this way no signal conditioning equipment is necessary to amplify measured signals in order to better match the analogue–to–digital converter (ADC) range. The PXI housing allows the card to be placed close to a signal source and away from sources of the electromagnetic interference. The maximum sampling speed is over 200 kS/s which allows more than 4000 points being recorded per cycle while measuring signals of 50 Hz [3.14]. As the specification of the DSA 4461 exceeds the requirement, reliable measurements in an extended range of flux densities was predicted. This would facilitate future studies of materials low flux density behaviour.

3.2.2 Power amplifier

The main purpose of the developed system was low flux density testing, but high flux density capability was also desirable. This requires a substantial amount of power, which can be delivered by means of a power amplifier. Taking into account reported problems with driving inductive loads from commercially available amplifiers [3.15], the Crown Macro–Tech model MA–5002VZ was favoured. Through its patented Variable Impedance System, it is

capable of operating under low, active, as well as reactive loads. The amplifier has numerous safety and protection features to minimise the possibility of damage [3.16]:

- circuitry which limits the drive level placed on the output devices before their safe operating area is exceeded
- radio frequency interference burnouts and output current overload protection

3.2.3 Sample enclosure and coils

The system was required to be sufficiently versatile, for the magnetic properties of Epstein strips to be easily measured without the need of winding coils on each sample for SST testing. This was addressed by placing windings on a former with dimensions shown in Figure 3.4. The 1009 turn coil was wound with a one uniform single layer of 0.15 mm diameter insulated copper wire, without overlapping or crossing of any turns. A single layer, 97 turn magnetising coil was wound on top of the search coil.

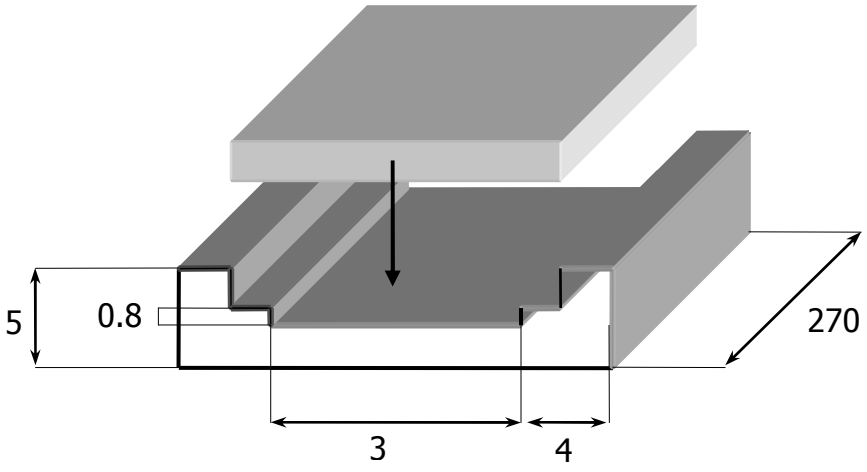

Figure 3.4 Sample enclosure design (dimensions in mm)

In the case of toroidal samples, a flat ribbon cable terminated in series configuration was used to reduce the time and effort required to wind a secondary coil. In the same way, a set of either three or five cables was utilised to form the magnetising winding.

3.2.4 Current shunt

For measuring the exciting current, a Tyco Electronics BDS2A1004R7K non–inductive shunt of the following specification was acquired:

- less than 40 nH inductance; this corresponds to a reactance of 12.6 μΩ at 50 Hz and therefore adds virtually no error to the amplitude or phase of the measured current;
- resistance of 4.74 Ω was chosen for testing core samples, to ensure that the shunt and search coil voltage were of the same order of magnitude; 0.5 Ω was found suitable for SST testing;
- 100 W power rating;
- low Temperature Coefficient of Resistance (TCR) equal 150ppm/°C.

Low TCR was sought to ensure that changes in the shunt temperature will not impair the overall accuracy of the system. A TCR value of 150ppm/°C means that the measured voltage can cause ≈ 0.15 % error in current reading for every 10°C temperature change. This can be an issue only when testing strips at high flux density using the SST due to high exciting current of a few amperes.

The shunt was attached to a heat sink (Thermo Electric Devices TDEX3132/100) in conjunction with silicon based thermal grease.

3.2.5 Measurement setup

All components of the system were connected as shown in Figure 3.5. Twisted wires were used for measuring signals leads to minimise electromagnetic interference. Twisting wires is a common technique and has two effects. It minimises the loop of a conductor in which an electromagnetic field induces an unwanted signal which is proportional to the area of that loop. Secondly, induced signals in consecutive loops cancel each other due to the opposite polarity [3.17].

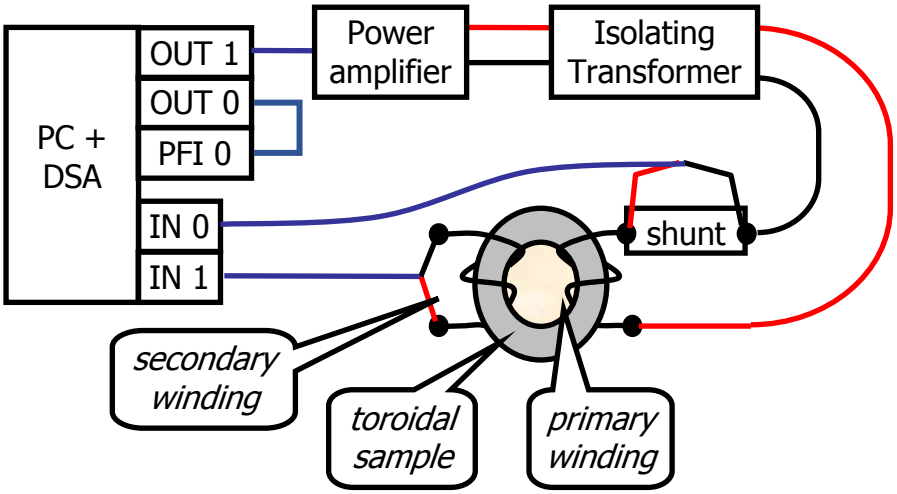

Figure 3.5 Schematic diagram depicting the wiring of the setup

The sample, the isolating transformer and the magnetising circuitry were placed in the anechoic chamber (ferrite tiles lined walls) to reduce the electromagnetic noise. At the same time the components of the system were separated from other EMI sources (e.g. computers, electrical office appliances, fluorescent lights).

In the course of testing at low flux densities, the amount of distortion and power frequency interference was found to be unacceptable. The power frequency being different from 50 Hz produced by DSA, and at the same time varying continuously with time, caused the distortion to drift in either direction with reference to the system trigger. Subsequently, this leads to a feedback control malfunction, hence preventing the measurement criteria from reaching satisfactory values. An example of a distorted signal induced in a search coil when a power amplifier was used in the magnetising circuit is shown in Figure 3.6 (at approximately 100 μT). While averaging can smooth the waveform, it still requires a harmonic correction (THD = 12%). For comparison, see signal recorded when the TTi function generator TGA 1230 was used to energise the magnetising circuit (THD = 1%). Disconnection of the power amplifier from the circuit resulted in elimination of the signal distortion and significant reduction in noise. It was further found that not all of the function generators have the same low noise characteristics, when the TTi TGA 1241, was employed.

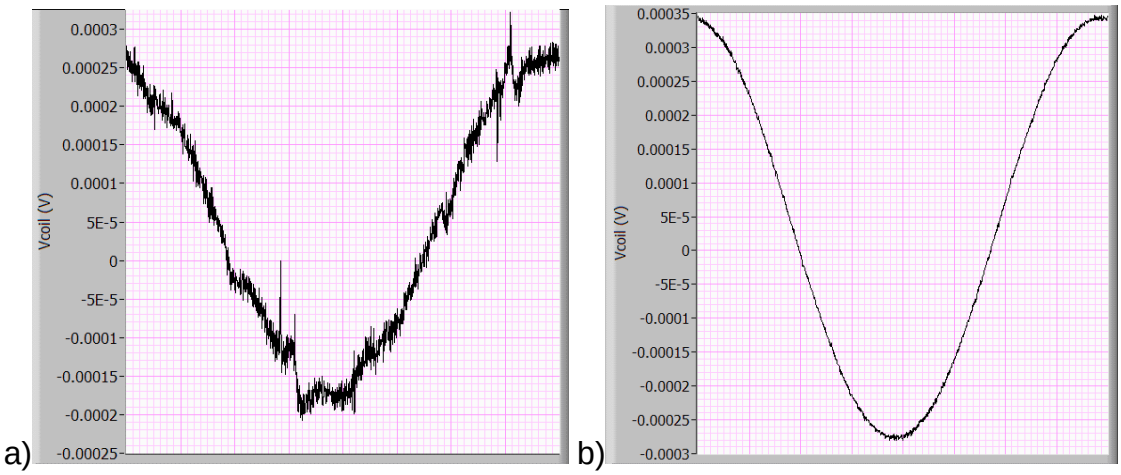

Figure 3.6 The level of distortion observed in the search coil induced voltage of 50 Hz frequency while (a) power amplifier, (b) function generator (TTi TGA 1230) was used in the magnetising circuit. In both cases the averaging was 25 cycles

The experiments with the function generator at low flux densities showed that the power amplifier is not a suitable appliance for use in the magnetising circuit due to noise and distortion issues. Utilising the function generator was also unfeasible because of its control and range limitations. Another solution was to find out details about the amplification stage design of the generator in an effort to construct one that could be used to amplify the DSA output signal. While considering the specification of such an amplifier it was noted that the rated power of the TTi 1230 generator is only 2 W, yet it was still sufficient to saturate the tested sample. The DSA maximum power is an order of magnitude smaller (0.16 W); however it is sufficient to magnetise a sample to 0.1 T. The only technical difficulty was to match the minimum load impedance (600 Ω) of the DSA with the low impedance of the magnetising circuit (5 to 20 Ω). This was accomplished with a matching impedance transformer by the KROHN–HITE, model MT– 56R (600 to 6 Ω). The observed search coil signal featured the same absence of distortion as when the function generator was used to magnetise the sample (see Figure 3.6b). The components of the measurement system placed in the anechoic chamber are shown in Figure 3.7.

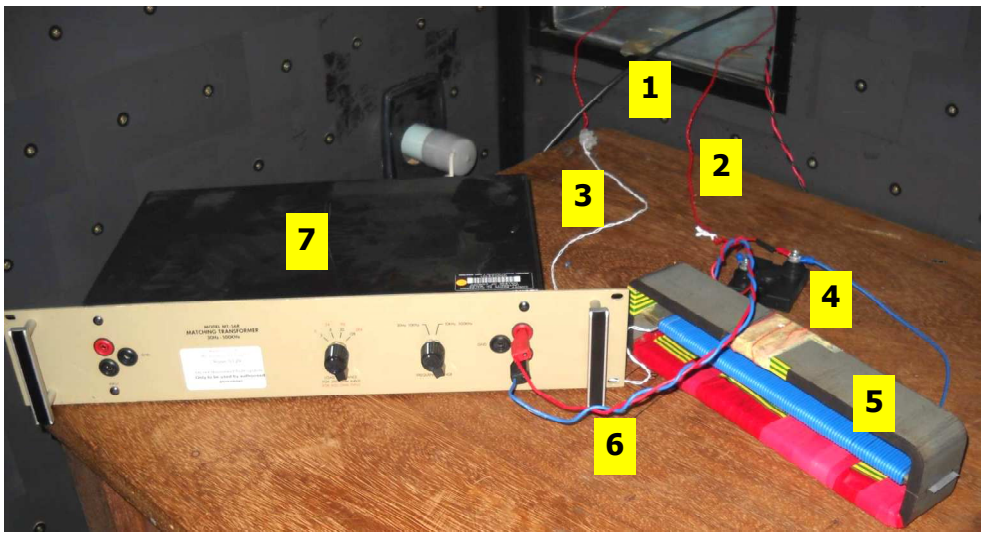

Figure 3.7 Components of the measurement system in the anechoic chamber: 1 – BNC cable connecting the DSA with '7', 2 – shunt voltage lead, 3 – search coil voltage lead, 4 – current shunt, 5 – SST, 6 – transformer output lead, 7 – matching impedance transformer

As a result of the above investigation, the power amplifier and isolating transformer were substituted by a matching impedance transformer (KROHN–HITE MT– 56R) for low flux density testing. Although this solved the distortion problem, the power frequency interference issue remained. It erratically influenced the peak flux density value and made the peak flux density control difficult. For this reason, the SST, sample and matching transformer were placed on top of four rectangular sheets of GO steel, and inside a four layer cylinder (45 cm diameter) made of a GO steel. The shielding arrangement is shown in Figure 3.8.

Figure 3.8 Power frequency shielding used to enclose a magnetic sample and matching impedance transformer. The diameter of the cylinder is 45 cm

Incorporation of the matching impedance transformer and shielding into the system enabled accurate measurements of the BH loops in toroids and strips at flux densities as low as 10 μT and 100 μT, respectively. Furthermore, it reduced the amount of magnetisation control and averaging required, and hence the time to complete a measurement.

The power available from the DSA through the transformer, was not sufficient to conduct a full range flux density test. Consequently, the amplifier had to be reconnected each time a sample required demagnetisation or a high flux density test was to be carried out.

The following summarises the experimental precautions taken to minimise the signal noise:

- twisted connecting wires,
- bias resistors on both input channels [3.18] connected to the acquisition instrument casing shown in Figure 3.3
- use of a matching impedance transformer instead of a power amplifier,
- use of an electromagnetic shielding chamber,
- an additional sample and matching impedance shielding.

3.3. Control application

The control software is an essential part of any PC based testing system. The low flux density system application (tk.VI) controls the generation of the magnetising field, acquisition and processing of signals. It does all the necessary calculations and saves results. Controlling of the measurement system was realised in NI Labview software.

The programming part of the application is accessible through a block diagram view. The control program concise algorithm is shown in Figure 3.9 illustrating the steps following the path of execution which are discussed in the following sections.

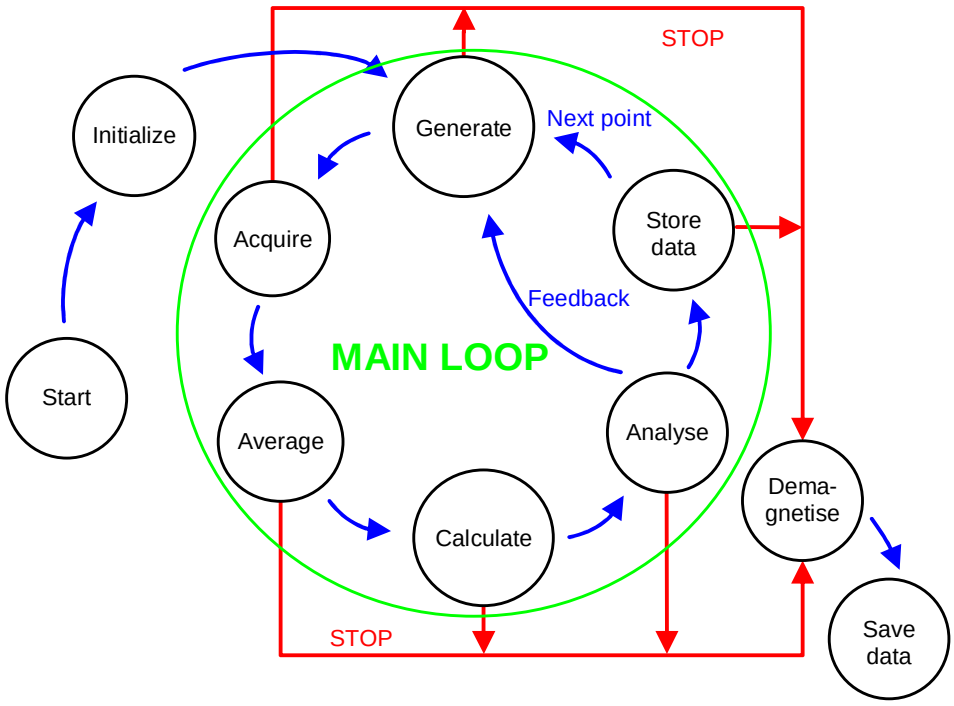

Figure 3.9 Control application state transition diagram

3.3.1 Initialisation stage

When the control application is executed, it follows a list of operations comprising the initialisation shown in Figure 3.9:

- calculation of the acquisition and generation parameters (sampling info, buffer size, see Figure 3.10)

- declaration of the triggering signal (shown in Figure 3.24, discussed in section 3.4.2)
- acquisition and generation options setting (e.g. coupling, sampling rate, buffer size, regeneration mode, triggering; see Figure 3.11)
- data saving preparation (Figure 3.12)
- calculation of the cross–sectional area and magnetic path effective values (Figure 3.13)
- reset of controls and indicators (Figure 3.14)

The number of samples to generate and acquire at 50 Hz is set to the maximum of the DSA [3.14]. This ensures acquisition with a sufficient sampling rate for recording signals up to 102.4 kHz according to the Nyquist theorem. At other frequencies, the number of samples is set to be a constant within specific ranges, as shown in the formula node, in Figure 3.10.

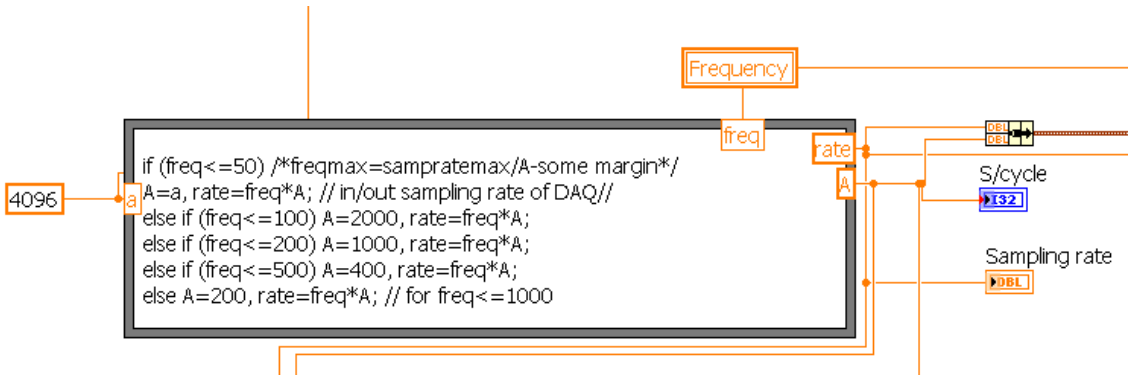

Figure 3.10 Block diagram outlining the calculation of the acquisition and generation parameters

For the maximum number of points per cycle at all frequencies, the formula node calculation must be replaced by following code:

```
A = floor(204800/freq); /* the no. of samples equals the max sampling rate
                           (204.8kHz)/the desired freq. of signal, rounded to
                           the nearest integer towards –inf */
rate = A*freq; /* the sampling rate equals number of samples times freq.
                  of the signal
```

The configuration process of generation and acquisition channels is shown in Figure 3.11. The gain of the output channel for generating the magnetising field

is set according to user operated control. The generation on both channels is configured to run continuously at a requested speed and starts before the main loop. The acquisition is set to measure a finite number of samples at a time (one period) starting with trigger signal present on the PFI0 input channel. The sampling frequency is equal to that of generation. DC coupling was selected since there is an insignificant amount of DC offset voltage and, in any case, any offset would be removed during data processing in the program. Furthermore, DC coupling eliminates the problem of settling time introduced by the RC filter in AC mode [3.19].

The acquisition task is transferred into a "reserve" state outside the main loop for optimum performance between consecutive acquisitions.

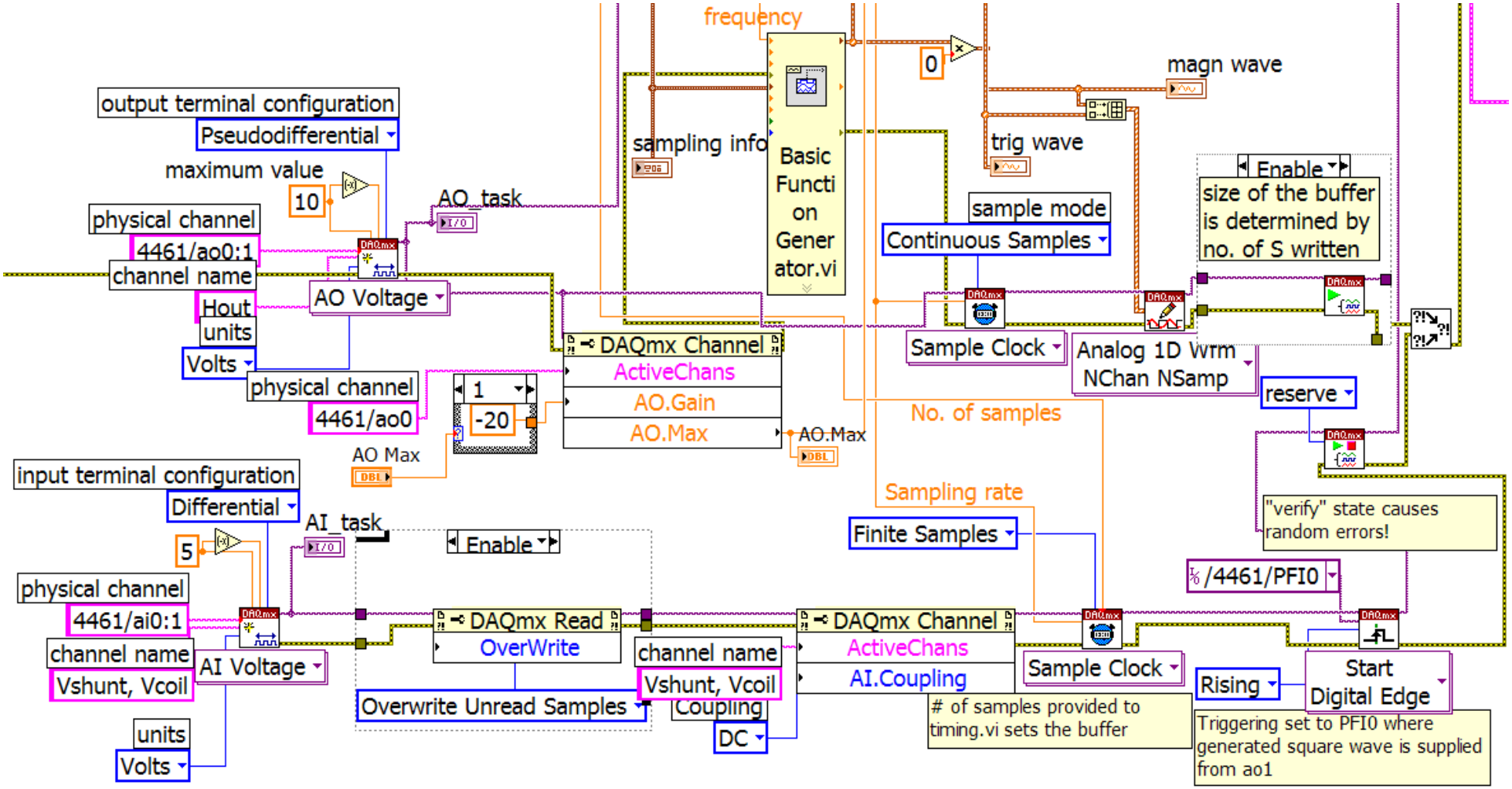

Figure 3.11 Block diagram of the DSA channels configuration

Another step of initialisation is the preparation of temporary files for streaming data to disk (Figure 3.12). If old files exist, they are deleted and replaced. The file path provided by the user is also verified and a folder created if necessary.

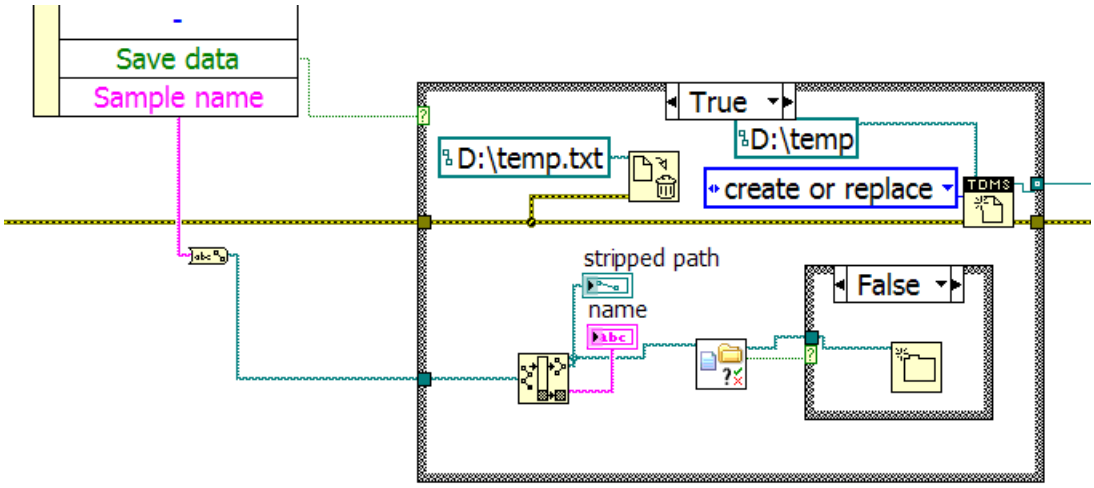

Figure 3.12 Block diagram outlining the preparation for data saving

The effective value of sample parameters is calculated from the user-inputted specification. In Figure 3.13, the block diagram shows sample dimensions being extracted from a cluster, converted from physical into pure number, and used subsequently to determine the effective values of the magnetic path and cross-sectional area.

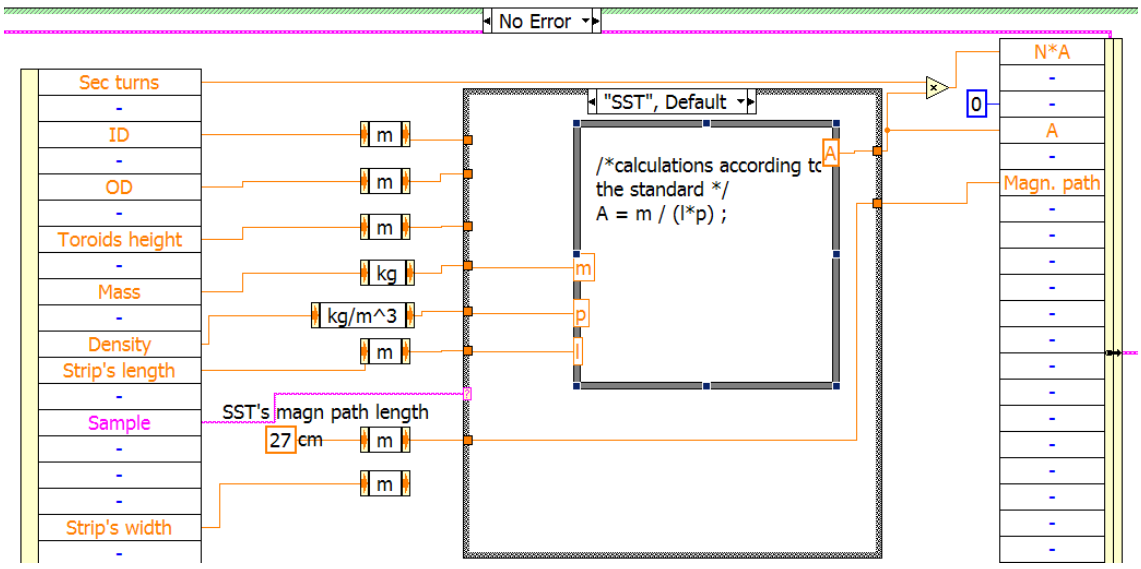

Figure 3.13 Calculation of the effective values of sample parameters

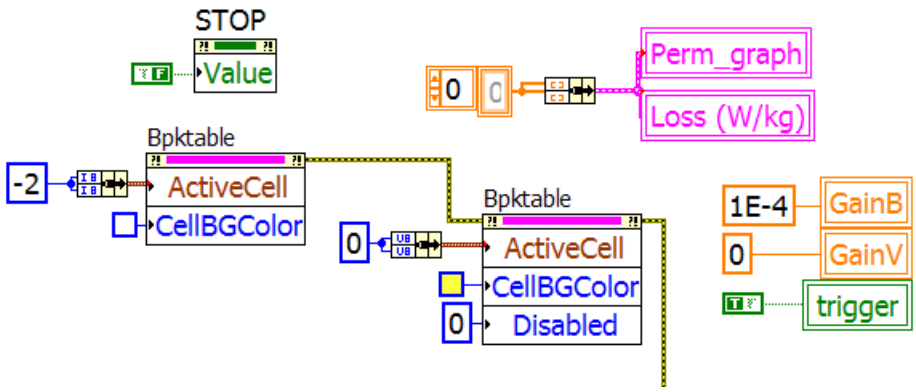

Figure 3.14 Resetting the controls and indicators operation

3.3.2 Generation

The first signal that is generated after the execution of the control application is a sine wave of zero amplitude. In the following iterations the magnetising field signal is computed according to the feedback algorithm or, in the case of the test mode, a sine wave of user-controlled amplitude is used. Prior to writing the data to the generation buffer, the signal is verified against two criteria. THD of the waveform is checked in case the feedback control becomes unstable. If the value is higher than 60% then the test is stopped. Secondly, the signal amplitude must fall within the voltage range of the DSA card, otherwise the signal is normalised. The overwriting of the buffer is omitted when there has been no change made to the output signal since the preceding buffer update.

The generation of signals in the software is set to user buffered regeneration. In this mode the signals created in a control application are first written to a buffer located in the computer memory and subsequently transferred to the DSA onboard memory. The transfer between the two buffers is continuous in a loop as the onboard buffer empties in time while the card carries out the generation. Thus, signals are regenerated until the user buffer is updated by the control program. The drawback of this arrangement is that the time delay between the update of the user buffer and the actual generated signal is uncertain. This might result in several acquisitions taking place before the actual change in the magnetising field signal. Consequently, that creates a sort of inertia problem for the control algorithm that can be seen as overshooting the target flux density

during the measurement. There is no doubt that it has other implications which impair the control feedback. The non–regeneration mode was attempted in order to resolve the problem. Nonetheless, it quickly emerged that the non–regeneration mode puts great demand on the PC resources since the DSA must be fed continuously with new samples. Whenever these have yet to be sent to a buffer an error occurs and generation stops. Eventually, it was decided to use the regeneration mode and thus the inertia issue had to be accounted for in the feedback control algorithm.

Two signals are generated during the measurement, namely the magnetising and triggering signal waveform. The latter does not change through the measurement and thus at low flux densities, it is an order of magnitude greater than the magnetising signal. Taking into consideration the crosstalk phenomenon, the generation of the trigger was set up on the furthest channel of the two outputs, which is AO1. For clarification, the BNC terminals on the DSA front panel are laid out vertically in the following order, starting from the top: PFI0, AI0, AI1, AO0, AO1. The amount of crosstalk observed on AI1 while triggering was set up on AO0 (adjacent channel) is shown in Figure 3.15. None was detectable on the non–adjacent input, AI0.

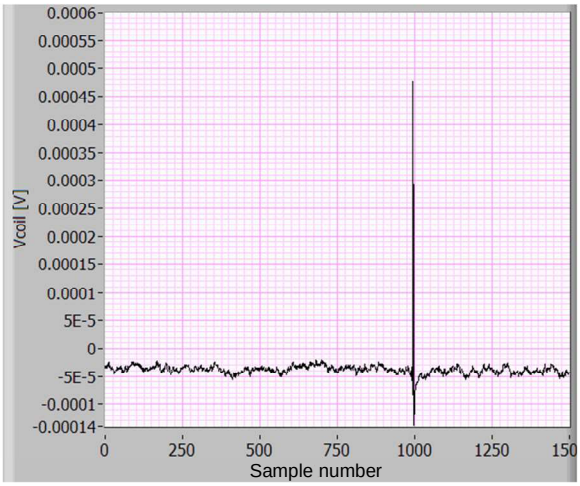

Figure 3.15 Graph illustrating the amount of crosstalk from output to adjacent input channel while triggering signal being generated

3.3.3 Acquisition

The acquisition of signals is organised into two parts, the input voltage range selection and the measurement. The first ensures that the measurement is carried out with the maximum sensitivity and, at the same time, no clipping occurs. This is done through a single acquisition of signal one cycle and gain adjustment. The below code is utilised in selecting the right range for both input channels:

```
int8 G, K, e;  //numeric representation of output variables
K=in/42.4*100;  /*percentage indicator of max voltage
                  "in" is the signal pk value */
x=in*1.02; // add 2% margin
/*choice of range of DAQ according to specification of 4461*/
if (x<=0.316) G=30, e=0;          //G=gain
else if (x<=1) G=20, e=0;         // e=0 =>NO error
else if (x<=3.16) G=10, e=0;
else if (x<=10) G=0, e=0;
else if (x<=31.6) G=–10, e=0;
else if (in<=42.4) G=–20, e=0;
else G=–20, e=1;  //measured signal is out of range, create error
```

If the measured signal is of higher amplitude than the maximum voltage range of a channel, an error is created causing the control application to stop and alert the user of the problem. The procedure of changing the input voltage range of the DSA is shown in Figure 3.16.

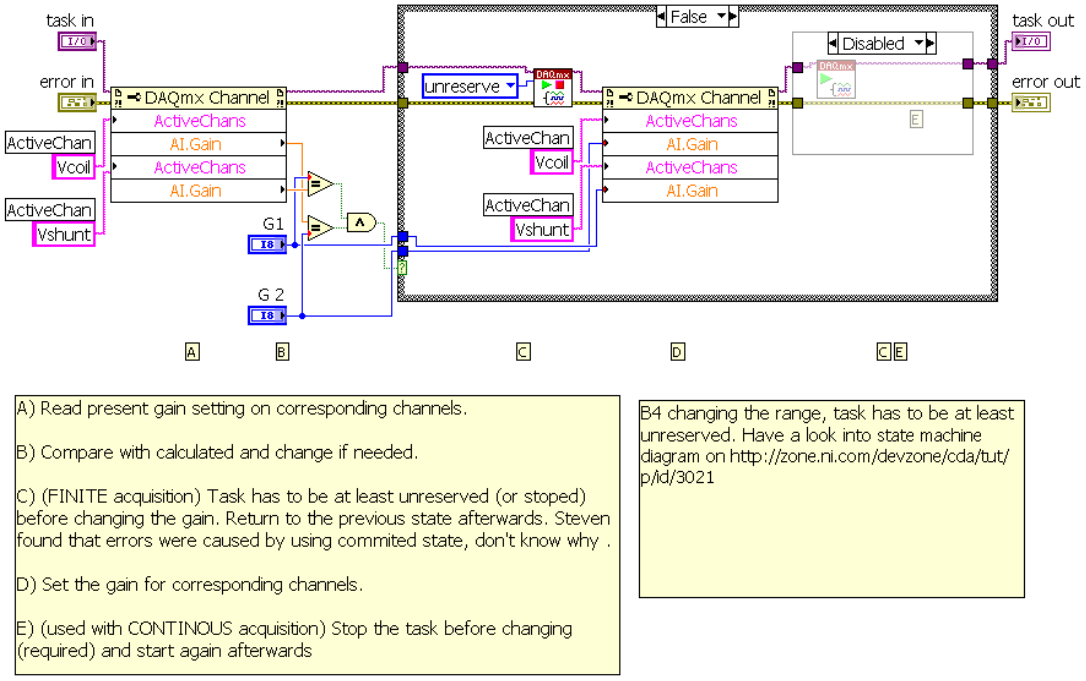

Figure 3.16 Block diagram of the 'range_change' subVI showing the necessary steps for updating the amplification of the DSA

3.3.4 Averaging

The averaging is a digital signal processing technique most commonly used in measurement of periodic signals. Together with other mechanisms, this can improve an ADC sensitivity [3.6][3.20]. Since the DSA used in the system has supreme sensitivity, the averaging is used as a white noise filter. The maximum effective number of cycles used is 250, at low flux densities (input voltage below 0.1 mV). This decreases to 50 with rising search coil voltage. As expected, there was no significant effect observed above the 250 periods. The averaging number required equals the square of the amount of noise suppression, hence in order to double the effect of averaging, over 1000 cycles would have to be used. This would lead to unfeasible testing times.

The noise reduction after averaging was found to be reduced significantly when the output channel was set to the maximum voltage range (Figure 3.17a) compared to others. In the highest voltage range, the sensitivity of the DAC is insufficient. This causes glitches in the generated signal and a "staircase–like looking" waveform. The phenomenon was observed previously and its effect evaluated by Matsubara et al. [3.21]. It is therefore important to set the voltage

range of the corresponding channel to a lower setting when producing signals of less than 10 mV amplitude (Figure 3.16b).

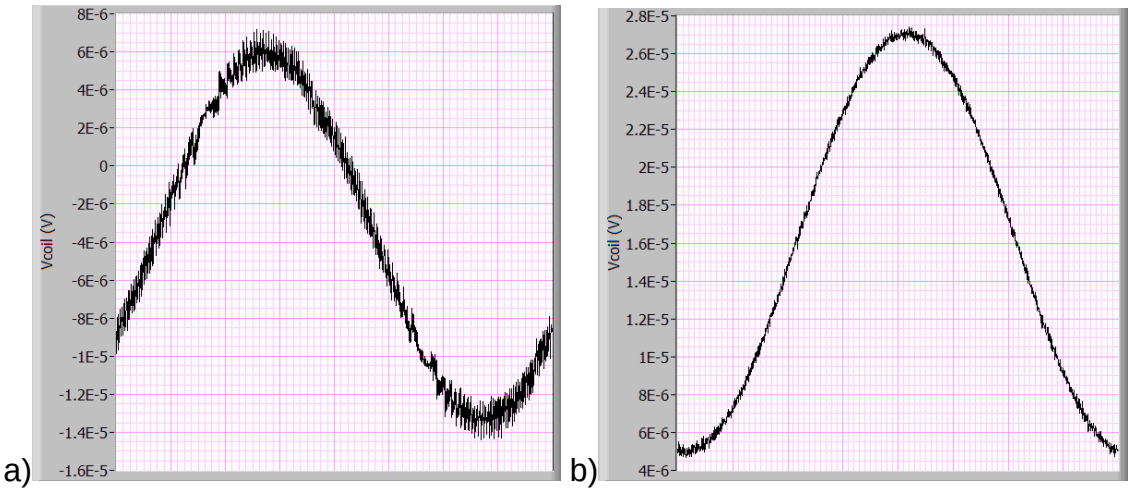

Figure 3.17 Illustration of the averaging impaired by the low sensitivity of the magnetising field (averaging is 150)
a) output range 10 V, b) output range 1 V

The number of cycles used for the averaging can be automatically controlled by the program algorithm (see latch aver button on the front panel diagram, shown in Figure 3.19). In this way the maximum averaging number is used only when the search coil signal meets the set criteria. Otherwise, the number is adjusted depending on the amplitude of the signal.

In addition to the periodical averaging, a moving average technique was incorporated in the processing of the acquired signals. It involves the calculation of the average value of the neighbouring points in the waveform to obtain the value of n point. It is a simple but effective method for reducing random noise in time domain encoded signals while retaining a sharp step response. Another advantage of this particular filter is the high speed and low computational power requirement recursive algorithm [3.22]. The amount of noise reduction is equal to the square–root of the number of points used in calculating the average.

The maximum recommended number of samples used in moving average is 15 and decreases the noise up to approximately four times. Parameters: THD, FF, Bpk, power loss, and permeability were checked for any effect of the averaging and none was observed. A visual check of the measured waveform averaged

with different number of samples also did not show any decrease in sharpness of the edges. This was conducted at the maximum sampling rate, hence 4084 samples per cycle. For lower speeds, the number of samples used in obtaining the moving average has to be decreased accordingly.

3.3.5 Calculation of the magnetic properties

After the digital processing of the measured signals, the magnetic properties and necessary parameters of the search coil induced voltage are calculated. The following equations are used to derive the flux density and the magnetic field signals:

$$H(t) = \frac{N_F}{l}\frac{V_S(t)}{R_S} \quad \left[\frac{A}{m}\right] \tag{3.3}$$

H (t) – magnetic field

N_F – number of turns in the magnetising field coil

l – effective value of the magnetic path length

V_S (t) – current shunt voltage

R_S – shunt resistance

$$B(t) = \frac{1}{N_C A}\int V_C(t)\,dt \quad [T] \tag{3.4}$$

B (t) – magnetic flux density

V_C (t) – voltage induced in the search coil

N_C – number of turns in search coil

A – cross–sectional area of the sample

The magnetic properties of interest, namely relative magnetic permeability and power loss, are calculated as follows:

$$\mu_r = \frac{B_{PK}}{H_{PK}\mu_0} \tag{3.5}$$

B_{PK}, H_{PK} – peak values of flux density and magnetic field

$$P = \frac{N_F}{m_e N_C}\, f\int V_C(t)\frac{V_S(t)}{R_S}\,dt \quad \left[\frac{W}{kg}\right] \tag{3.6}$$

m_e – effective mass of the sample

The parameters vital to evaluate the measurements are: search coil voltage form factor and total harmonic distortion, measured flux density percentage error related to set value. The formulae used are shown below:

$$FF_{\%error} = \frac{1.11 - \frac{V_{C\ RMS}}{V_{C\ AV}}}{1.11} \cdot 100\% \tag{3.7}$$

$$THD_{\%} = \frac{\sqrt{\sum_{n=2}^{\infty} V_n^2}}{V_1} \cdot 100\% \tag{3.8}$$

$$B_{PK\ \%error} = \frac{B_{PK\ set} - B_{PK\ meas}}{B_{PK\ set}} \cdot 100\% \tag{3.9}$$

3.3.6 Analysis of the measured signals

Once the calculations are complete the results are displayed on the front panel in various numeric and graph indicators, as depicted in Figure 3.19. The values of $B_{PK\%error}$, $THD_{\%}$, $FF_{\%error}$ are compared with the previously set criteria. If these match five times in a row, full averaging is employed and the feedback parameters are adjusted so that only the amplitude is corrected as necessary. Rising harmonic distortion was observed without the deactivation of the waveform shape feedback. When the criteria are met at full averaging number, the measurement point is saved and the procedure repeats for the next flux density on the user–input list.

At this stage of the control application loop, the feedback parameters are being adjusted continuously (GainB, Gainlast). GainB, insignificant at the start of a measurement (1E–4), is gradually increased and adjusted in order that that the increase in $B_{PK\%error}$ is about one percent at every iteration. When $B_{PK\%error}$ falls below 3% (close to the desired flux density) the GainB is reset to its initial small value to avoid overshooting the set flux density. Subsequently, it is again increased gradually until the search coil signal matches the $B_{PK\%error}$, $FF_{\%error}$ and $THD_{\%}$ criteria. Below the 3% threshold, the amplitude gain of the previously generated signal (Gainlast) is also being controlled to stabilise the peak value of

the search coil signal while the GainB is increased to high values (up to 40) in order to correct the harmonic distortion.

3.3.7 Digital feedback algorithm

The feedback control is realised as a sum of the previously generated signal and the difference between the desired and the currently measured flux density waveform. Both have their own gain (Gainlast and GainB) which is automatically adjusted to facilitate gradual changes (< 1% amplitude) in the sample magnetisation. It is crucial in this algorithm for the last generated and the correction signal to be in phase. Therefore the phase of them is adjusted little by little (Figure 3.18) before the calculation of a new waveform.

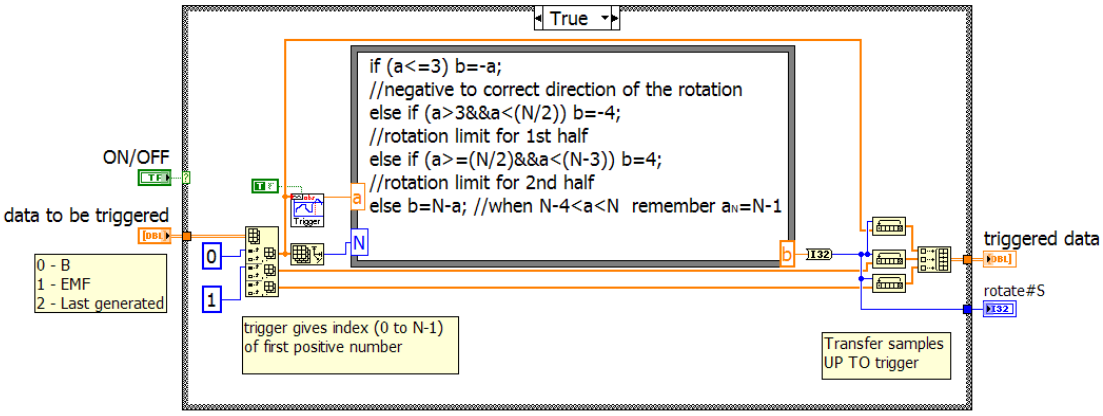

Figure 3.18 Block diagram of the signals phase adjustment for the feedback purposes

The described algorithm performs up to 19 harmonics and the signal is filtered before sending to the DSA buffer. This is sufficient to correct the THD of the search coil induced voltage to a value less than 1%.

3.3.8 Process of demagnetisation

It is a requirement of the magnetic testing standards to demagnetise the test specimen before the measurement. This can be completed by slowly decreasing an alternating magnetic field starting from well above the value to be measured. In the developed program, the demagnetisation takes place at the end of the procedure. The last generated signal is decreased, half a percent every iteration

until it reaches an amplitude of 2E–5 V. At this point the magnetic field acting on a sample is below the noise level.

In order to demagnetise a sample before the measurement, the control application has to be switched to "test" mode (top control of group four, Figure 3.19). The magnetisation level can be controlled with the amplitude manual control (control number five on the front panel). Upon reaching the desired flux density, the STOP button can be pressed and the demagnetisation will follow. The "demag" indicator (indicators group nine in Figure 3.19) shows the progress of the demagnetisation.

3.3.9 Saving of data

The results of a measurement are saved in two different formats for ease of use and to maximise the speed of the application. The basic magnetic properties, such as peak flux density, permeability, and power loss, are saved along with the parameters at which the measurements were taken ($THD_{\%}$, $FF_{\%error}$, $B_{PK\%error}$, averaging used) in a spreadsheet file. This type of file has a small size and can be easily accessed with popular software, e.g. Microsoft Excel. The whole signal waveforms measured and the BHloops are recorded in tdms files. wLabVIEW TDMS is a Technical Data Management and Streaming solution for streaming and organising significant amounts of measurement data. It is designed for high speed recording and processing of data. There is a purpose-made software package, DIAdem, for processing the data saved in this format. Although the files in this format are designed to be used in the special National Instruments software, if necessary, plug–ins for Excel, Matlab and other common data processing packages are available. Due to the amount of data, these files take a significant amount of hard disk memory space [3.24].

Results from each experiment are saved to separate files named as specified by the user in the control application. In case files of the same name already exist, a consecutive number is added.

3.3.10 User interaction with the program

The user interface is accessed through the front panel view (see Figure 3.19). Various numeric and graph indicators allow monitoring of the magnetic properties being measured and the progress of the test. The specification of a sample can be inputted in the relevant numeric controls and the options of the procedure selected by means of numerous switches.

The user interaction starts prior to execution of the control application since a user must provide the specification of a sample and the conditions of the test. The necessary information is sample type dependant and follows the guidelines of the corresponding international standards:

- Single Strip Tester [3.3] requires input of the mass, length and density of a strip. The magnetic path length is set to a value equal to the inside length of the yokes used (27 cm);
- measurement by means of an Epstein frame [3.23] – the mass, length, and density of all the strips together with the number of strips to be tested. The value of the magnetic path length must be updated appropriately;
- toroidal core [3.25] – requires the height, inner and outer diameter.

The above details are necessary for the calculation of the effective values of a cross–sectional area and the magnetic path length. There is other information that must be filled in before starting the program:

- data files' path and name
- list of flux densities at which a sample is to be measured
- number of primary and secondary turns
- desired frequency of the test
- output range of the DSA

The front panel diagram illustrating the layout of the controls and indicators is shown in Figure 3.19 and below is a short explanation of the items in groups marked by numbers.

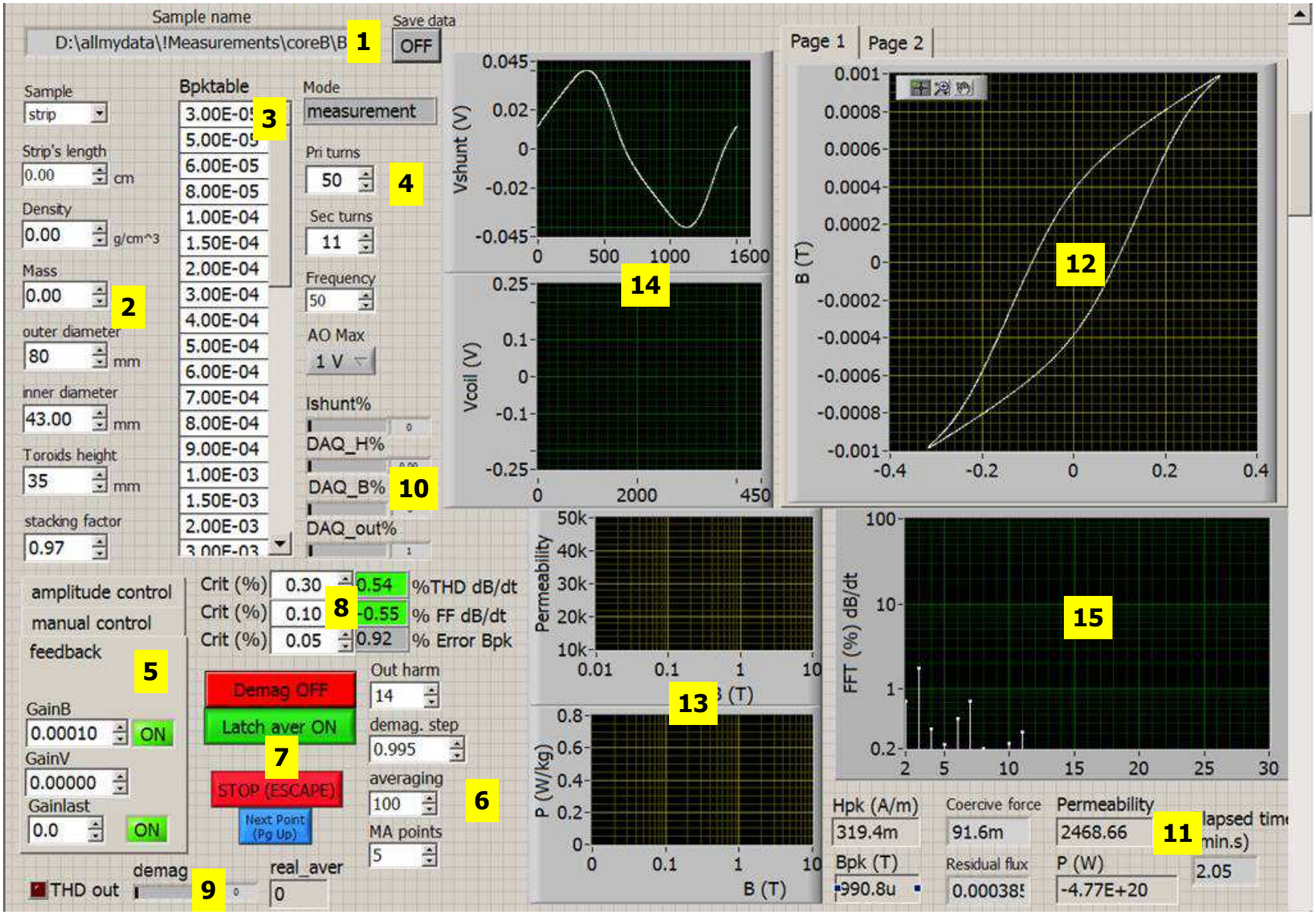

Figure 3.19 Front panel diagram of the control application illustrating the user interface

1 – To the left of the number there is the editable path to the files in which data is to be saved. When files of the same name already exist, a consecutive number is added to the requested filename. To the right of the control is the ON/OFF button for the saving function.

2 – On the left from the top, there are controls in a column for the input of the sample parameters. The type of a sample determines which of them are used as follows: strip (length, density and mass), wound toroid (density, mass, outer and inner diameter), powder materials toroid (height, outer and inner diameter).

3 – The table contains a list of peak flux density values at which a test is to be conducted and can be altered throughout the measurement. There was also a feature added for reading the test points from a file.

4 – To the left of the number there is a column of controls for setting the number of turns, frequency and output range. The highest maximum output is used with a matching impedance transformer to obtain the highest power. Otherwise it should be set to the medium voltage range (1 V) to avoid quantisation error from occurring at low flux densities.

5 – Feedback controls are divided into three groups. **Amplitude control** is, as the name suggests, a mode in which the amplitude of the signal is controlled to induce a desired flux density, irrespective of the waveform shape. In **manual control** the output signal amplitude can be manually adjusted which can be used for demagnetisation, compensation setup and quick checks. The **feedback** card consists of two buttons for switching between automatic operation and numeric controls for manual adjustments.

6 – At column six there are four controls. The top is the output harmonic limiter, which should normally be kept below 19, otherwise the feedback algorithm is not performing. The demagnetisation step is currently set to a 0.5 % drop in the output signal amplitude every iteration, which is well above the requirements laid down in international standards. Averaging can be adjusted according to the requirements. It is subjected to automatic control throughout the test. There is also another type of averaging in this program

used for conditioning the acquired signals, known as the moving average. It has proved very effective in reducing the noise and at the same time, it does not affect the time and feedback control. It was found that up to N/270 (where N is the number of samples per cycle) points can be utilised in this type of averaging without affecting results (15 points for 4000 samples per cycle).

7 – The four buttons marked by 7 are from the top: the ON/OFF demagnetisation procedure, the averaging automatic control, the STOP button, the approval of the current measurement and switch to the next flux density point.

8 – Here are lumped together indicators and controls of the dB/dt waveform distortion along with the peak value error. It can be specified here what is the limit of distortion and how far from the requested flux density value the measurement can be taken.

9 – From the left there is the warning indicator for excessive THD distortion of the signal being generated, the demagnetisation progress, and the last indicates the number of cycles used for averaging for the most recently acquired data.

10 –These indicators show the output and input levels.

11 –Here are displayed the measured magnetic properties values and the time since the start of the experiment.

12 – The graph of the BH loop derived from the most recently acquired data.

13 – The graphs of permeability and the power loss for tested points.

14 – The acquired waveforms are shown in these two graphs.

15 – The graph shows the harmonics in the search coil induced voltage

During a typical measurement, the program can be stopped at anytime with the STOP button. Any measured points will be saved if selected. The application will automatically stop if an error occurs or if all the points from the flux density table are successfully measured. The input voltages and the harmonic distortion of the output signal are monitored throughout the measurement, and if above the limit, will cause the program to stop.

3.4. Triggering

An essential part of the developed system is the triggering of the signals acquisition. It is necessary for the operation of the periodic averaging technique and the digital feedback. The acquisition is set to acquire a lump of data, the duration of one period, at a time. These lumps of data, consecutive cycles, must be in phase and this is facilitated by triggered acquisition. The triggering further allows the measured and generated signals to be phase–locked to allow correct operation of the digital feedback.

Further information on the mechanism of the acquisition is provided in section 3.3.3.

3.4.1 Types of triggering

Triggering in general can be accomplished by software data processing or by hardware functionality. Due to the fact that a low level signals with a substantial amount of noise are the subject of the measurement, it was desirable to use the latter solution. Software triggering was anticipated to malfunction in these conditions.

There are two types of the hardware triggering [3.26]:

- analogue
- digital

In the analogue triggering, the DSA monitors continuously an analogue signal to determine if it satisfies the trigger conditions, i.e. the signal crosses a predefined level on a specified slope. Once the trigger conditions are met, the analogue trigger circuitry (ATC) generates an internal trigger signal to initiate the acquisition. Figure 3.20 shows the rising slope of a sinusoidal signal triggered at level zero and on a rising edge, meaning that the acquisition starts precisely with the first sample that is higher than the previous sample and zero.

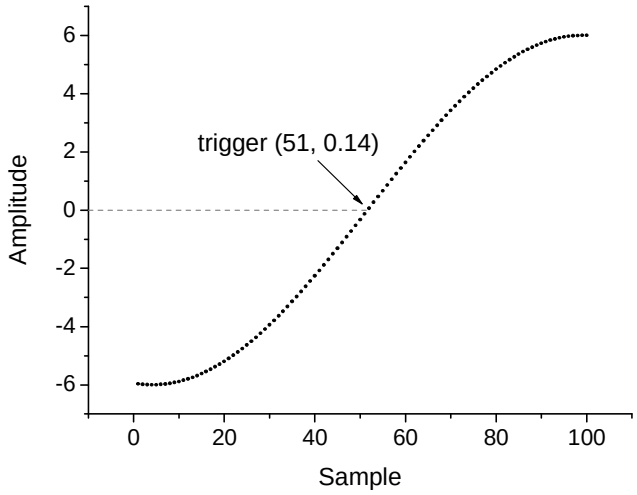

Figure 3.20 Illustration of the analogue triggering on a positive zero crossing

The precision of this type of triggering is limited by the sensitivity and speed of the equipment. An example of the former is shown in Figure 3.21a, where the same waveform (Figure 3.20) is sensed by a low sensitivity ADC (2 V). The trigger activates six samples later in this case. The negative impact that a low sampling frequency may have on the triggering is shown in Figure 3.21b (sampling frequency is 10 times smaller).

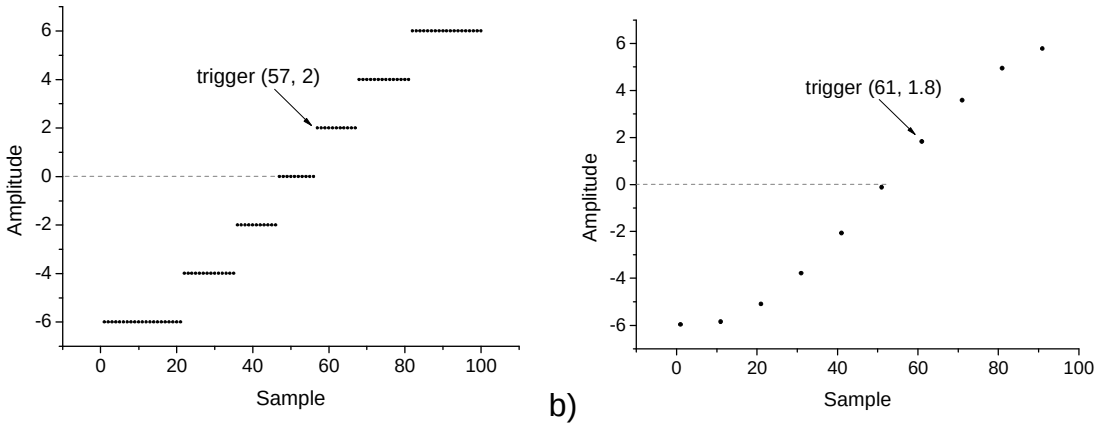

Figure 3.21 Illustration of triggering impaired by: a) low sensitivity of a DAQ, b) insufficient sampling frequency

The digital triggering uses a digital signal or a combination of signals as a stimulus. These can be either external (e.g. from other equipment) or internal (e.g. a counter). Conversely to the analogue triggering, the digital triggering is not affected by the sensitivity or the sampling frequency of the acquisition and is more accurate. The DSA 4461 processes the digital trigger input with a

100 MHz clock, whereas the maximum sampling frequency of analogue channels is 204.8 kHz.

3.4.2 Provision of the triggering waveform

Since the DSA 4461 does not have counters or digital outputs, the triggering waveform had to be generated on the analogue output. This signal was then looped back to the card through the digital input, PFI0. The triggering signal is being generated simultaneously to the magnetising waveform and hence the phase shift between them remains constant between modifications to the magnetising signal.

The triggering waveform was configured initially according to the DSA data sheet, to be a square waveform of 5 V amplitude and 50% duty cycle. However, every now and then, a 180 degrees phase shift of the measured signal was observed. To investigate the issue, the magnetising signal was looped back to an analogue input for evaluation. A test application (trigger_test.vi) was created that generates continuously a sine waveform of high amplitude (1 V) so that it is not compromised by a noise and can be measured precisely. A software trigger function is used to determine the index of the first sample in an array ≥0. If the digital triggering functions correctly, the software trigger is expected to return the same sample index after every signal acquisition. Otherwise, the trigger index is recorded and the 'bad triggers' indicator (a counter of the incorrectly triggered acquisitions) updated (Figure 3.22). This way it was confirmed that the triggering does malfunction and occasionally takes place on the falling edge of the square waveform. A measurement of the triggering waveform by means of a high sampling rate oscilloscope revealed many harmonics in the signal causing so called 'ringing', alike the one shown in Figure 3.23. It was established that this behaviour is expected from the DSA 4461 and any other DSA instrument as a result of the internal architecture [3.27].

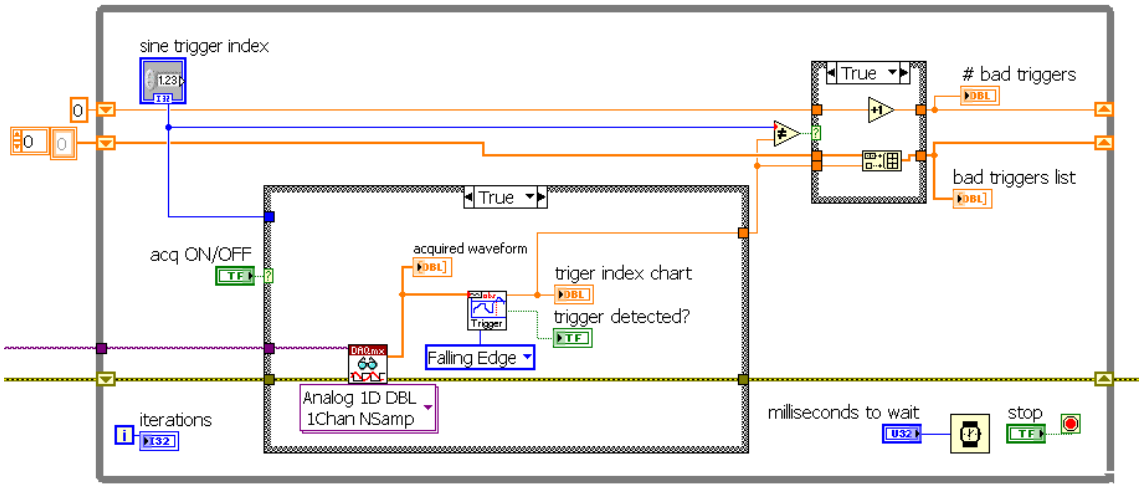

Figure 3.22 Triggering test VI block diagram depicting the acquisition and analysis section

The developed trigger testing VI was subsequently used to test various waveforms that would perform correctly as a trigger. It was found experimentally that the trigger signal had to be a short impulse in order to prevent triggering acquisition circuitry on the falling edge. Eventually, by trial and error, the suitable waveform parameters were found to be as those shown in Figure 3.24.

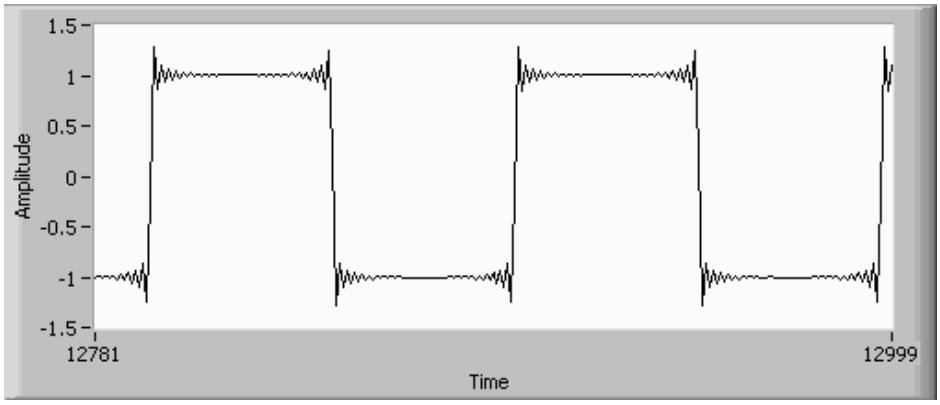

Figure 3.23 An example of a square wave generated by DSA 4461 illustrating the incapability of the analogue output to produce sharp edge waveforms [3.27]

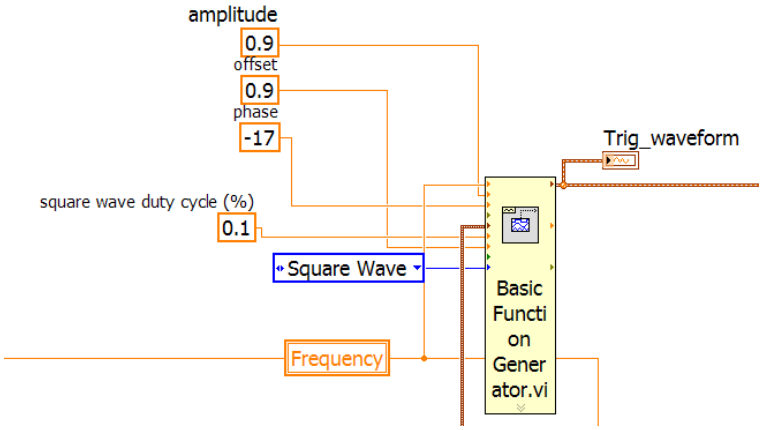

Figure 3.24 Triggering waveform setup

3.5. Digital compensation

The principle of a magnetic flux density measurement by means of a search coil was explained in section 2.4. Figure 3.4, in section 3.2.3, shows the former on which the coil was wound. The use of the former introduces an error to the magnetic measurement due to the coil encompassing not only the sample (as in (Figure 2.12), but also an air gap between the sample and the former, and the former itself. Since the last one is a non–magnetic material, its permeability can be assumed to be equal to that of free space. Therefore the voltage induced in the search coil can be calculated as:

$$V_{EMF}(t) = N\,\frac{d\Phi_{sample}(t) + d\Phi_{gap}(t)}{dt} = V_{sample}(t) + V_{gap}(t) \qquad (3.10)$$

$V_{EMF}(t)$ – voltage induced in the search coil

N – number of turns in the search coil

Φ_{sample} – flux changing in time within the sample

Φ_{gap} – flux within the gap between the sample and the coil

$V_{sample}(t)$ – voltage resulting from the flux in the sample

$V_{gap}(t)$ – voltage resulting from the flux in air

Hence the actual measured magnetic induction value is:

$$B = \frac{1}{NA_{sample}} \int [V_{sample}(t) + V_{gap}(t)]\,dt = B_{sample}(t) + B_{gap}(t)\,\frac{A_{sample}}{A_{gap}} \qquad (3.11)$$

A_{sample} – cross-sectional area of the sample

$B_{sample}(t)$ – magnetic flux density in the sample

$B_{gap}(t)$ – magnetic flux density in the gap between the sample and the coil

A_{gap} – cross-sectional area of the gap between the sample and the coil

In order to compensate for the magnetic flux density in the gap between the sample and the coil, its value can be found as:

$$B_{gap}(t) = \mu_0 H(t) \tag{3.12}$$

Following the directives of Epstein [3.23] and SST [3.3] test standards, the air flux compensation must be applied to the voltage signal induced in the search coil and not the magnetic flux density derived from it. This is important for a proper evaluation of the coil signal form factor. The required value can be calculated as:

$$V_{gap}(t) = NA_{gap}\ \mu_0 \frac{dH(t)}{dt} \tag{3.13}$$

In order to avoid the error associated with the non-uniformity of the coil, a different approach was developed to facilitate the air flux compensation. The sample is removed from the SST and the recorded signals of magnetising field current and search coil induced voltage are plotted as shown in Figure 3.25. The slope of the line is the compensation coefficient, and hence the voltage induced in the search coil due to the magnetic flux in the gap can be found as:

$$\int V_{gap}(t)dt = C\ I_{shunt}(t) \ \Rightarrow\ V_{gap}(t) = \frac{dV_{shunt}(t)}{dt}\frac{C}{R_{shunt}} \tag{3.14}$$

As a result the magnetic flux density calculated from the compensated coil induced voltage is the actual magnetic flux density in a sample:

$$B_{sample}(t) = \frac{1}{NA_{sample}}\int\left[V_{EMF}(t) - \frac{dV_{shunt}(t)}{dt}\frac{C}{R_{shunt}}\right]dt \tag{3.15}$$

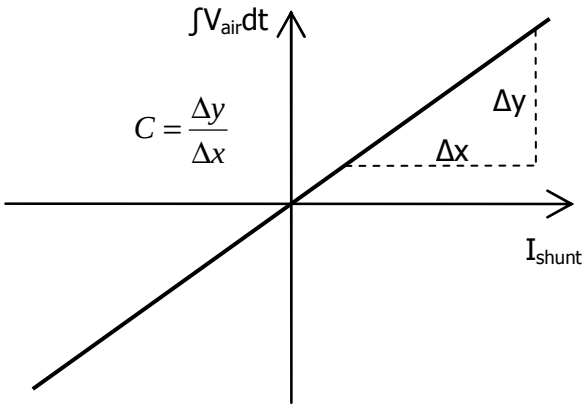

Figure 3.25 Illustration of the compensation coefficient "C", i.e. slope of the curve

3.6. Measurement results

Magnetic properties, the permeability and power loss, of the Epstein size samples and toroids were measured in two stages. The measurement setup shown in Figure 3.5 was used to obtain the magnetic data at high flux densities and the low-noise setup, described in section 3.2.5, was used in low flux density measurements. The measurements were performed with the control application (tk.VI) in the following manner:

- The sample was demagnetised in the process described in section 3.3.8;
- The appropriate information on the samples (details in section 3.3.10) were inputted in the controls group two and four, in Figure 3.19;
- The criteria of the peak flux density error (controls in group eight, Figure 3.19), was set to 0.2 in low-flux density measurements;
- The tk.VI was executed to perform the measurement.

All measurements were repeated once to confirm the obtained data is within expected repeatability range.

3.6.1 Measurements by means of an SST

Magnetic properties of the Epstein size strips of electrical steel, 0.3 mm thick, were measured to demonstrate the capability of the developed low flux density system. Three samples of the CGO and HGO steel of unknown grade were tested; the obtained permeability and power loss data are shown in Figure 3.26 to Figure 3.29.

It can be seen in Figure 3.27 that the permeability of HGO steel is higher than that of the CGO material, as expected. However, Figure 3.26 shows that this reverses around 10 mT, and the initial (constant) permeability of HGO steel is about half of that of the CGO samples. No information of this effect was found in the literature. Similar inconsistency appears in the plots of the power loss. As anticipated, in Figure 3.29 the measured power loss of HGO samples is lower than that of the CGO. On the contrary, below about 30 mT the data in Figure 3.28 show the power loss of the CGO samples to be lower than those of HGO.

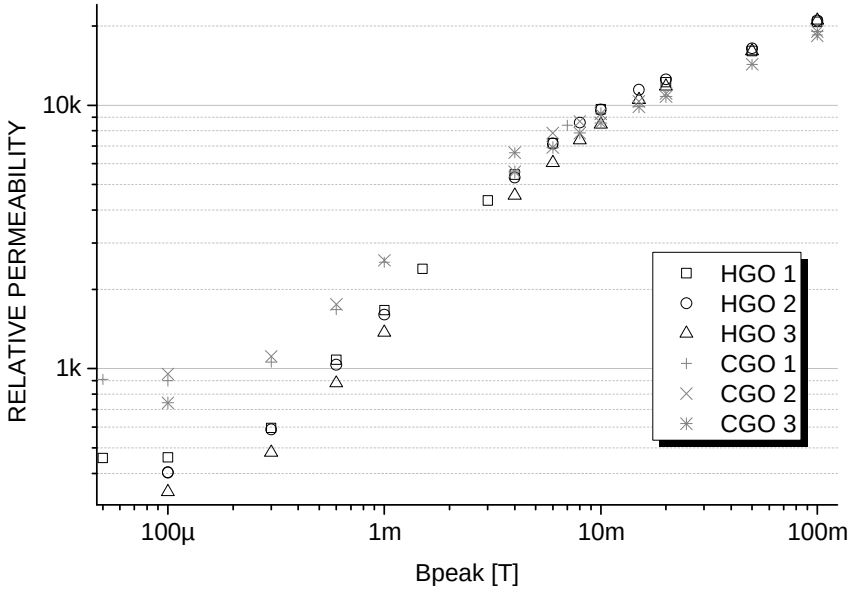

Figure 3.26 Permeability vs peak flux density characteristics in the range from 50 uT to 100 mT for the CGO and HGO steel, 0.3 mm thick, Epstein samples

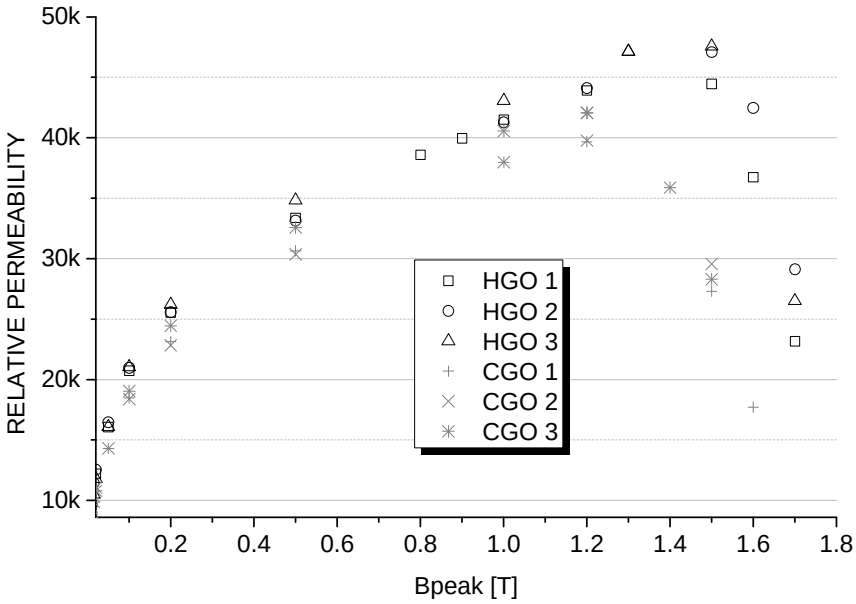

Figure 3.27 Permeability vs peak flux density characteristics in the range from 100 mT to 1.7 T for the CGO and HGO steel, 0.3 mm thick, Epstein samples

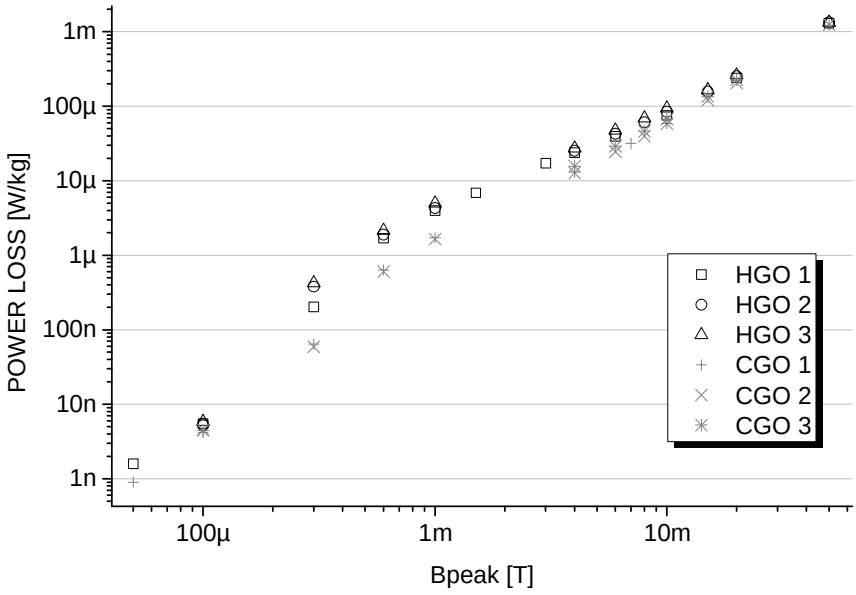

Figure 3.28 Specific total power loss vs peak flux density characteristics in the range from 50 uT to 100 mT for the CGO and HGO steel, 0.3 mm thick, Epstein samples

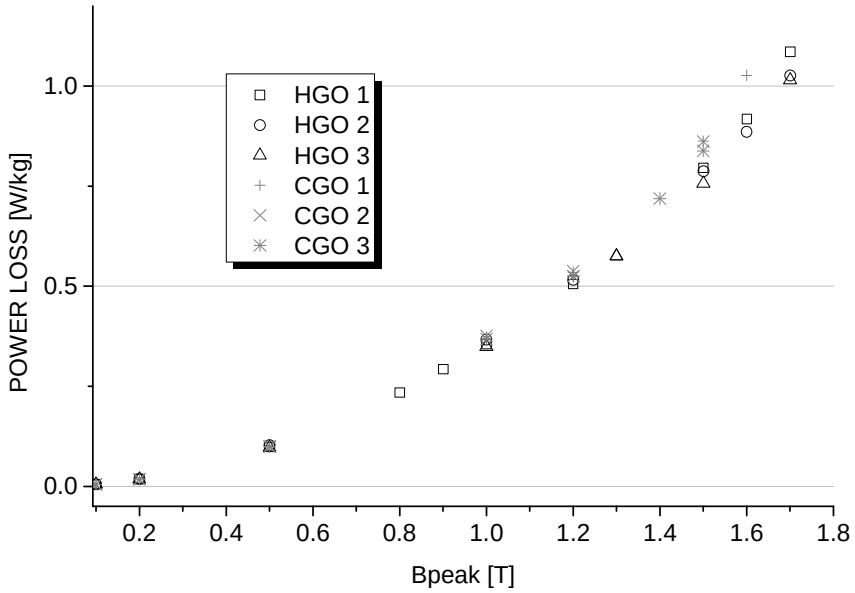

Figure 3.29 Specific total power loss vs peak flux density characteristics in the range from 100 mT to 1.7 T for the CGO and HGO steel, 0.3 mm thick, Epstein samples

3.6.2 CT core samples

Two CT 250/5 cores of undisclosed grade were measured in order to calculate the CT errors with the developed model (described in Chapter 4) and compare against the measured CT errors (see section 5.2). Search coils of 18 turns were wound on top of the existing CT secondary windings that were utilised as H coils. As both of the CT cores were manufactured to the same specification, the magnetic characteristics were found to be in close agreement, as shown in Figure 3.30 and Figure 3.31. The initial permeability is about 200, the power loss is proportional to the magnetisation up to 100 μT. Above that flux density, the magnetisation processes inside the core change (as described in section 2.3) and the hysteresis loss is thought to cause a rapid increase in the power loss (up to 300 μT). The permeability rises to the maximum value of 50,000 in the knee region, near 1.3 T. Eventually, change in the magnetisation process from the domain wall motion to domain rotation causes a sharp fall in permeability.

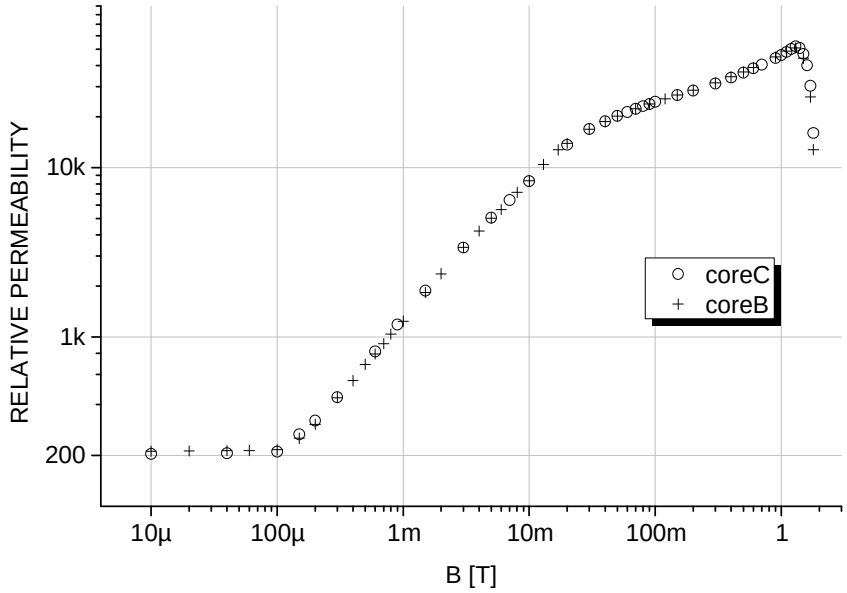

Figure 3.30 Permeability vs flux density characteristics for CT 250/5 cores 'B' and 'C'

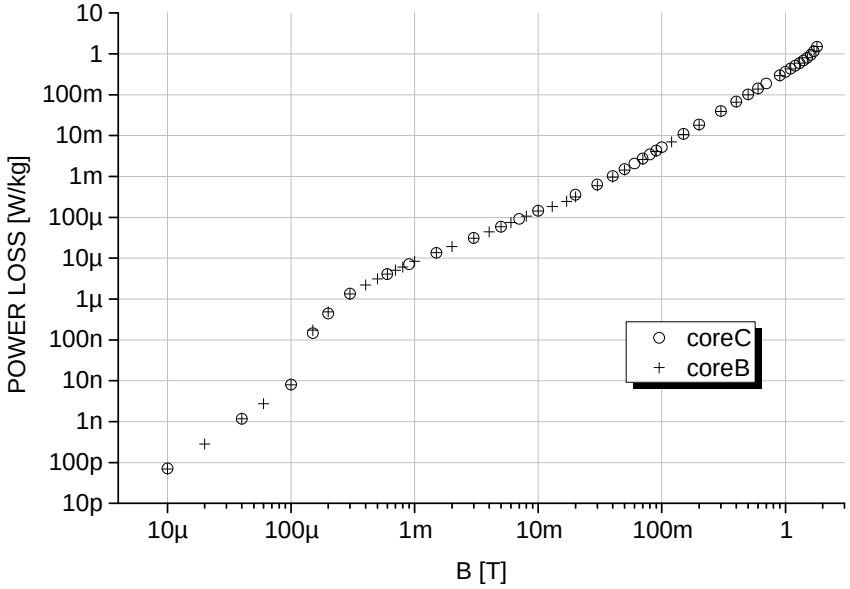

Figure 3.31 Specific total power loss vs peak flux density characteristics for CT 250/5 cores 'B' and 'C'

3.6.3 Vacuumschmelze toroidal samples

Although the developed measurement system was designed mainly for investigation of electrical steels, it was desirable to be able to conduct measurements on other ferromagnetic materials that are used in similar applications. A number of different samples was obtained from Vacuumschmelze and measured in a wide range of flux densities. Figure 3.26 and Figure 3.27 show the permeability and power loss of the following samples:

- W850 coated toroid, Vitroperm 800F (Fe-based nanocrystalline), A=14.9 mm^2, l= 104 mm, m=11.3 g;
- Vacoperm 100, 77% NiFe, uncoated toroid, A=54.2 mm^2, l=232 mm, m=109 g;
- Permax M, 56% NiFe, uncoated toroid, A=47.4 mm^2, l=218.3 mm, m=85.4 g;
- W955 uncoated toroid, Vitroperm (Fe-based nanocrystalline), A=21.1 mm^2, l=139 mm, m=21.8 g.

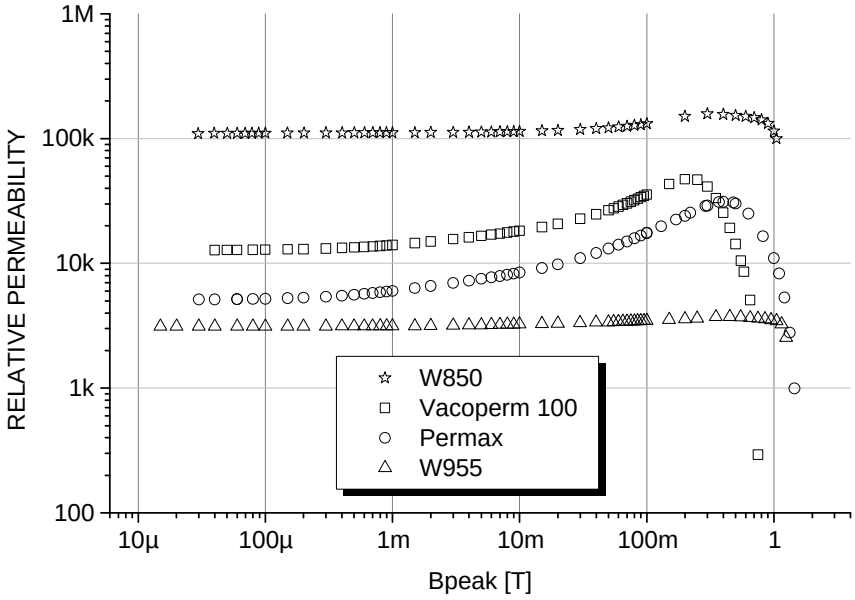

Figure 3.32 Permeability vs peak flux density characteristics for toroidal samples of nickel and nanocrystalline alloys

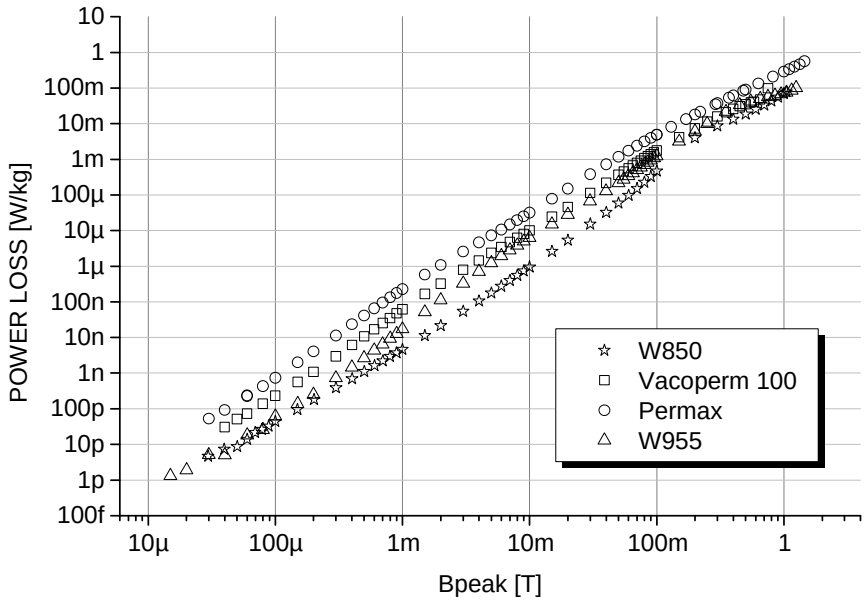

Figure 3.33 Total specific power loss vs peak flux density characteristics for the toroidal samples of nickel and nanocrystalline alloys

In Figure 3.34 and Figure 3.35 are shown the measured magnetic properties of the following samples:

- W639 uncoated toroid, Vitrovac 6150F (Co-based amorphous), A=13.8 mm^2, l=61.7 mm, m=6.74 g;
- W588 uncoated toroid, Vitrovac 6150F, A=13 mm^2, l=70.7 mm, m=7.28 g;
- Vitrovac 6150F uncoated toroid, A=14.1 mm^2, l=70.7 mm, m=7.3 g

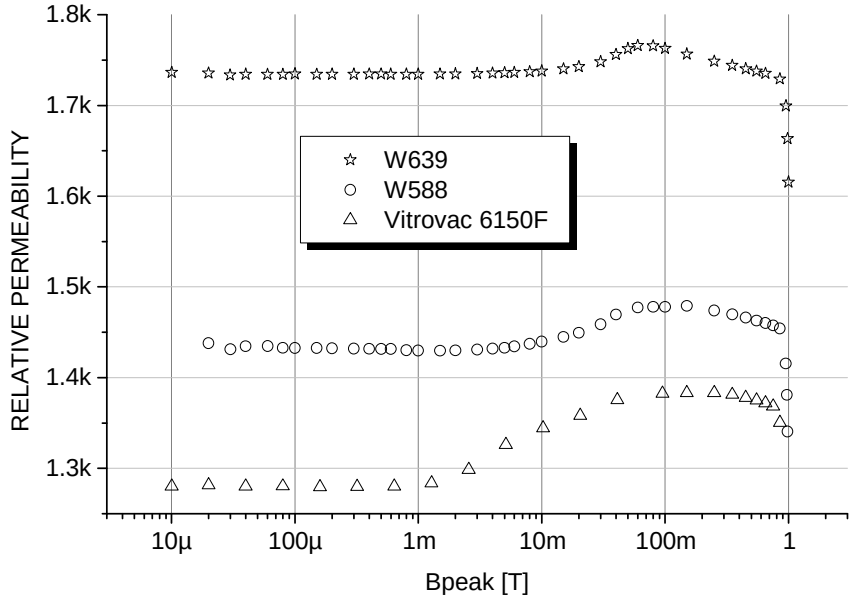

Figure 3.34 Permeability vs peak flux density characteristics for the toroidal samples of nickel and amorphous alloys

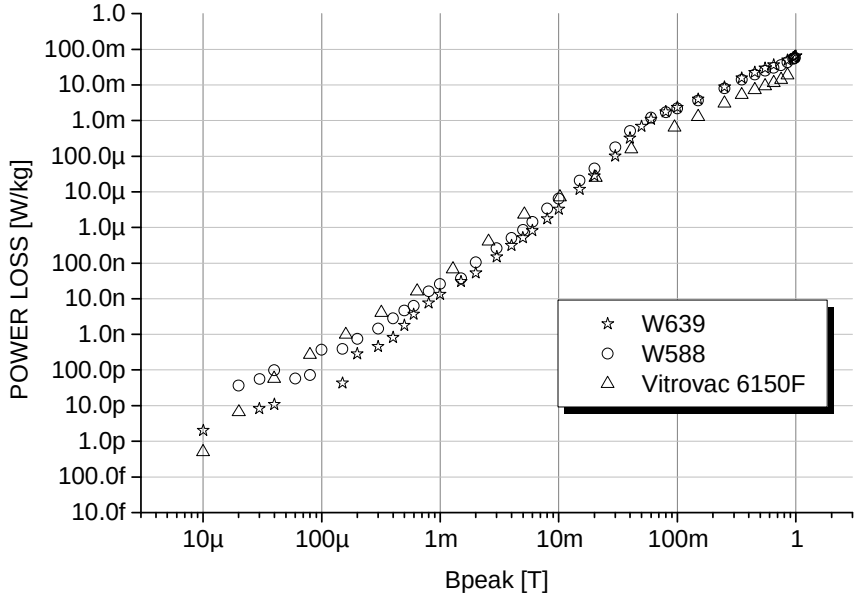

Figure 3.35 Total specific power loss vs peak flux density characteristics for the toroidal samples of nickel and amorphous alloys

3.7. Uncertainty of the low flux density system

The uncertainties of the permeability and power loss measurement were estimated according to [3.28]. Contributions of the systematic ("Type B" analysis) and random errors ("Type A" analysis) are combined in the

uncertainty budget as shown in Table 3.1. The first step was to calculate the uncertainty of Bpeak measurement (Table 3.1) for a particular peak flux density value.

Table 3.1 Uncertainty of the Bpeak measurement

Source of uncertainty	± %	Probability distribution	Divisor	Ci	Ui ± %	Vi or Veff
EMFpeak	0.347	Normal	2.00	1	0.17333	∞
Mass (Balance calibration)	0.010	Normal	2.00	1	0.00500	∞
Length (Ruler calibration)	0.025	Normal	2.00	1	0.01250	∞
Length (Reading uncert of rule)	0.082	Rectangular	1.73	1	0.04732	∞
Freq accuracy	0.002	Normal	2.00	1	0.00100	∞
Criteria	0.200	Rectangular	1.73	1	0.11547	∞
Sum of squares					0.04580	
Combined uncertainty					0.21401	
Expanded uncertainty					0.5	
at a confidence level of 95 %						

The uncertainty of the DSA itself (first row) was found to maximum 0.347 in the following way:

Table 3.2 Calculation of the max uncertainty of the DSA card from the specification [3.14]

Device Input Amplitude Accuracy			
range	uncertainty [±mV]	uncertainty [±%]	Calibrator Output Amplitude (VDC)
0.316	31.1	0.345555556	9
1	31.1	0.345555556	9
3.16	31.1	0.345555556	9
10	10.4	0.346666667	3
31.6	3.1	0.344444444	0.9
42.4	1	0.333333333	0.3
	max=	0.346666667	

The reading uncertainty of the ruler is the percentage ratio of the value of the minimum notch to the length of the Epstein strip. The accuracy of the DSA clock can be found in the specification. Criteria stands for the desired accuracy of the Bpeak setting during the measurement. The probability type can be found in calibration certificate or otherwise must be presumed according to rules gives in the [3.28]. The divisor is probability dependant, and coefficient is describing how sensitive the considered uncertainty is to the error in elementary uncertainties, in this case the coefficient of one was decided appropriate. Following the formulas of the budget the expanded uncertainty can be determined.

Following the same scheme, the uncertainty in Hpeak was determined, as shown in Table 3.3. The standard uncertainty of Rshunt was calculated as standard deviation of ten measurements divided by square root of samples number. The uncertainty of temperature change of the current shunt was calculated in section 3.2.4. Dependence on Bpeak value is the uncertainty found previously for the Bpeak. Repeatability describes how much Hpeak varied in consecutive measurements of at the same Bpeak.

Table 3.3 Determination of the uncertainty in Hpeak for Bpeak=0.5T

Source of uncertainty	± %	Probability distribution	Divisor	Ci	Ui ± %	Vi or Veff
EMFpeak	0.347	Normal	2.0000	1	0.17333	∞
freq	0.002	Normal	2.0000	1	0.00100	∞
Rshunt measurement	0.009	Normal	2.0000	1	0.00461	∞
Shunt temp change	0.450	Normal	2.0000	1	0.22500	∞
Length magn path (Rule calibration)	0.025	Normal	2.0000	1	0.01250	∞
Length (Reading uncert of rule)	0.082	Rectangular	1.7321	1	0.04732	∞
Dependence on B value	0.500	Rectangular	1.7321	1	0.28868	∞
Repeatability	0.3	Rectangular	1.7321	1	0.17321	∞
Sum of squares					0.19642	
Combined uncertainty					0.44319	
at a confidence level of 95 %						

The two uncertainties calculated above allowed calculation of uncertainty of the permeability, as shown in Table 3.4.

Table 3.4 Uncertainty in in permeability vs B at Bpeak=0.5T

Source of uncertainty	± %	**Probability**	**Divisor**	**Ci**	**Ui**	Vi or Veff
		distribution			**± %**	
Bpeak uncertainty	0.2	Normal	2.0000	0.01	0.00107	∞
Hpeak uncertainty	0.4	Normal	2.0000	1	0.22160	∞
Repeatability	0.4	Rectangular	1.7321	1	0.23094	∞
Sum of squares					0.10244	
Combined uncertainty					0.32006	
Expanded uncertainty					0.7	
at a confidence level of 95 %						

Following the same algorithm uncertainty for power loss was calculated. Both were repeated for a number of flux densities within 10 μT and 1.8 T. It was

found that repeatability of measurements with the low flux system were the major factor affecting the uncertainty. It was decided to simplify the matters considerably and unify the uncertainty across the whole flux density range as much as possible.

The uncertainty of the permeability was estimated to be ±8% up to the peak flux density of 50 mT and ±3% above that value. It may be worth noting that the uncertainty within the range of 0.1 T and 1 T was found to be ±1% but to simplify matters and include the high flux density region where the permeability drops sharply, it was decided to adopt the ±3% value.

The uncertainty of the power loss was found to be higher, potentially due to higher sensitivity of this property to Bpk and thus affecting the repeatability more. The adopted values are ±13% below 50 mT and ±5% above.

References

[3.1] A. J. Moses, Challenges in High and Low Field AC Magnetic Measurements for Material Modelling and Electrical Machine Performance Prediction, IET Seminar, pp. 15–20, 2006

[3.2] S. Zurek, F. Al–Naemi, A. J. Moses, Anomalous B–H Behaviour of Grain–oriented Electrical Steels at Very Low Flux Density, Journal of Magnetism and Magnetic Materials, Vol. 320, pp. 2521–2525, 2008

[3.3] Magnetic Materials — Methods of Measurement of the Magnetic Properties of Electrical Sheet and Strip by Means of a Single Sheet Tester, European Standard, EN 10280:2001

[3.4] F. Fiorillo, Characterization and Measurement of Magnetic Materials, Elsevier Academic Press, Amsterdam, London, 2004

[3.5] NI 6115/6120 Specifications, National Instruments

[3.6] S. Zurek, T. Kutrowski, A. J. Moses, P. I. Anderson, Measurements at Very Low Flux Density and Power Frequencies, Journal of Electrical Engineering, Vol. 59, No. 7/S, pp. 7–10, 2008

[3.7] A. Ambardar, Analog and digital signal processing, PWS Pub, Boston, c1995

[3.8] Analog Sampling Basics, White Paper, National Instruments, 2013

[3.9] Low Level Measurements Handbook, Keithley Instruments, 2004

[3.10] Simultaneous Sampling DAQ Architectures, Tutorial, National Instruments, 2010

[3.11] NI PXI Chassis Design Advantages, Tutorial, National Instruments, 2010

[3.12] Signal Conditioning Fundamentals for Computer–Based Data Acquisition Systems, Tutorial, National Instruments, 2009

[3.13] Increase Your Measurement Accuracy by 10X with Signal Conditioning, Tutorial, National Instruments, 2009

[3.14] NI 446x Data Sheet, National Instruments

[3.15] S. Zurek, Two-dimensional magnetisation problems in electrical steels, PhD thesis, Cardiff University, 2005

[3.16] Crown Macro–Tech MA–5002VZ Operational Manual

[3.17] Preventing and Attacking Measurement Noise Problems, White Paper, Campbell Scientific, 2001

[3.18] Field Wiring and Noise Considerations for Analog Signals, Tutorial, National Instruments, 2008

[3.19] Pseudo–differential versus Differential Input Configurations, Tutorial, National Instruments, 2008

[3.20] V. Gorican, B. Hribernik, A. Hamler, T. Nakata, The Measurement of Power Losses at High Magnetic Field Densities or at Small Cross–Section

of Test Specimen Using the Averaging, Journal of Magnetism and Magnetic Materials, Vol. 215–216, 2000

[3.21] K. Matsubara, T. Nakata, N. Takahashi, K. Fujiwara, M. Nakano, H.L. Zhu, H. Aoki, Effect of Staircase Output Voltage Waveform of a D/A Converter on Iron Losses Measured Using an H Coil, Journal of Magnetism and Magnetic Materials, Vol. 160, pp. 185–186, 1996

[3.22] S. W. Smith, Digital Signal Processing: A Practical Guide for Engineers and Scientists, Newnes, 2002

[3.23] Magnetic Materials — Part 2: Methods of Measurement of the Magnetic Properties of Electrical Steel Sheet and Strip by Means of an Epstein Frame, International Standard, IEC 404–2:1996

[3.24] TDMS File Format Internal Structure, Tutorial, National Instruments, 2010

[3.25] Calculation of the Effective Parameters of Magnetic Piece Parts, International Standard, IEC 60205:2006

[3.26] Tips and Techniques in Data Acquisition Triggering – NI–DAQmx, Tutorial, National Instruments, 2009

[3.27] Why Does my Dynamic Signal Acquisition (DSA) Device Not Handle Impulses, Square Waves, Triangle Waves or Sawtooth Waves Well? KnowledgeBase, National Instruments

[3.28] The Expression of Uncertainty and Confidence in Measurement, UKAS publication M3003, 2007

Chapter 4

Modelling of a current transformer

A model relating the magnetic properties of a CT core to the errors of the CT itself is presented in this work. The model is simple in its formulation and can be easily implemented in the CT design. It does not involve modelling of the core hysteresis, as is the case with the complex models, by Locci and Muscas [4.1] or Annakkage et al. [4.2], and Rezaei–Zare et al. [4.3], commonly employed in transient state studies of the protective CTs. Proposed here is a solution which follows the same principles as those found in the work of Draxler and Styblikova [4.4]. However, this model links directly the CT errors to the main magnetic properties of the material. In this way, the accuracy of a potential CT design can be easily predicted from the basic magnetic data of the core material.

The developed CT model follows the assumption of sinusoidal currents. This is justified practically, because the CT errors are measured industrially by injecting sinusoidal currents [4.5]. In the international standard [4.6], the phase error also refers to primary and secondary currents as sinusoidal. Although ferromagnetic materials exhibit nonlinear behaviour, it has a fractional effect on the secondary current of a CT that meets the requirements of the standard and is operated within its specification [4.7]. Under most test conditions, the uncertainties from the waveform distortion are commonly regarded as negligible [4.8].

The basic principle utilized in the CT analysis is the duality between the magnetic and the electrical circuits [4.9]. This allowed the physical behaviour of a CT at a steady state to be represented by a network of electrical elements which could be studied easily. A negligible leakage reactance design CT is considered in this work, which is the most often used CT on the distribution network. The analysis of a different design CT, with significant leakage reactance, e.g. a core with an air gap(s), windings encompassing a limited

circumference of the core, must be based on an equivalent circuit diagram including the relevant components, described in section 4.1.

4.1. The equivalent circuit of a current transformer

The principle of the equivalent circuit diagram has been introduced in section 2.5. Here the general case of the circuit will be adapted to the CT case in order to simplify the analysis. The equivalent circuit of a transformer shown in Figure 2.14 can be reduced, as shown in Figure 4.1. Since it is not the voltage but the current that is supplied to a CT, the voltage drop on the primary winding components $\mathbf{R_P}$ and $\mathbf{X_P}$ does not affect the currents in the circuit. Therefore, these elements are irrelevant and are omitted in further analysis. The voltage source, $\mathbf{V_P}$ is swapped for the current, representing the actual primary current $\mathbf{I_P}$ to be measured. A negligible leakage flux design of a CT is considered in this work, i.e. having a continuous core and uniformly distributed windings; therefore the secondary leakage reactance is also removed [4.6], [4.7]. In the case of CTs with a considerable leakage flux, this parameter would have to be included in the model and its value either measured or estimated. To improve further the model, the secondary winding DC resistance $\mathbf{R_{aS}}$ may require adjustment if a considerable rise of temperature is expected at high currents.

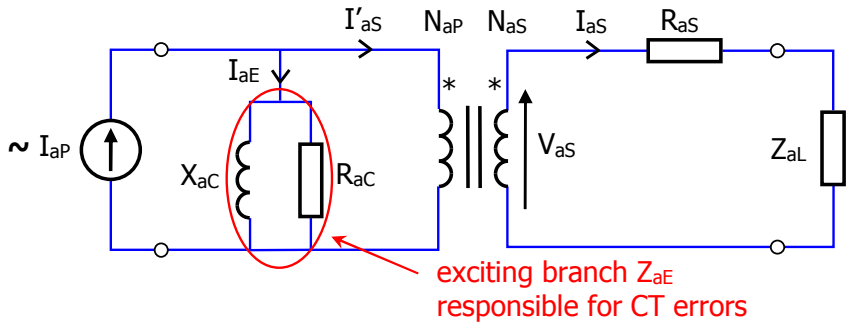

Figure 4.1 The simplified equivalent circuit diagram of a transformer suitable for CT analysis. All parameters were given index "a" to differentiate between diagrams.

On the basis of an equivalent circuit diagram, a phasor (vector) diagram can be constructed. This type of a diagram is used to visualize complex circuits and

help with their analysis [4.10]. It is clear from the CT phasor diagram shown in Figure 4.2, that the amplitude error of that CT equals the difference in length of the two green vectors. The phase error, also known as a phase displacement, is the angle **PD** between these vectors. The black vectors depict the voltages in the secondary side of the CT equivalent circuit, and the currents flowing through the exciting branch elements. The red vector illustrates the $\mathbf{I_E}$, exciting current, of which the length and phase shift has direct influence on both CT errors.

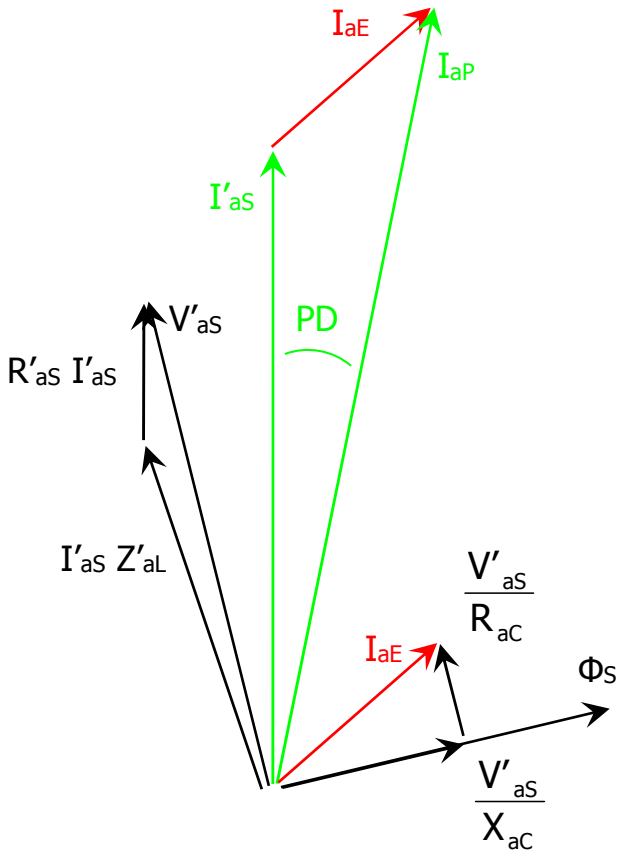

Figure 4.2 The phasor diagram of the CT. Parameters transferred to the primary side of the CT are marked with an apostrophe.

It is evident from the phasor diagram and the CT equivalent circuit diagram that inaccuracy of CTs is caused by the $\mathbf{I_{aE}}$ portion of the primary current flowing through the exciting branch instead. The higher the exciting impedance, the lower the current $\mathbf{I_{aE}}$, and consequently, the smaller are the CT errors. The value of the reactive part of this impedance is proportional to the CT core permeability which determines how much current is necessary to maintain

a flux in a CT core. This is why materials of a high magnetic permeability are sought for the production of CTs. Another important magnetic parameter of a CT core is its magnetic loss, of which a low value is desired to keep the resistive component of the exciting impedance high. The variability of the magnetic properties with a peak value of flux density implies that the equivalent value of the exciting impedance will also vary. Therefore the calculation of the CT errors at a particular current is based on the value of the exciting impedance at a corresponding flux density.

4.2. The relationship between magnetic properties and the exciting impedance

It will be shown here that the exciting impedance can be calculated from the permeability and the power loss. For that purpose an equivalent circuit diagram of the measurement setup has to be constructed, the same way the CT equivalent circuit was developed for the CT analysis. The equivalent circuit diagram of a transformer in Figure 2.14 is the starting point. The voltage source is replaced by the current source ($\mathbf{I_{bP}}$ in Figure 4.3) that drives a current through the primary winding to create the desired magnetic field. The primary side components that would now be connected in series with the current source are omitted, as they have no effect on the value of the current and hence the magnetic field. As during the measurement of the magnetic properties, the secondary circuit remains open, i.e. the load impedance is much greater than that of the secondary side components, the secondary reactance $\mathbf{X_S}$ and resistance $\mathbf{R_S}$ have negligible effect on the voltage induced in the secondary winding that is being measured ($\mathbf{V_{bS}}$ in Figure 4.3), the secondary side components are skipped. Therefore, it is the exciting branch and an ideal transformer that form the equivalent circuit diagram of the measurement setup described in Chapter 3, as shown in Figure 4.3.

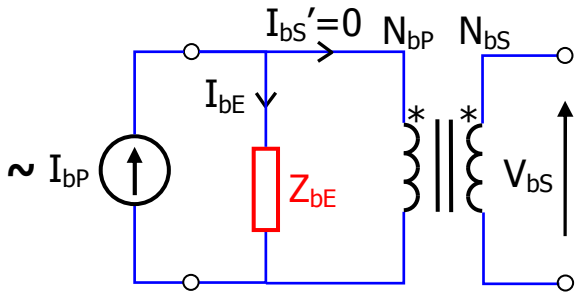

Figure 4.3 The equivalent circuit diagram of the measurement setup. All parameters were given index "b" to differentiate between diagrams.

Two parameters of the measurement setup equivalent circuit are monitored during the magnetic test, the primary current $\mathbf{I_{bP}}$ and the secondary voltage $\mathbf{V_{bS}}$, which allow the calculation of the BH characteristics (magnetisation curve) and hence the permeability and power loss. Bearing in mind that the secondary circuit is open, i.e. exciting current is synonymous with that of the primary ($\mathbf{I_{bP}} = \mathbf{I_{bE}}$); exciting impedance can be computed using complex numbers calculus as follows:

$$\underline{Z_{bE}} = \frac{\underline{V_{bS}} \cdot \frac{N_{bP}}{N_{bS}}}{\underline{I_{bE}}} \tag{4.1}$$

where:

$$\underline{V_{bS}} = N_{bS} A_b \cdot \frac{d\underline{B}}{dt} \tag{4.2}$$

$$\underline{I_{bP}} = I_{bE} = \underline{H} \cdot \frac{l_b}{N_{bP}} \tag{4.3}$$

l_b – magnetic path length of a sample

A_b – cross–sectional area of a sample

$\underline{B}$ – complex value of the flux density in a sample

$\underline{H}$ – complex value of the magnetic field strength applied to a sample

N_{bP}, N_{bS} – number of turns in primary and secondary windings, respectively

As previously stated, the signals in the equivalent circuit are sinusoidal, hence:

$$\underline{B} = \hat{B} \cdot e^{j\omega t} \tag{4.4}$$

$$\underline{H} = \hat{H} \cdot e^{j(\omega t + \varphi)} \tag{4.5}$$

ω – angular frequency

Substituting equations (4.4) into (4.2), (4.5) into (4.3), the resulting equations into (4.1) yields:

$$\underline{Z_{bE}} = \frac{A_b}{l_b} \cdot {N_{bP}}^2 \cdot \omega \cdot \mu \cdot e^{\,j(\pi/2-\varphi)} \tag{4.6}$$

μ – permeability of the core

φ – ∠(B, H)

Solving the equation for the power loss, being the area of a BH loop, with the same assumption of a flux density and a magnetic field being sinusoidal (as explained above), results in the following (for derivation of the formula see section 4.3):

$$P = \hat{B}^2 \cdot \omega \cdot \frac{\sin\varphi}{2\mu} \tag{4.7}$$

P – power loss value

From (4.7) the angle **φ** can be determined as:

$$\varphi = \arcsin\left(\frac{2 \cdot P \cdot \mu}{\hat{B}^2 \omega}\right) \tag{4.8}$$

It is shown in (4.6) and (4.8) that the exciting impedance is a function of, not only the sample's magnetic properties (permeability, power loss) at a particular peak flux density, but also the sample's dimensions and primary turns. For that reason it is essential that the values of those parameters corresponding to a CT core are used for calculating its exciting impedance:

$$\underline{Z_{aE}} = \frac{A_a}{l_a} \cdot {N_{aP}}^2 \cdot \omega \cdot \mu \cdot e^{\,j(\pi/2-\varphi)} \tag{4.9}$$

Since a CT core was used as the sample in the magnetic properties test, only the number of turns $\mathbf{N_{bP}}$ has to be replaced according to the actual specification of a CT, $\mathbf{N_{aP}}$.

4.3. The derivation of the power loss formula

As discussed previously, the flux density and the magnetic field are assumed to be sinusoidal. For the purpose of the power loss calculation, it is convenient to express them in the form below:

$$H = \hat{H}\sin(\omega t + \varphi) \tag{4.10}$$

$$B = \hat{B}\sin(\omega t) \quad \Rightarrow \quad dB/dt = \omega \hat{B}\cos(\omega t) \tag{4.11}$$

Substituting H and dB in the power loss equation with the above expressions results in:

$$P = \frac{1}{T}\int_0^T HdB = \frac{\hat{H}\hat{B}\omega}{T}\int_0^T [\sin(\omega t + \varphi)\cos(\omega t)]dt \tag{4.12}$$

Using the trigonometric identity given below:

$$\sin(a+b) = \sin(a)\cos(b) + \sin(b)\cos(a)\,, \tag{4.13}$$

power loss can be expressed as:

$$P = \frac{\hat{H}\hat{B}\omega}{T}\int_0^T [\sin(\omega t)\cos(\omega t)\cos(\varphi) + \cos^2(\omega t)\sin(\varphi)]dt \tag{4.14}$$

An integral of a sum equals a sum of elementary integrals, thus below the first part of the integral is analysed. For this another trigonometric identity is used:

$$\sin(2a) = 2\sin(a)\cos(a) \tag{4.15}$$

$$\int_0^T \frac{1}{2}\sin(2\omega t)\cos(\varphi)dt = \frac{1}{2}\left[-\frac{1}{2\omega}\cdot\cos(2\omega t)\cos(\varphi)\right]_0^T = 0 \tag{4.16}$$

In order to find the value of the second integral, the trigonometric identity shown below is utilised:

$$\cos(2a) = 2\cos^2(a) - 1 \tag{4.17}$$

$$\int_0^T \left[\frac{1}{2}\cos(2\omega t)\sin(\varphi)+\frac{1}{2}\sin(\varphi)\right]dt = \\ = \frac{\sin(\varphi)}{2}\left[\frac{1}{2\omega}\cdot\sin(2\omega t)+t\right]_0^T = \frac{\sin(\varphi)}{2}T \tag{4.18}$$

The value of the power loss is:

$$P = \frac{\hat{B}^2\omega}{2\mu}\cdot\sin\varphi \quad \Rightarrow \quad \varphi = \arcsin\frac{2P\mu}{\hat{B}^2\omega} \tag{4.19}$$

4.4. Algorithm of CT errors calculation

There are two CT errors defined in the international standard [4.6]. The phase displacement is a difference in phase between the vectors of the secondary and primary current:

$$PD = \varphi_S - \varphi_P \tag{4.20}$$

The amplitude error is a percentage difference of the RMS values of both currents of the primary current:

$$F\% = \frac{I_S\cdot\frac{N_S}{N_P} - I_P}{I_P}\cdot 100\% \tag{4.21}$$

The complex values of both currents, from which the corresponding phase shifts can be extracted and RMS values found, can be determined as follows:

$$\underline{I_{aS}} = \frac{\underline{V_{aS}}}{(\underline{Z_{aL}} + \underline{R_{aS}})} \tag{4.22}$$

where:
$$\underline{V_{aS}} = N_{aS}\cdot A_a\cdot\omega\cdot\hat{B}\cdot e^{j\omega t} \tag{4.23}$$

Z_{aL} – rated burden impedance of a CT

R_{aS} – DC resistance of the secondary winding

N_{aP}, N_{aS} – number of turns in primary and secondary windings of a CT, respectively

A_a – cross–sectional area of a CT core

$\hat{B}$ – peak flux density at which values of power loss and permeability are being considered

$$\underline{I_{aP}} = \underline{I_{aS}} \cdot \frac{N_{aS}}{N_{aP}} + \frac{\underline{V_{aS}} \cdot \frac{N_{aP}}{N_{aS}}}{\underline{Z_{aE}}} \tag{4.24}$$

Once both current values are calculated from (4.22) and (4.24) the corresponding phase shifts can be extracted and the RMS values found. Subsequently, the CT errors can be determined by using (4.20) and (4.21).

4.5. Application for calculating CT errors

The devised CT model together with the errors calculation algorithm allows an easy prediction of the amplitude and the phase errors at a particular peak flux density. Repeating the calculation for different values of flux density, burden or CT specification would be a tedious work. Therefore, a Labview programme (CT_model.vi) was created to read the data from the measurement file, perform necessary computations based on the desired CT specification and to save the results. The algorithm of the CT model VI is shown in Figure 4.4.

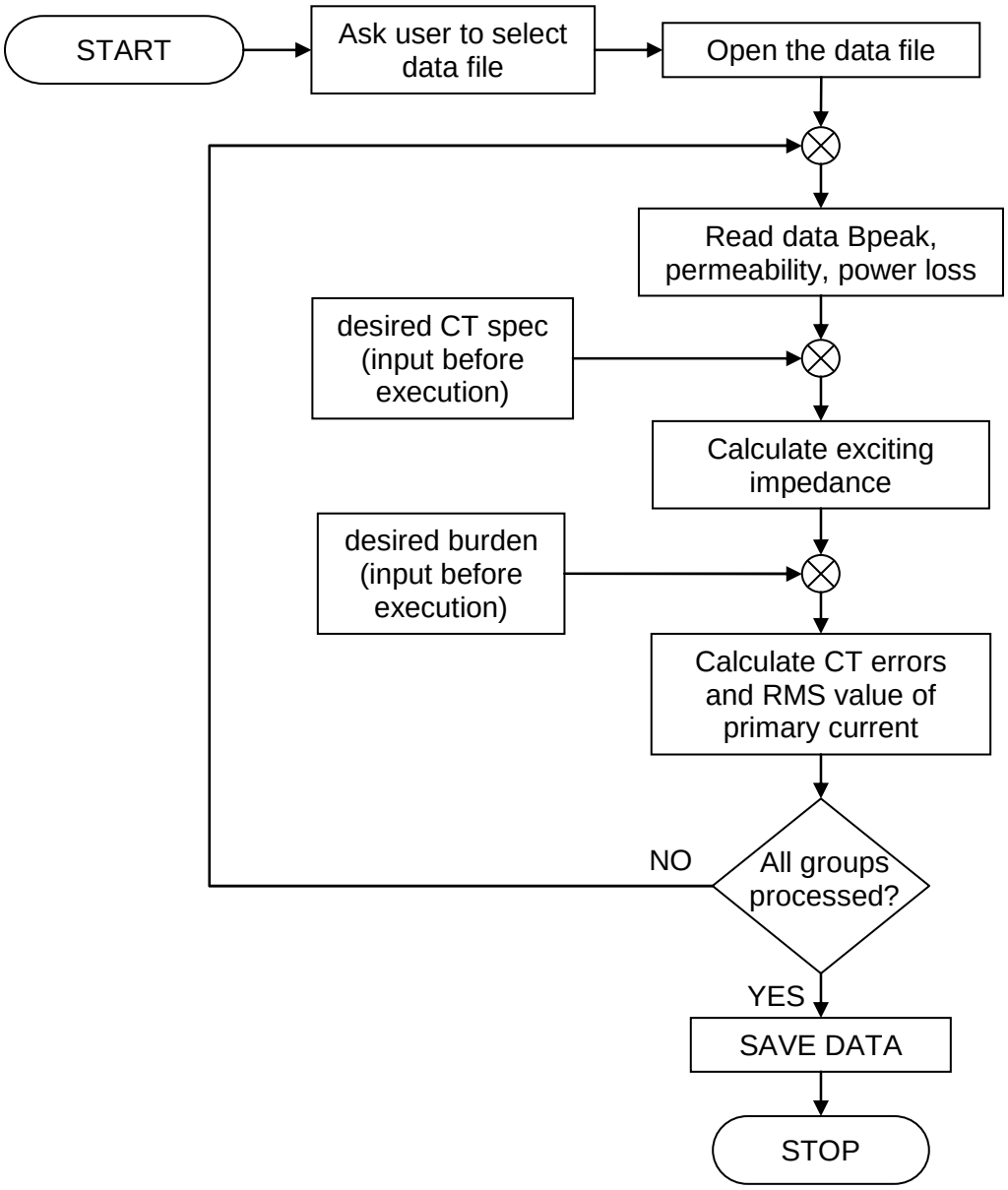

Figure 4.4 Flowchart of the CT errors prediction application

4.6. Simulation of the CT model

In order to test the developed CT model together with the Labview application for CT errors prediction, simulations were performed to establish if the modelled CT errors change with varying parameters as expected. The results were verified against theory and the CT errors behaviour as a function of the parameters explained. The design specification of the hypothetical CT is of

common industrial CTs and was identified by the collaborator (Howard Butler Ltd). The values of CT core magnetic properties were chosen without any particular importance. The aim was to see how changes in an individual parameter affect both CT errors. The burden value, number of turns, magnetic path, and the cross–sectional area is specification of tested CTs. The permeability and power loss were assumed to be the minimum expected, in order to analyse the worst case and at the same time achieve significant changes in error numbers. The errors were calculated in a wider range of flux densities than occurring normally to make sure nothing is overlooked. As with the developed CT model, a CT with a negligible leakage flux was considered. Below is the list of the parameters and its assumed values (unless being a variable in a simulation):

- burden of 5 VA apparent power and unity power factor at 5 A rated secondary current
- one primary turn and 50 secondary turns
- magnetic path of 0.23 m
- cross–sectional area of 2.8 cm^2
- relative permeability of 500
- specific power loss of 1.3 10^{-5} W/kg
- B_{pk} in the range from 1uT to 1 T
- no leakage flux

It is known that a high permeability and a low loss are desirable magnetic characteristics of a core in order to achieve low CT errors. It is also important to maintain a low burden impedance [4.11]. Therefore CT errors as a function of these three parameters were analysed.

4.6.1 The effect of CT core permeability on CT errors

The effect of changes in permeability on the CT errors was investigated first. As mentioned earlier, generally high permeability materials are chosen for CT cores in order to obtain low errors [4.11]. The simulation showed the expected result and in Figure 4.5 the amplitude error reduction can be seen with rising

permeability. The result also demonstrates the importance of the high values of permeability being retained above a certain level (in this case approximately 800) over the whole working range of a CT to ensure accurate transformation of a current.

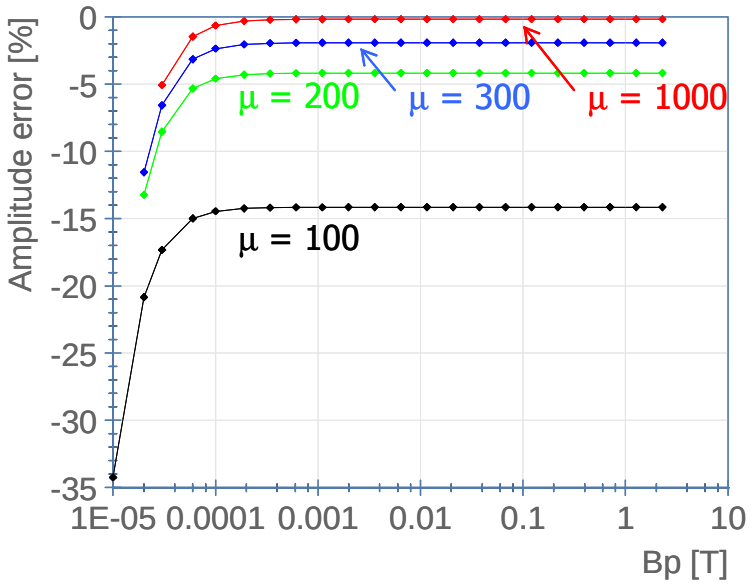

Figure 4.5 Demonstration of the influence of permeability variation on the CT amplitude error through simulation of developed CT model

It is shown clearly in Figure 4.6 that the amplitude error changes logarithmically with permeability, and thus is sensitive especially to lower values of the permeability. In this particular case, a relative permeability drop from 200 to 100 triples the error (green and black curve in Figure 4.5). In contrast, the same 50% drop from 2000 would not have any significant impact on the error (negligible error above the red curve). This increased sensitivity of the CT amplitude error to permeability below the value of 500 explains the advantage of high permeability materials for cores construction. Although there are techniques to correct the error for a constant value (e.g. a turns ratio correction), there are few magnetic materials characterised by stable permeability over the required range of flux densities, e.g. amorphous Co-rich and Fe-based alloys [4.12]; Isoperm (50% Fe-50% Ni) and Perminvar (25% Co, 45% Ni, and 30% Fe) [4.13], nanocrystalline alloys ($Fe_{73.5}Cu_1Nb_3Si_{15.5}B_7$, permeability characteristics shown in Figure 4.7) [4.14].

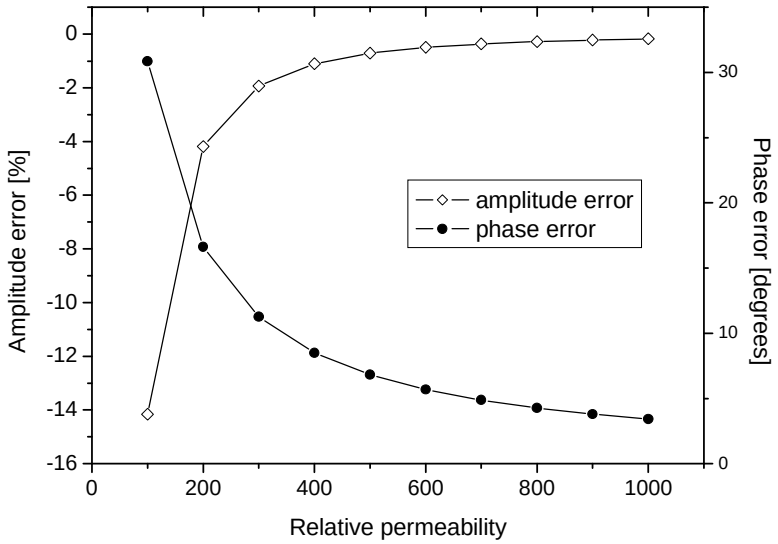

Figure 4.6 CT errors vs permeability in the simulated case

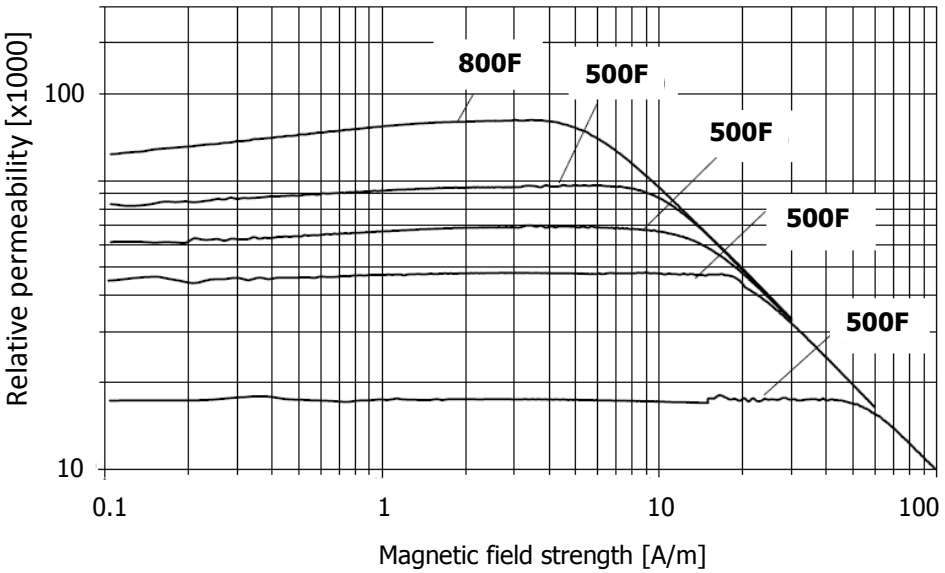

Figure 4.7 Permeability characteristics of nanocrystalline materials (VITROPERM 800 F, VITROPERM 500 F). Adapted from VACUUMSCHMELZE GmbH & Co. KG

Very much the same effect of changes in the permeability on the CT amplitude error was observed on the CT phase error, presented in Figure 4.8. The higher magnetic permeability of the CT core results in the lower phase error. The increase in the error is also not linear with the decreasing permeability as shown in Figure 4.6.

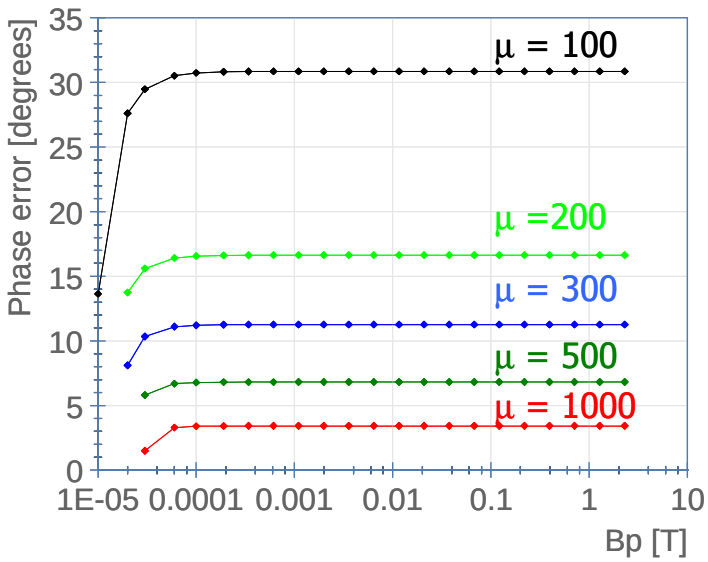

Figure 4.8 Demonstration of the influence of permeability variation on the CT phase error through simulation of developed CT model

The CT errors in both presented graphs exhibit high sensitivity to the magnetic parameters in the lower end of a flux density range. In practice the amplitude error rises abruptly due to the decrease in the permeability. In the simulation however the value of permeability is kept constant for each curve. It is therefore a different reason for the sudden change of amplitude error in the low flux density region. To explain the observed effect it is necessary to analyse the developed CT model, more specifically the formula for the exciting impedance (4.8) and (4.9). It has been discussed previously that the CT errors are related directly to the magnitude and angle of that impedance. In this case none of the parameters (i.e. CT specification, magnetic properties) is being changed, but the low values of flux density in (4.8) cause a decrease in the impedance angle which results in the increase of the amplitude error. It is easier to envisage this with the help of a phasor diagram (Figure 4.2), in which the exciting current $\mathbf{I}_E$ would rotate anticlockwise (Figure 4.9) that is increasing the difference in length between the primary and secondary current. At the same time this results in a sudden decrease of the phase error at low flux densities, whereas in practice both of the CT errors increase.

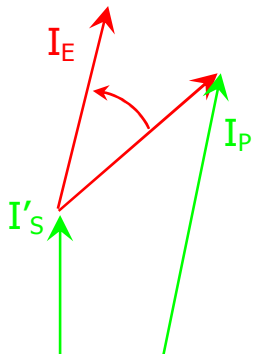

Figure 4.9 Rotation of the exciting current vector due to decreasing magnetic induction in the CT model.

Summarising, the above simulations lead to the expected results in the case of both CT errors. A high and steady permeability, over the flux density range in which CT is design to operate, ensures accurate transformation of the CT primary current.

4.6.2 The effect of CT core magnetic loss on CT errors

The second parameter to which the response of both the CT errors was investigated, was the power loss of a CT core. Figure 4.10 and Figure 4.11 illustrate the result of the simulation. Both CT errors appear to be unaffected by changes in the power loss above 40mT. Explanation for this lays in the exciting impedance equation, parts (4.8) and (4.9), where it can be seen that the power loss influences only the angle of the impedance and hence the phase shift of the exciting current. The value of the (4.8) is proportional to the power loss but at the same time, inversely proportional to the flux density squared. Consequently, above a certain value of flux density, all the values of power loss result in 90 degrees phase shift of the exciting current and thus both CT errors remain intact.

In the lower half of the flux density range, the absolute values of the amplitude error (Figure 4.10) are greater in the case of higher power loss. This is expected behaviour for materials of low loss have preference in design of CTs. The explanation for the sharp slope of all the curves has already been discussed in previous simulations.

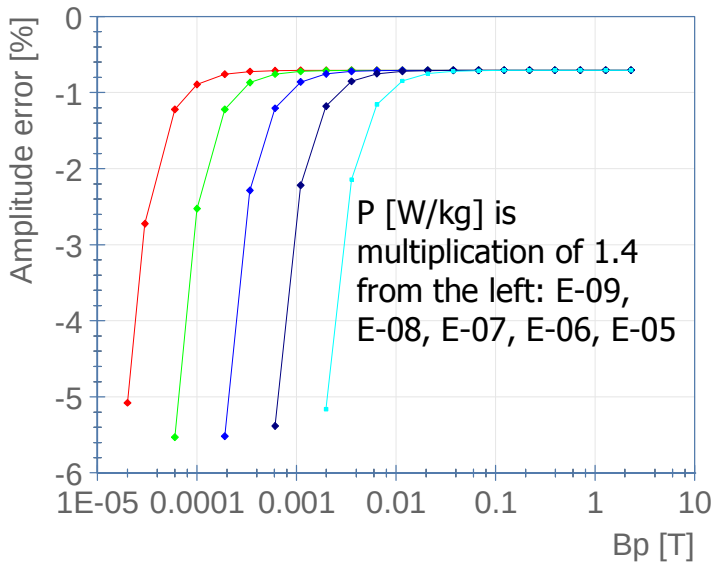

Figure 4.10 Simulation of the influence of the power loss value on the CT amplitude error

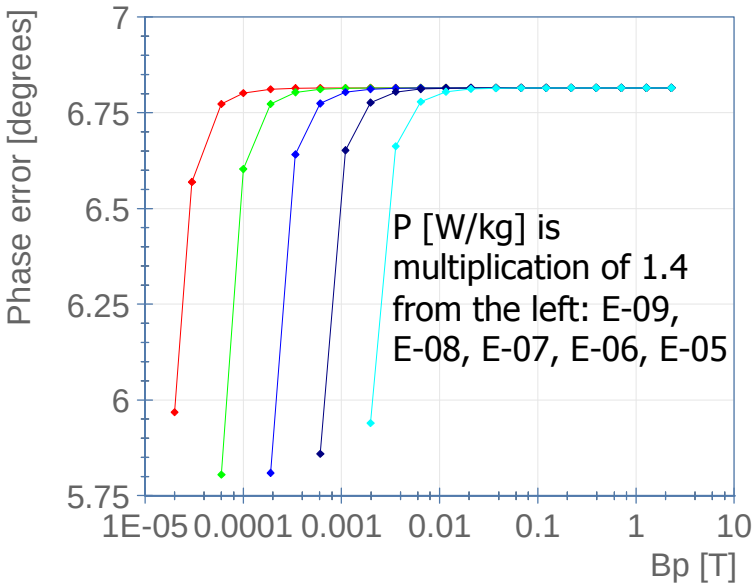

Figure 4.11 Simulation of the influence of the power loss value on the CT phase error

4.6.3 The effect of CT burden on CT errors

In the last simulation, the rated burden impedance was varied and the impact on both the CT errors verified. The results are shown in Figure 4.12 and Figure 4.13. It is clear that CT accuracy benefits from low impedance of any instrumentation connected to the secondary of a CT. This includes wiring

which is reflected as **Rs** in the CT model (Figure 4.1). In this simulation the burden was assumed to have resistive character, therefore any increase in the resistance of wires connecting a CT output to any instrumentation will have exactly the same effect.

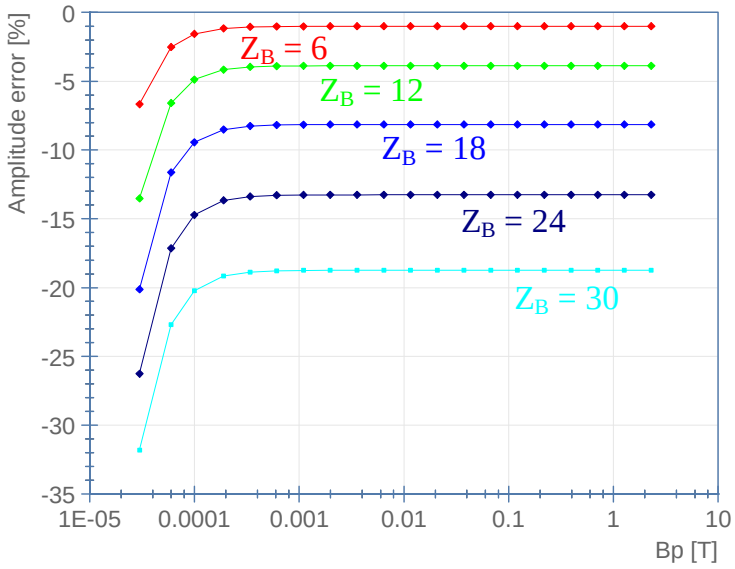

Figure 4.12 Simulation of developed CT model showing what influence burden value has on the CT amplitude error

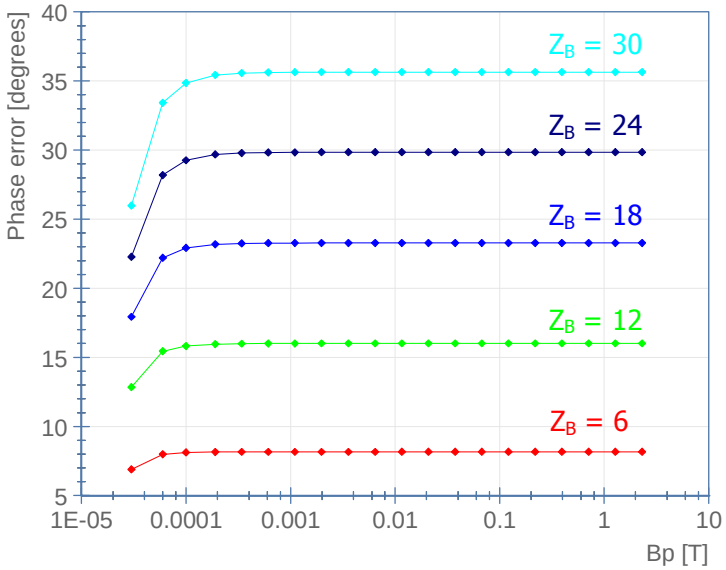

Figure 4.13 Simulation of developed CT model showing what influence burden value has on the CT phase error

Both CT errors as a function of the burden impedance are very much alike in the case of the permeability as a parameter. The latter is, in fact, affecting

directly the exciting impedance in which case it produces the same changes in CT errors. At the same time, both of the impedances can be treated as parts of a current divider in which, the higher the burden impedance, the higher the proportion of the primary current flows through the exciting impedance; hence the higher CT errors.

All of the simulations done lead to expected results thus reassuring that the developed model and software correctly represents a physical CT.

4.7. CT errors calculated from the measured data

The measured magnetic characteristics of the permeability and power loss shown in section 3.6 were used in the developed CT model to calculate the exciting impedance and, subsequently, CT errors. The burden of 1 VA was assumed (the lowest burden allowed in the relevant standard [4.6]) in the calculation of CT errors to minimise its effect on the CT errors. The number of turns in both windings have no effect on the CT errors unless considered with reference to current levels (as in section 5.2). The CT errors were plotted versus the peak flux density rather than CT primary current to allow direct comparison with the graphs of the magnetic properties. The other parameters of the CT errors calculation, i.e. the cross-sectional area of the core and magnetic path length were set to that of the investigated CTs discussed in Chapter 5.

4.7.1 Epstein size samples measured in SST

The CT errors in Figure 4.16 and Figure 4.17 were derived from the data shown in Figure 3.26 to Figure 3.29 for one of the three samples of each type of steel, CGO and HGO. It is clear that the drop in permeability of the HGO steel below approximately 10 mT results in higher (absolute value) amplitude error. It is also responsible for the 'deep dip' in the amplitude error within the region of flux densities from 0.2 to 2 mT. The lower amplitude error of the HGO steel due to higher permeability in the region of a few hundredths mT is insignificant.

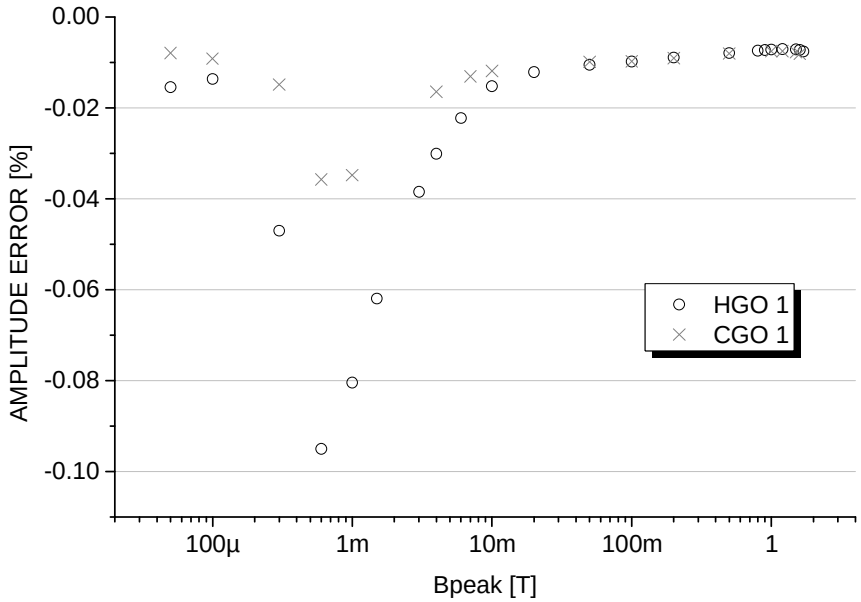

Figure 4.14 Amplitude error vs peak flux density of the CGO and HGO steel Epstein size strips

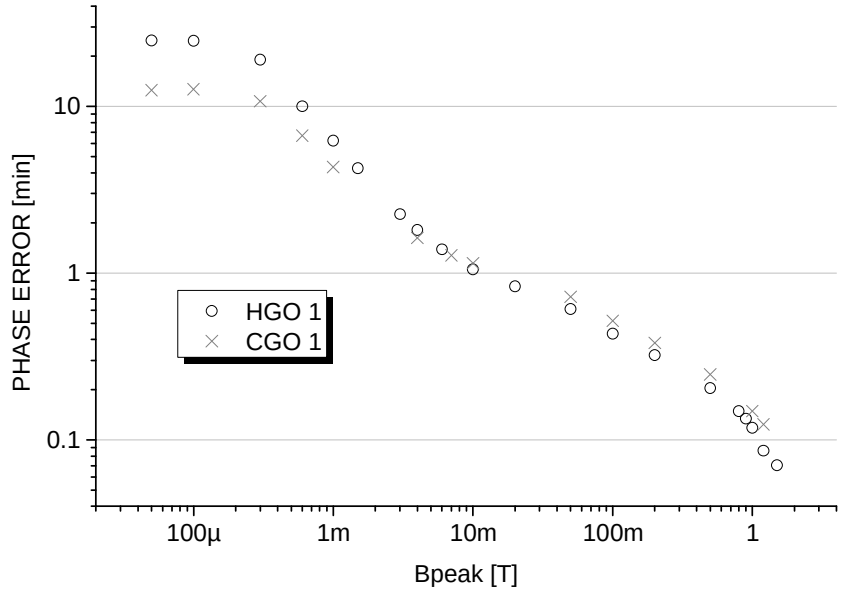

Figure 4.15 Phase error vs peak flux density of the CGO and HGO steel Epstein size strips

4.7.2 CT core samples

The magnetic characteristics of the permeability and power loss, shown in Figure 3.30 and Figure 3.31, were used in the developed CT model to calculate

the exciting impedance and, subsequently, CT errors. The results were plotted versus the peak flux density (Figure 4.16 and Figure 4.17) rather than CT primary current to allow direct comparison with the plots of the magnetic properties. The number of turns in both windings have no effect on the CT errors unless considered with reference to current levels. The other parameters of the CT errors calculation, i.e. the cross-sectional area of the core and magnetic path length were set to that of the investigated CTs. The CT errors in Figure 4.16 and Figure 4.17 are limited to the maximum peak flux density at which the parameter 'φ' of the exciting impedance (4.8) was soluble.

The investigated CT cores were of 250/5 nominal ratio CTs, of undisclosed grade steel. It can be found from the developed CT errors calculation software (CT_model.vi) that, during the operation under the burden of 1 VA, the flux density is in the range from 1.5 to 350 mT at 12.5 and 300 A of primary current, respectively. However, it is important to note that, the flux density range under the nominal burden, 10 VA and 0.8 power factor, is approximately between 16 and 400 mT. The operational flux density range is the accuracy class and burden specification dependent.

At flux densities beyond the operational value, a sharp drop in permeability (Figure 3.30) results in a lower exciting impedance (4.6), hence higher amplitude error (absolute value). This is not shown in the graphs due to the limitation of the CT model to sinusoidal waveforms. The falling value of permeability with the flux density results in increasing (absolute value) amplitude error. At the same time the phase error is rising due to a gradual change of the exciting impedance from a resistive to reactive load. When the angle of the exciting impedance vector crosses the 45^{o} threshold (around 300μT), its effect on the amplitude error is of such a significance that causes the amplitude error decrease rapidly. Both CT errors level out at about 100 μT as the permeability reduces to its constant, initial value, and exciting impedance becomes almost of fully reactive character.

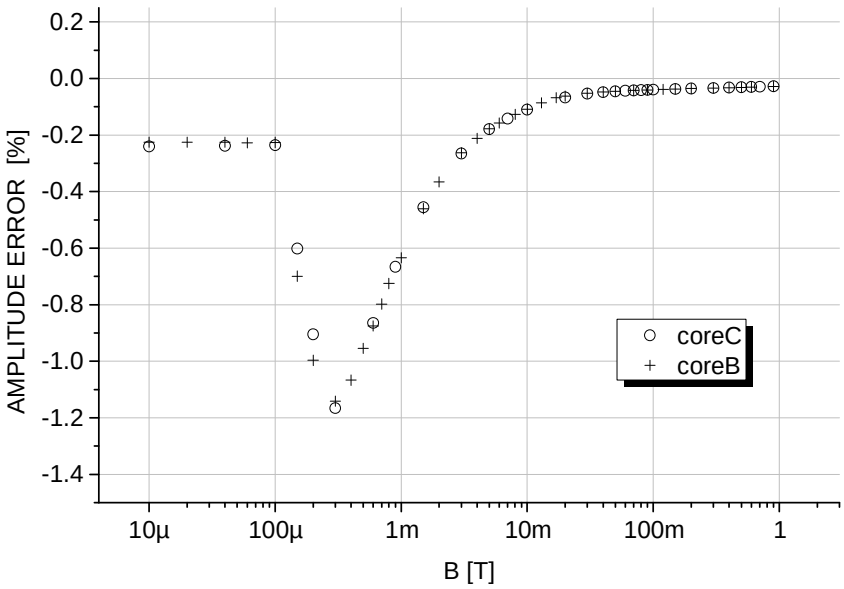

Figure 4.16 Amplitude error vs peak flux density of the CT 250/5 cores 'B' and 'C'

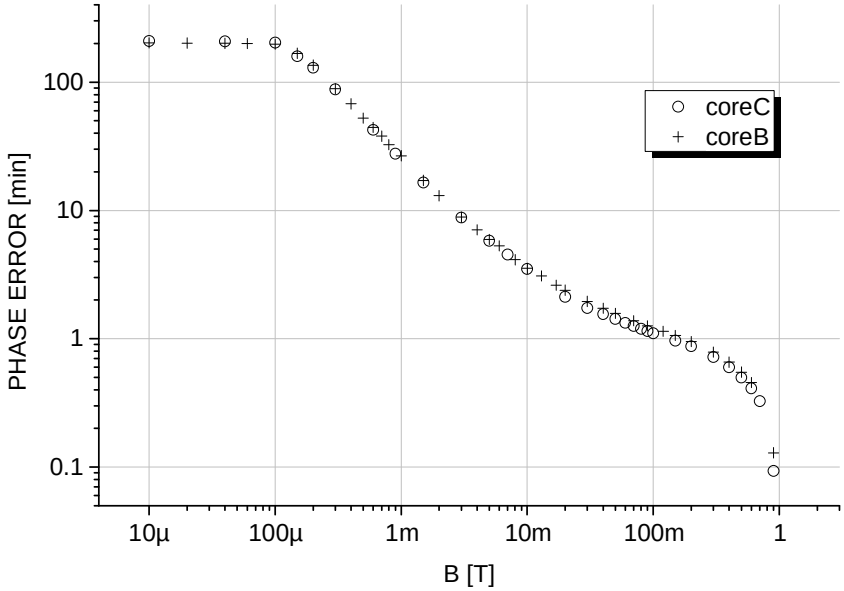

Figure 4.17 Phase error vs peak flux density of the CT 250/5 cores 'B' and 'C'

4.8. References

[4.1] N. Locci, C. Muscas, Hysteresis and Eddy Currents Compensation in Current Transformers, IEEE Transactions on Power Delivery, Vol. 16, No. 2, pp. 154–159, 2001

[4.2] U. D. Annakkage, P. G. McLaren, E. Dirks, R. P. Jayasinghe, A. D. Parker, A Current Transformer Model Based on the Jiles–Atherton Theory of Ferromagnetic Hysteresis, IEEE Transactions on Power Delivery, Vol. 15, No. 1, pp. 57–61, 2000

[4.3] A. Rezaei–Zare, R. Iravani, M. Sanaye–Pasand, H. Mohseni, S. Farhangi, An Accurate Current Transformer Model Based on Preisach Theory for the Analysis of Electromagnetic Transients, IEEE Transactions on Power Delivery, Vol. 23, No. 1, pp. 233–242, 2008

[4.4] K. Draxler, R. Styblikova, Influence of Instrument Transformers on Quality of Electrical Power and Energy Measurement, IEEE International Symposium on Industrial Electronics, pp. 1317–1321, 2007

[4.5] MCT1605, Multi–tap Automatic Current Transformer Saturation, Ratio and Polarity Test Set, User Manual, Megger Instruments Ltd, 2001

[4.6] Instrument Transformers – Part1: Current Transformers, International Standard, IEC 60044–1:1996

[4.7] A. Wright, Current Transformers, Their Transient and Steady State Performance, Chapman and Hall, 1968

[4.8] Requirements for Instrument Transformers, IEEE Standard, C57.13–2008

[4.9] E. C. Cherry, The Duality Between Interlinked Electric and Magnetic Circuits and the Formation of Transformer Equivalent Circuits, Proceedings of the Physical Society, Sec. B, Vol. 62, No. 2, pp. 101–111, 1949

[4.10] B. D. Jenkins, Introduction to Instrument Transformers, George Newnes, 1967

[4.11] Magnetic Circuits and Transformers, The MIT Press, 1965

[4.12] R. Martis, R. Hasegawa, Fe-based amorphous metal alloy having a linear BH loop, United States Patent, 2004

[4.13] S. Chikazumi, Physics of Ferromagnetism, Oxford University Press, 1997

[4.14] VACuumschmelze, Cores and Components, Soft magnetic materials: Overview and properties, Databook 2000

Chapter 5

Validation of the CT model

The developed CT model, described and pretested in section 4.6, has been used with real data on magnetic properties of cores to predict CT errors, which subsequently were compared against measured CT errors. The evaluation is based on two CTs of the same 250:5 rating but different actual transformation ratio at three different values of burden, i.e. six sets set of data were analysed. These were provided by a CTs manufacturer (Howard and Butler Ltd). The investigation is limited to this particular transformation ratio CTs due to equipment limitations. The predicted CT errors were found to be in a good agreement with measured values, taking into account the uncertainty of the CT errors test and the magnetic characterisation measurement.

Some modifications to the CT model were made in order to establish if any of the model assumptions could be responsible for the existing discrepancies between the predicted and measured CT errors, specifically in the low current region. However, simulations performed with a customized application did not show any improvement. It was therefore concluded that the higher discrepancies between predicted and measured CT errors in low currents, cannot be attributed to the CT model simplifications discussed.

5.1. Measurements required for the evaluation

Two sets of data were required for the evaluation of the CT model:

- data on magnetic properties of a core material
- the actual errors of a CT to compare against

The magnetic testing was performed by means of a purpose built system as described in Chapter 3. The CT errors measurement setup consisted of the following components (Figure 5.1):

- ITs test set TETTEX Type 2767
- programmable electronic burden TETTEX Type 3691
- current source T&R PSU–1
- calibrated CT 250:5 of nominal burden 5 VA/0.8

Figure 5.1 CT errors measurement setup

The TETTEX test set requires a standard transformer against which it compares the secondary current of the CT under test. The manufacturer offers a high precision standard current transformer (current comparator, model 4764) of multiple transformation ratios, which allows testing of CTs in the current range of 5 A to 5 kA. Not being in the inventory of our labs, this equipment was substituted with a CT of 0.2 S [5.1] accuracy class and 250:5 nominal transformation ratio. It was calibrated and the certificate data used to correct all the CT errors measurement results. In order to test the different ratio CTs, respective standard transformers would have to be acquired, thus the investigation was limited to 250:5.

In this study, current transformers of 250:5 rated transformation ratio, 80 mm outside diameter, and 43 mm inner diameter, 35 mm height, designed to work

with a burden of 10VA and 0.8 power factor, were used. Power frequency primary current was varied in the range of 2.5 to 300 amperes as per [5.1] at different values of the burden impedance and the CT errors were determined. Each test under specific condition was repeated three times to ensure correct readings. CTs were tested starting at the lowest value of the burden and the highest being the last. Following the instructions of the ITs testing standard, CTs were demagnetised prior to testing to ascertain the cores did not have any residual flux. Significantly higher CT error readings were noted when the current source tripped during a test. In such cases the procedure was stopped, both CTs (being tested and standard) demagnetised, and subsequently the measurement was continued.

After CT errors testing, the BH characteristics of the CTs under investigation were measured over a wide range of the flux densities (1 mT – 1 T) with the low flux density system. The power loss and the permeability were determined from the hysteresis loops. These were then used in the CT errors calculation algorithm.

CT cores were used as samples for magnetic testing, to ensure the agreement of the magnetic properties between the samples and the CTs. Data from other types of samples could be utilised in the presented model, as long as the differences in magnetic behaviour of a CT core are either negligible or accounted for.

5.2. The predicted CT errors vs measured

Predicted amplitude and phase errors were compared with the experimental data for two CTs of the same rated ratio (but different actual ratio) at three different values of burden (2.5, 10, and 20 VA). The results are presented in Figure 5.2 and Figure 5.3. The CT 'B', under all burden condition, meets the requirements of class 3. However, the class rating could be improved to class 0.2 by modifying the turns correction by a fraction of a turn. The results of the CT 'C' tests indicate the accuracy class of 0.5 but with the correction of a

fraction of a turn, the accuracy rating could be improved to 0.2. The actual turns correction can be determined with the developed CT model and errors calculation software by running a series of CT errors calculations for a series of turns corrections, and at the required values of burden following the requirements in the relevant standard [5.1].

Two extreme cases are discussed in details; Figure 5.3 a and b show the amplitude and phase errors respectively of 250:5 "C" CT investigated under the burden of 2.5 VA and unity power factor. The predicted and measured curves follow the same trends, though it can be seen that the predicted errors are overestimated at low currents. Nonetheless, it has to born in mind that, as the CT errors test has a limited accuracy (as discussed in section 5.4), so do the measurement of the magnetic properties from which the CT errors are calculated. During both measurements, scatter of the readings in a range as wide as 21% was observed with all the experimental precautions taken.

The second CT used for the evaluation of the model (B) had the same type of core but its actual ratio was different from the rating value. The CT had 49 secondary turns and therefore a positive amplitude error at the rated current and above, as can be seen in Figure 5.2e. The same tendency of the predicted errors increasing at a higher rate than the measured values is observed in the case of both errors (Figure 5.2 e and f).

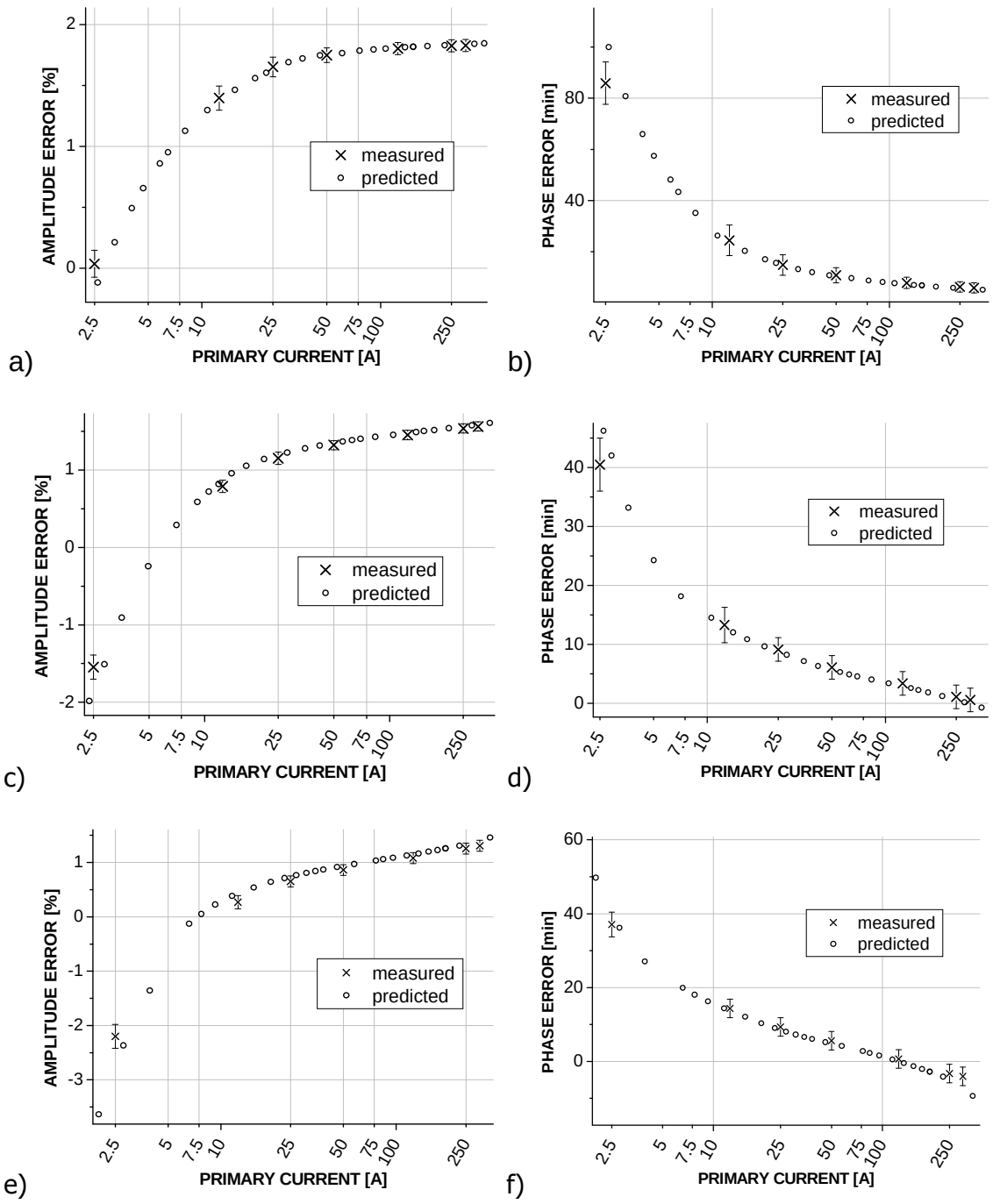

Figure 5.2 The Predicted and measured results for the CT "B" 250:5 under 2.5 VA burden and unity power factor (a) amplitude error and (b) phase error; under 10 VA burden and 0.8 power factor (c) amplitude error and (d) phase error; under 20 VA burden and 0.8 power factor (e) amplitude error and (f) phase error

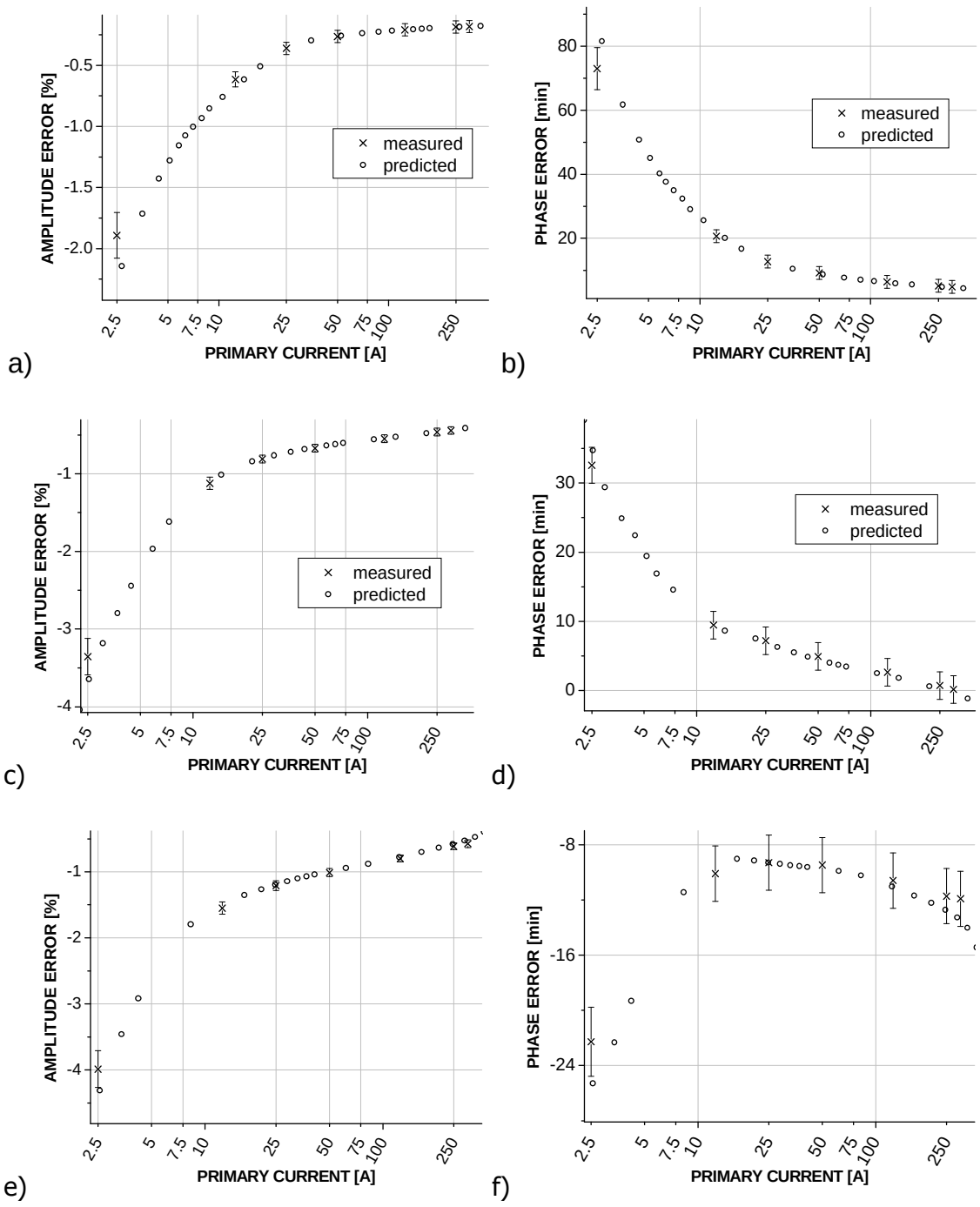

Figure 5.3 The predicted and measured results for the CT "C" 250:5 under 2.5 VA burden and unity power factor (a) amplitude error and (b) phase error; under 10 VA burden and 0.8 power factor (c) amplitude error and (d) phase error; under 20 VA burden and 0.5 power factor (e) amplitude error and (f) phase error

For the "B" CT, results under the highest burden impedance are shown for comparison. In this case, the prediction remains within the error bars of the CT test over the whole range of currents, and that can be seen for both, the amplitude and phase error. It should be noted that the errors close to the rated current of the CT are slightly overestimated compare to those of the CT "C".

This might be caused by a mismatch of the burden impedance in the test setup and the modelling. It can be caused by operating the CT above its rated specification, in which case the resistance of the secondary winding and leads connecting it to the equipment could be affected by excessive temperature. It should also be noted that, at the highest value of burden, the CT errors at the maximum current were showing instability. It could be a sign of the equipment straining to maintain a set value of the burden.

Overall, the predicted CT errors were found to be in good agreement with measured values, taking into account the uncertainty of CT errors test and the magnetic characterisation measurement. The estimate of the latter is more complex for the model will show different sensitivity to inaccuracy in the measurement of the magnetic properties depending on a particular CT and the desired specification. Nonetheless, assuming the uncertainty of the predicted values to be approximately equal to the BH characterisation, in all the cases investigated the model results met the tested CT errors within the uncertainties of both.

5.3. Modifications of the CT model

The precise reason for the higher discrepancies between the predicted and measured CT errors in low currents is not known. Attempts were made to associate it with any of the two assumptions of the CT model, namely:

- the leakage flux in the secondary winding of the CT is negligible
- all signals in the CT equivalent circuit are sinusoidal

To ascertain the influence of the first simplification, an additional parameter (leakage reactance) was added into the secondary side of the CT equivalent circuit diagram. However a simulation of the modified CT model did not show any significant improvement in the low current region. In Figure 5.4, the amplitude error of the "C" CT is shown (as Figure 5.3a) with the CT errors predicted from a model that includes the leakage reactance. Clearly the

introduction of the reactance in the CT equivalent circuit diagram impairs the amplitude error prediction over the whole range of the CT.

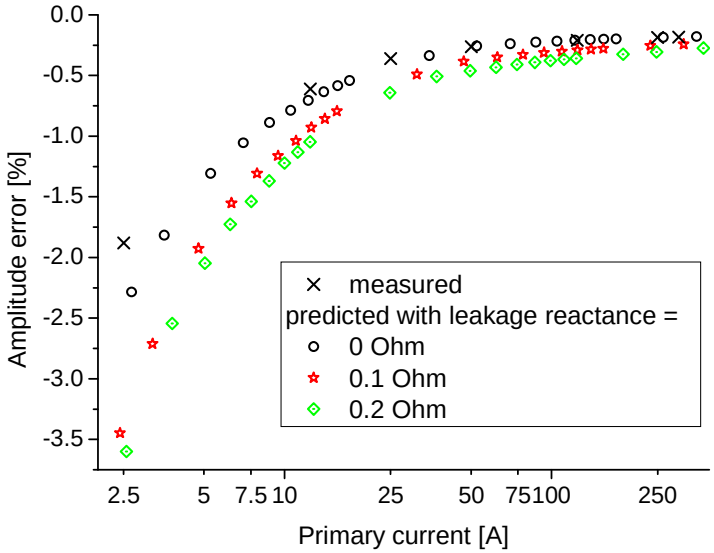

Figure 5.4 Predicted and measured amplitude error of the CT "C" 250:5 under 2.5 VA burden

On the other hand, the phase error results (Figure 5.5) show a decrease in the predicted phase error. Since the leakage flux is expected to vary with the magnetic flux density in a core, it should be possible to match the value of the introduced reactance in order to improve the prediction of the phase error. However, this would cause a deterioration of the amplitude error prediction. Therefore, it was concluded that the existence of a leakage flux in the tested CT is unlikely and hence the assumption of a negligible leakage flux in the CT secondary was correct.

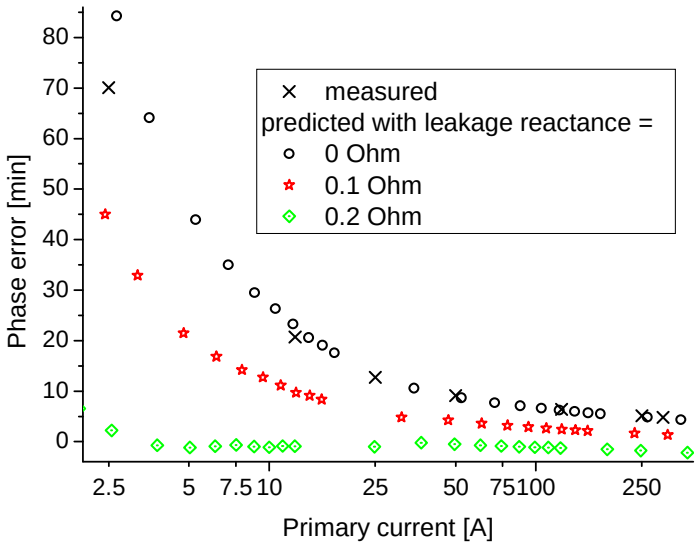

Figure 5.5 Predicted and measured phase error of the CT "C" 250:5 under 2.5 VA burden

Similar conclusions can be drawn from analysing the phasor diagram (Figure 4.2) presented in section 4.1. One can imagine an additional vector representing the leakage reactance in line with a reactive part of a burden (Figure 5.6a). This would cause the flux in a CT core to rotate anticlockwise so that a right angle would remain between the flux and the secondary induced voltage vectors. As a result, the CT phase displacement would decrease and the amplitude error increase, as observed in the simulated case in Figure 5.4 and Figure 5.5. The resulting changes in values of the CT errors are dependent on the starting point values of the CT equivalent electrical circuit. The opposite changes, increase of the phase displacement and decrease of the amplitude error, can take place when the significant reactive components are present in the CT secondary circuit and the exciting impedance is strongly resistive, as shown in Figure 5.6b. In such a case, the difference in length of the primary and secondary current, being the amplitude error, can in fact decrease. Nonetheless, this would result in a considerable overestimate of phase displacement.

On the basis of the above simulations and analysis, it can be concluded that the leakage flux could not possibly be the cause for the observed discrepancies in predicted and measured CT errors. Furthermore, this implies that the assumption of a negligible leakage in the CT secondary is valid.

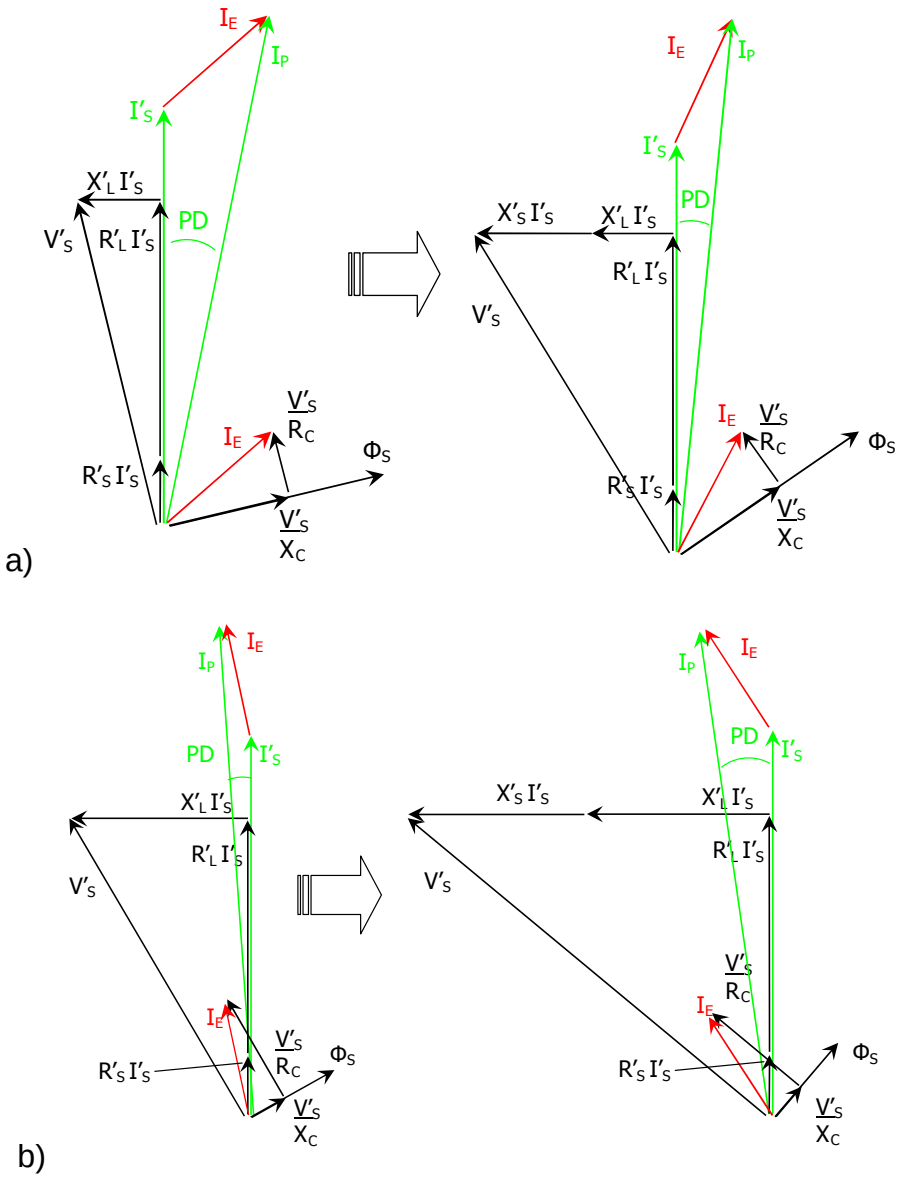

Figure 5.6 The effect of leakage reactance on the CT errors depending on the initial values of CT equivalent circuit elements: a) high power factor of the burden and low factor of the exciting impedance; b) low burden power factor and high exciting impedance power factor

In an effort to validate the negative impact of the second limitation on the CT model, a different method was used to calculate CT errors. The RMS values of the signals recorded during the magnetic testing were utilized instead of the CT core magnetic properties in a modified CT errors computation algorithm. This did not introduce any significant change in the predicted values of the CT errors, i.e. the nonlinearity of the core is negligible.

Since the above attempts to associate the earlier observed deficiency of the CT model failed, it was concluded that the higher discrepancies between predicted and measured CT errors in low currents, cannot be attributed to the CT model simplifications discussed. However, magnetic measurements at low excitation levels are known to be more difficult to perform and, as a result, suffer from higher errors, which would of course propagate through the model.

5.4. Uncertainty of the CT errors test

The uncertainties of the CT error test were estimated according to [5.2]. Contributions of the systematic ("Type B" analysis) and random errors ("Type A" analysis) are combined in the uncertainty budget as shown in Table 5.1. The uncertainty was estimated separately for each current test point. An example of the uncertainty budget for the measurement of CT amplitude and phase error at rated value of current (250 A), under the smallest load, is shown in Table 5.1 and Table 5.2 respectively.

Table 5.1 Uncertainty of the CT "C" amplitude error measurement at the CT rated value of current under the smallest load (Figure 5.3a)

Source of uncertainty	**± %**	**Probability distribution**	**Divisor**	**C_i**	**U_i ± %**	**V_i or V_{eff}**
Standard CT calibration	27.80	Normal	2.00	1	13.90	∞
TETTEX error indication	4.30	Normal	2.00	1	2.15	∞
TETTEX burden	4.24	Normal	2.00	1	2.12	∞
TETTEX excitation	1.30	Normal	2.00	0.12	0.08	∞
Current setting	0.40	Rectangular	1.73	0.12	0.03	∞
Repeatability	0.50		1.73	1	0.29	2
Sum of squares					202.44	13336795
Combined uncertainty					14.23	
Expanded uncertainty (at 95 % confidence level)					28.50	

Table 5.2 Uncertainty of the CT "C" phase error measurement at the CT rated value of current under the smallest load (Figure 5.3b)

Source of uncertainty	**± %**	**Probability distribution**	**Divisor**	**C_i**	**U_i ± %**	**V_i or V_{eff}**
Standard CT calibration	26.00	Normal	2.00	1	13.00	∞
TETTEX error indication	3.55	Normal	2.00	1	1.77	∞
TETTEX burden	4.24	Normal	2.00	1	2.12	∞
TETTEX excitation	1.30	Normal	2.00	0.34	0.22	∞
Current setting	0.40	Rectangular	1.73	0.34	0.08	∞
Repeatability	1.11		1.73	1	0.64	2
Sum of squares					177.13	424082
Combined uncertainty					13.31	
Expanded uncertainty (at 95 % confidence level)					27.00	

The elementary uncertainties in the budget are stated as percentage uncertainties of the test results, with applied correction according to the calibration certificate. The method of correction is derived in section 0. The source of the elementary uncertainties and method of the calculation are presented below:

- Standard CT calibration is the percentage value of the calibration uncertainty vs measured current corrected according to this calibration. It is the highest contribution to the overall uncertainty when the measurand is small (close to accuracy of an instrument).
- TETTEX error indication is the CT error measurement uncertainty value of the automatic test set equipment, calculated according to [5.3].
- TETTEX burden is the uncertainty of the electronic burden equipment in maintaining a desired load of the CT under test [5.4].
- TETTEX excitation is the uncertainty of the primary current indication by the test set [5.3].

- Current setting has its source in the limited precision of the primary current injection system (T&R PCU1–SP). It describes the ability of a user to set a required value of primary current.
- Repeatability is the result of statistical analysis on a set of measurement data points. It estimates the effect of random errors on the accuracy of the measurement. It was calculated as a standard deviation and its divisor is equal to the square root of number of samples.

5.4.1 T standard calibration certificate correction

The correction stated in a calibration certificate is commonly added to the measured value. Below it is examined if the correction can be applied in the same way to CT amplitude error.

Let us define:

- $\mathbf{I_A}$, $\mathbf{I_B}$ as RMS secondary current value of calibrated CT and under test, correspondingly
- $\mathbf{I_N}$ as RMS current value (primary) at which calibration was done
- $\mathbf{K_A}$, $\mathbf{K_B}$ as rated transformation ratio of calibrated CT and under test correspondingly
- **E [%]** as amplitude error of calibrated CT
- **F [%]** as amplitude error of CT under test compare to calibrated CT
- **X [%]** as amplitude error of CT under test

From the definition of the amplitude error [5.1] it can be written that:

$$\frac{I_A K_A - I_N}{I_N} \cdot 100 = E\,[\%] \quad \Rightarrow \quad I_N = \frac{I_A K_A 100}{E + 100} \tag{5.1}$$

$$\frac{I_B K_B - I_A K_A}{I_A K_A} \cdot 100 = F\,[\%] \quad \Rightarrow \quad I_B = \frac{K_A I_A (F + 100)}{100 K_B} \tag{5.2}$$

$$\frac{I_B K_B - I_N}{I_N} \cdot 100 = X\,[\%] \tag{5.3}$$

The amplitude error "X" of interest can be found by substitution of equations (5.1) and (5.2) in (5.3) which leads to:

$$X\ [\%] = \frac{EF}{100} + E + F \tag{5.4}$$

The above can in most cases be simplified to just simply a sum of both errors (calibrated CT and tested), although it is important to be aware of the implications. If the measured CT amplitude error is equal to the calibration correction and at the same time both happen to be high in magnitude (>11 %), the error introduced by the mentioned simplification will be more than 10 %. It shows that a significant error might be introduced by simply adding up the calibration correction to a measured value of the amplitude error in certain cases.

5.5. References

[5.1] Instrument Transformers – Part1: Current Transformers, International Standard, IEC 60044–1:1996

[5.2] The Expression of Uncertainty and Confidence in Measurement, UKAS publication M3003, 2007

[5.3] Automatic Instrument Transformer Test Set TYPE 2767, Instruction Manual, TETTEX Instruments

[5.4] Programmable Electronic Current Burden TYPE 3691, Instruction manual, TETTEX Instruments

Chapter 6

Conclusions and future work

6.1. The system for measuring the low flux density magnetic properties

6.1.1 Achievements

The developed low flux density measurement system is capable of measuring magnetic properties of materials at flux densities as low as few μT. It was verified that the magnetic properties of the GO electrical steels can be measured from 10 μT and 100 μT of the toroidal and Epstein size samples, respectively with the estimated uncertainty of:

- For the permeability – ±8% up to the peak flux density of 50 mT and ±3% above that value;
- For the total power loss – ±13% below 50 mT and ±5% above.

It has been shown that the developed measurement setup can be used for testing variety of ferromagnetic materials, other than GO electrical steels. This can allow investigation of the magnetic processes at low flux densities.

An innovative digital compensation has been incorporated in the control application which contributed to the lower noise levels in the measured search coil signal. It simplifies the measurement setup of the Epstein frame and SST methods. Through eliminating the need for extra compensation coil it reduces the electromagnetic interferences that could affect the results.

The cycle averaging was partially substituted with a moving average technique in order to significantly speed up the testing procedure.

The control feedback has been automatized to decrease the duration of the measurement and most importantly necessary interaction from the operator.

A work around was found and validated for triggering a digital acquisition card from a device constructed of delta-sigma ADCs. This will allow the use of very precise equipment in applications were previously it had not been possible or cost-prohibitive.

The crucial part of the system is both, the high and low frequency, shielding that reduces the necessary averaging and allows greater control over the magnetisation inside the sample.

A phenomenon was revealed involving the CGO and HGO steels in which their permeability and power loss being higher or lower at high flux densities, reverses at flux densities around few tens of mT.

6.1.2 Future work

Recommendations for future work include further noise shielding to extend the measuring range of the system below μTs and potentially improve the repeatability which was found is the major factor limiting the accuracy.

The exposed phenomenon of the reduction in permeability and increase in the loss of the HGO steel requires further testing to confirm this is a general effect and not limited to faulty batch of material or other factors. The effect could possibly be explained by the grain size and the expected longer domain walls in the HGO material compare to CGO. The longer domain walls could pose a higher inertia at feeble fields and result in lower permeability than that of the CGO. At the same time the eddy current loss which is most likely to be responsible for the sharp rise in the power loss of the HGO material above 100 μT could also be related to the bigger length of the domain walls or the 'bowing' part of domain walls.

6.2. Current transformer modelling

6.2.1 Achievements

The relationship between the CT errors and the magnetic properties of its core has been investigated and a model proposed allowing calculation of the errors from the basic magnetic properties of a core. The model has been validated and found to return the CT errors accurately.

It was shown that the assumption of the negligible leakage flux was correct. The performed simulations of the effect the magnetic properties have on the CT errors demonstrated the usefulness of the model and the developed software for calculation of CT errors.

The magnetic data measured with the developed low-flux density system was used to calculate CT errors in wide range of flux densities from 20 μT to 1 T. It showed that the developed tool allows to verify different designs of a CT of different specifications with a click of button.

The calculated with the model CT errors from the measured properties of HGO and CGO steel strips indicate that due to the observed phenomenon of the HGO material performance weaker than that of CGO at low flux densities, a core made of CGO steel could potentially offer better accuracy. It has been shown that the CT errors are more likely to be outside the accuracy class at low flux densities.

6.2.2 Future work

Future work could extend the developed CT model for measuring non–sinusoidal currents. It is suggested to employ a technique of superposition and, in essence, consider a series of models for each necessary harmonic separately. This way a CT response to distorted waveforms could be predicted with use of the developed CT model.

The performance of the developed CT model in the presence of DC bias could be investigated by using magnetic data on the core in this conditions.